

Title: Mitochondrial Ca^{2+} influences photoresponse recovery, metabolism, and mitochondrial localization in cone photoreceptors

Authors: Rachel A. Hutto¹, Celia M. Bisbach¹, Fatima Abbas², Daniel Brock¹, Whitney M. Cleghorn¹, Edward D. Parker¹, Benjamin Bauer¹, William Ge¹, Frans Vinberg², James B. Hurley¹, Susan E. Brockerhoff¹

Affiliations:

1. Biochemistry Department, University of Washington, Seattle WA 98109

2. John A. Moran Eye Center, University of Utah, Salt Lake City UT 84132

Abstract

Mitochondrial Ca^{2+} regulates key cellular processes including cytosolic Ca^{2+} signals, energy production, and susceptibility to apoptosis. Photoreceptors are specialized neurons that have extraordinarily high energy demands and rely on cytosolic Ca^{2+} signals for light adaptation and neurotransmission. Here we show that unlike other neurons zebrafish cone photoreceptors express low levels of the mitochondrial Ca^{2+} uniporter (MCU), the channel that allows mitochondrial Ca^{2+} entry. To determine why MCU expression is kept low, we overexpressed MCU specifically in cones. This increases mitochondrial $[\text{Ca}^{2+}]$, causes faster cytosolic Ca^{2+} clearance, and accelerates photoresponse recovery. Moreover, flux through the citric acid cycle increases despite dramatic changes in mitochondrial ultrastructure and localization. Remarkably, cones survive this ongoing stress until late adulthood. Our findings demonstrate the importance of tuning mitochondrial Ca^{2+} influx to modulate physiological and metabolic processes and reveal a novel directed movement of abnormal mitochondria in photoreceptors.

Introduction

Photoreceptors are highly specialized sensory neurons responsible for vision. In addition to having unique and vulnerable structural features, photoreceptors reside in the retina, a hostile cellular environment. They can be exposed to damaging light radiation, are located near blood vessels with high levels of oxygen, and use more ATP

than most cells in the body. Despite these chronic stressors, most people retain vision throughout their lives, highlighting the extraordinary ability of photoreceptors to regulate cellular homeostasis and maintain viability.

Photoreceptor function and survival depends on Ca^{2+} homeostasis. Photoreceptors rely on Ca^{2+} as a second messenger to recover from light signals and adapt to constant illumination (Nakatani and Yau, 1988). In darkness they continuously release synaptic vesicles, which requires precise regulation of synaptic Ca^{2+} by L-type voltage-gated channels (Barnes and Kelly, 2002). Both chronic elevations and chronic decreases in cytosolic Ca^{2+} have been implicated in photoreceptor cell death and retinal disease (for review, see Fain, 2006; Vinberg et al., 2018). Mutations in photoreceptor phosphodiesterase, guanylyl cyclase, and guanylyl cyclase activating protein result in sustained high Ca^{2+} in the cell and cause retinal degeneration (Bowes et al., 1990; Dizhoor et al., 1998; Fox et al., 1999; Payne et al., 1998; Sokal et al., 1998; Tucker et al., 1999; Wilkie et al., 2000). Sustained light exposure or deficiencies of rhodopsin kinase and arrestin that cause sustained low intracellular Ca^{2+} also cause degeneration of photoreceptors (Chen et al., 1999a, 1999b; LaVail et al., 1987).

Cytosolic Ca^{2+} in photoreceptors is buffered and regulated by the endoplasmic reticulum (ER) and mitochondria (for review, see Križaj, 2012). In the synapse, Ca^{2+} flow through the ER to the synaptic terminal supports sustained CICR-driven synaptic transmission (Chen et al., 2015). Mitochondria are most abundant in a region of the cell body termed the “ellipsoid”, between the outer segment (where phototransduction occurs) and the rest of the cell body and synapse (Hoang et al., 2002). Ca^{2+} pools in the outer segment are distinct from the rest of the cell, and it has been suggested that ellipsoid mitochondria can protect the cell body from the high Ca^{2+} generated in the outer segment as a consequence of phototransduction (Križaj and Copenhagen, 1998; Szikra and Krizaj, 2007). It was recently shown in zebrafish photoreceptors that ellipsoid mitochondria maintain the distinct Ca^{2+} pools between the outer segment and the cell body (Giarmarco et al., 2017).

Mitochondrial Ca^{2+} uptake is also involved in energetic output (Glancy and Balaban, 2012). Ca^{2+} can regulate the activity of mitochondrial enzymes including pyruvate dehydrogenase, isocitrate dehydrogenase, and α -ketoglutarate dehydrogenase (Denton, 2009). The aspartate/glutamate exchangers on the inner mitochondrial membrane are sensitive to Ca^{2+} (Contreras et al., 2007; Satrústegui et al., 2007). Ca^{2+} also may regulate the activity of ATP synthase (for review, see Glancy and Balaban, 2012). Increased mitochondrial matrix Ca^{2+} has been linked to increases in NADH and ATP production in multiple cell types (Balaban, 2009; Hajnóczky et al., 1995; Jouaville et al., 1999). However, metabolic responses to changes in mitochondrial Ca^{2+} vary across tissues, likely reflecting the diverse metabolic demands of different tissues (Griffiths and Rutter, 2009). It is not currently known to what extent fluxes in mitochondrial Ca^{2+} influence metabolism in photoreceptors, which have extraordinarily high ATP demand (Okawa et al., 2008).

While modest increases in mitochondrial Ca^{2+} can stimulate energy production, excessive mitochondrial Ca^{2+} can trigger opening of the mitochondrial permeability transition pore (Baumgartner et al., 2009). Prolonged opening of the pore is associated with mitochondrial swelling, collapse of the proton gradient, and release of mitochondrial solutes that eventually results in cell death (Bernardi et al., 1999; Kroemer et al., 1997; Rizzuto et al., 2012; Smaili et al., 2000; Zoratti and Szabò, 1995). In isolated rat retina, increases in cellular Ca^{2+} and Pb^{2+} cause photoreceptor-selective apoptosis that depends on mitochondrial permeability transition pore activity (He et al., 2000).

Ca^{2+} import into the mitochondrial matrix in all cells occurs via the mitochondrial Ca^{2+} uniporter complex (MCU complex), comprised of a tetramer or pentamer of the pore-forming protein MCU that associates with several regulator proteins (Baradaran et al., 2018; Baughman et al., 2011; Fan et al., 2018; Nguyen et al., 2018; Oxenoid et al., 2016; De Stefani et al., 2011, 2015; Yoo et al., 2018). The small transmembrane protein EMRE is necessary for MCU function in vertebrates (Sancak et al., 2013). MICU proteins tune Ca^{2+} uptake through the uniporter complex. MICU1 imparts cooperativity to Ca^{2+} entry and is required for other MICU proteins to interact with the MCU complex (Csordás et al., 2013; Kamer et al., 2014; Mallilankaraman et al., 2012). MICU2 has a

distinct inhibitory effect on Ca^{2+} entry at high cytosolic Ca^{2+} concentrations (Patron et al., 2014; Plovanich et al., 2013). MICU3, enriched in neurons, confers hyper- Ca^{2+} uptake activity (Patron et al., 2018). The MCU pore can also include a dominant negative form of the MCU subunit, called MCUB (Raffaello et al., 2013). Finally, several other mitochondrial proteins have been purported to interact with the MCU complex and potentially modulate its function (Chaudhuri et al., 2016; Hoffman et al., 2014; Nieminen et al., 2014; Paupe et al., 2015; Tomar et al., 2016; Zeng et al., 2018). This degree of regulation of MCU, along with the variability of modulator expression across tissues, implies that the activity of this complex is attuned specifically to cellular needs.

To begin to investigate the relationship between Ca^{2+} and photoreceptor mitochondria we analyzed protein and transcript levels of MCU, MICU1, MICU2 and MICU3 in retina compared to heart and brain. We found that MICU transcript expression in retina and brain is strikingly similar. However, the retina has much lower MCU protein expression than brain or heart tissue, and MCU is particularly low in cone photoreceptors. To elucidate why MCU expression may be limited in cones, we generated zebrafish models of cone-specific MCU overexpression. We found that elevated MCU in cones increases mitochondrial Ca^{2+} content, alters cytosolic Ca^{2+} transients and the photoresponse, and increases flux through citric acid cycle enzymes. MCU overexpression also causes dramatic changes in mitochondrial morphology accompanied by a directed movement of mitochondria away from the ellipsoid region of the cell. Despite these morphological changes and disruptions to Ca^{2+} and cellular homeostasis, cones overexpressing MCU survive well into adulthood before degenerating. Our findings uncover how mitochondrial Ca^{2+} content can affect cone function and open a new area of research investigating survival strategies employed by these sensory neurons.

Results

MCU expression is specifically limited in retinal tissue

We developed a custom antibody against the purified N-terminus of zebrafish MCU and verified the specificity of this antibody using a global zebrafish MCU knock-out (MCU KO, **Figure 1A**). Using this antibody, we found that MCU protein expression (as normalized to total protein) is significantly higher in brain tissue than retina, which is even lower than heart tissue (**Figure 1A**). When normalizing MCU protein to other mitochondrial inner membrane proteins cytochrome oxidase (MTCO1) and succinate dehydrogenase (SDH), the retina more closely resembles heart tissue (**Figure 1B**). To see if this low retinal abundance of MCU was reflected in other regulators of the complex, we used RT-qPCR to determine the relative mRNA quantity of the MCU regulators MICU1, MICU2, and MICU3 (which has two isoforms in zebrafish) across the same tissues. Expression of all MICU transcripts in retina is more similar to expression in brain rather than heart (**Figure 1C**).

To quantify MCU expression specifically in zebrafish cone photoreceptors, we took advantage of a zebrafish cone degeneration model caused by a mutation in the cone phosphodiesterase (*pde6c*^{-/-}); in this model, cones selectively degenerate while rods and other retinal neurons are preserved (Stearns et al., 2007). We analyzed MCU and mitochondrial membrane protein expression in the *pde6c*^{-/-} mutants compared to their WT siblings and found that without cones there is a loss in mitochondrial membrane protein expression that is not reflected in a loss of MCU signal (**Figure 1D,E**). The loss of MTCO1 and SDH expression in the *pde6c*^{-/-} mutant is consistent with cones having more mitochondrial volume than rods (Hoang et al., 2002), but the data indicate that these cone mitochondria have relatively little MCU compared to other retinal neurons. Our antibody was not suitable for IHC of the endogenous protein.

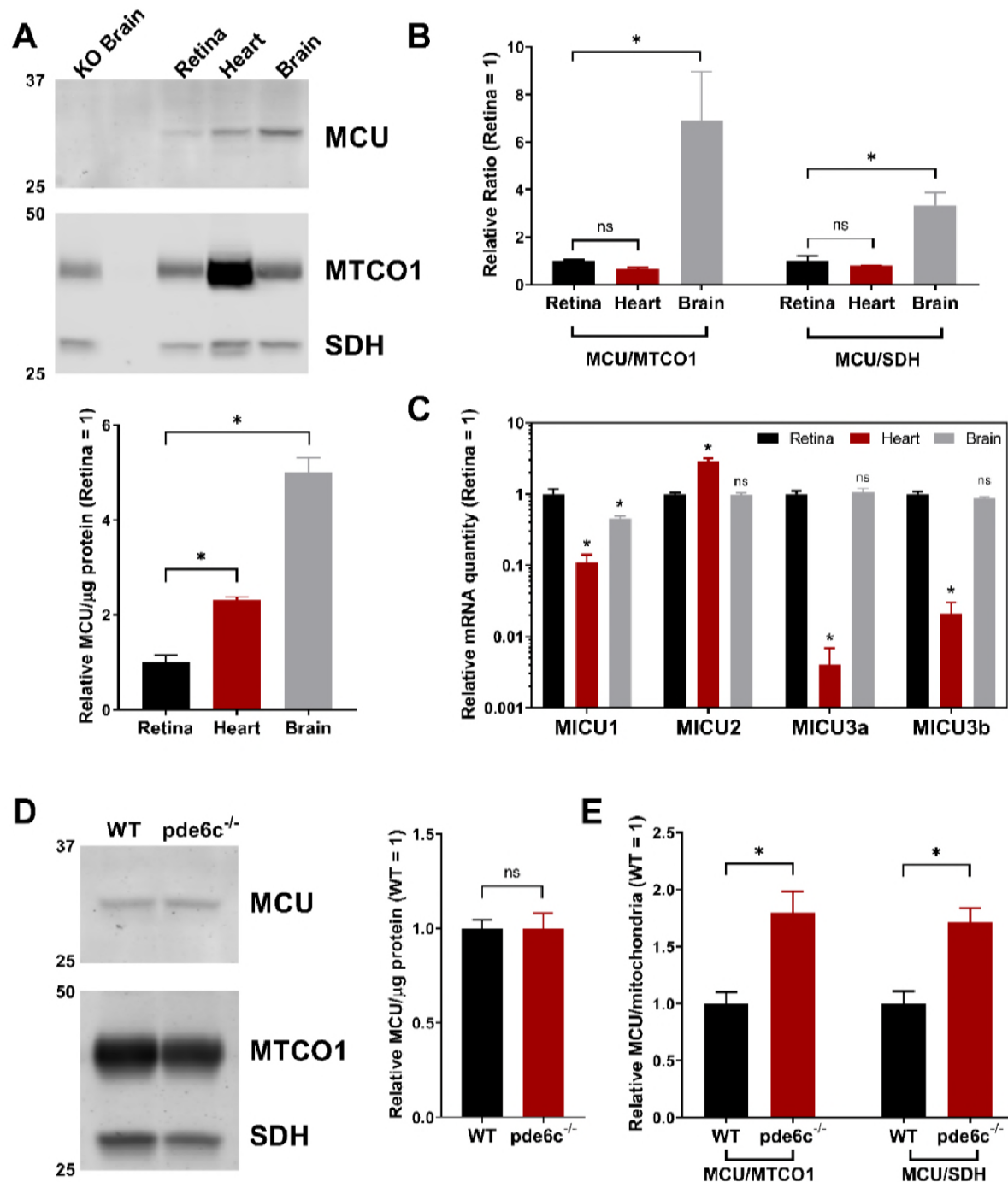


Figure 1: MCU expression is limited in the retina, particularly in cones.

A. Western blot using zebrafish MCU antibody with zebrafish tissue lysate, enriched for mitochondrial proteins and probed for MCU, mitochondrial cytochrome oxidase (MTCO1), and succinate dehydrogenase (SDH). Samples were pooled from either 4 retinas, 2 hearts, or 1 brain and performed with n=3 biological replicates of each pool. Each lane contains 8 μg of protein. Values were normalized relative to retina tissue. Bars = standard error. *p<0.05 using ANOVA followed by Dunnett post-hoc test (comparison to retina).

B. Within each lane from the gel in A, the ratios of MCU signal to the mitochondrial proteins MTCO1 and SDH were determined. Values were normalized relative to retina tissue. Bars = standard error. *p<0.05 using ANOVA followed by Dunnett post-hoc test (comparison to retina).

Figure 1 contd.

C. qRT-PCR quantification of relative mRNA of MICU proteins (relative to reference gene *Ef1α* and/or *b2m*, see methods) across retina, heart, and brain tissues. Bars = standard error. * $p < 0.05$ and ns = not significant using ANOVA followed by Dunnett post-hoc test (comparison to retina).

D. Retinal lysate, enriched for mitochondrial proteins, of WT and *pde6c*^{-/-} cone deficient retinas. Each lane is from mitochondrial-enriched lysate of two pooled retinas from a single fish, $n=4$ fish. Each lane contains 30 μ g of protein. Ns = not significant using Welch's t-test.

E. Relative quantification of the ratio MCU to mitochondrial proteins MTCO1 and SDH in WT and *pde6c*^{-/-} cone deficient retinas from the gel shown in D. * $p < 0.05$ using Welch's t-test.

138

139 **Overexpression of MCU in cones raises basal $[Ca^{2+}]$ in the mitochondrial matrix**

140 We hypothesized that low expression of MCU protein in photoreceptors could protect
 141 them from overloading their mitochondria matrix with Ca^{2+} . To test the consequences of
 142 increased MCU, we expressed MCU-T2A-RFP in zebrafish cones under control of the
 143 promoter for cone transducin ("*gnat2*" or "*TαCP*") and established a stable transgenic
 144 line overexpressing zebrafish MCU in cone mitochondria (**Figure 2A**). Cones
 145 overexpressing MCU (MCU OE) also express RFP in the cytosol, as the T2A sequence
 146 stalls the ribosome after MCU has been translated to allow MCU protein release before
 147 translation of RFP (Kim et al., 2011). Based on immunoblot analysis we found that
 148 retinal MCU protein expression is 102 ± 5 -fold higher in the MCU OE model. This also
 149 is reflected in the ratio of MCU to other mitochondrial membrane proteins (**Figure**
 150 **2B,C**). Immunohistochemistry confirmed that MCU expressed in this way is localized to
 151 cone mitochondria (**Figure 2D**).

152

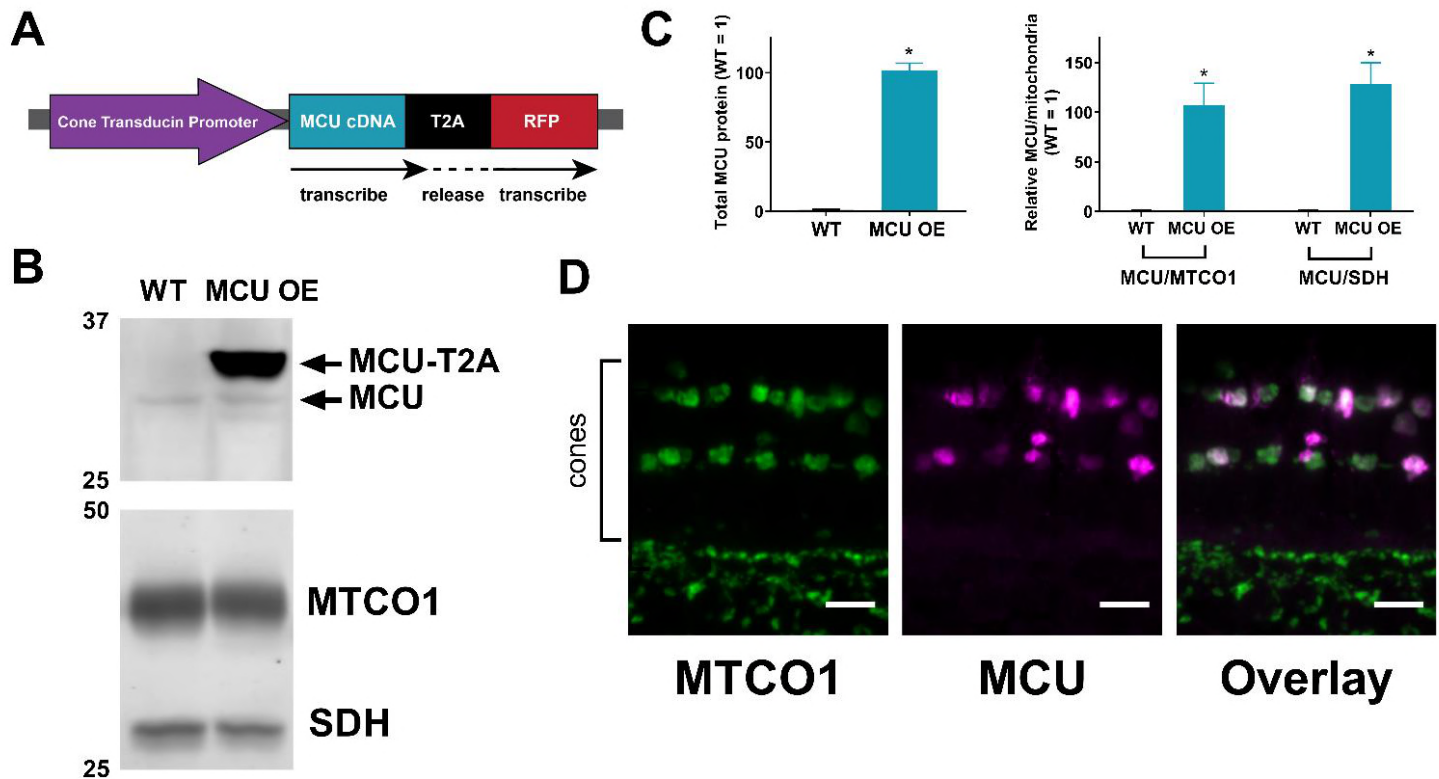


Figure 2: Successful generation of a cone-specific MCU overexpression zebrafish model.

A. Schematic of MCU OE construct. The cone transducin promoter (TαCP, *gnat2*) drives expression of zebrafish MCU cDNA in all cone subtypes. The MCU cDNA is tagged with a T2A sequence followed by RFP. The T2A sequence causes ribosomes to stall and release the nascent MCU polypeptide with some added peptides from the T2A sequence before translating the RFP separately. Thus, RFP is present in the cytosol of cones with MCU overexpression.

B. Retinal lysate, enriched for mitochondrial proteins, of WT and MCU OE retinas. Blot was probed with antibodies for MCU, MTCO1, and SDH. 8 μg of protein was loaded per well. Each lane is from mitochondrial-enriched lysate of two pooled retinas from a single fish, n=4 fish.

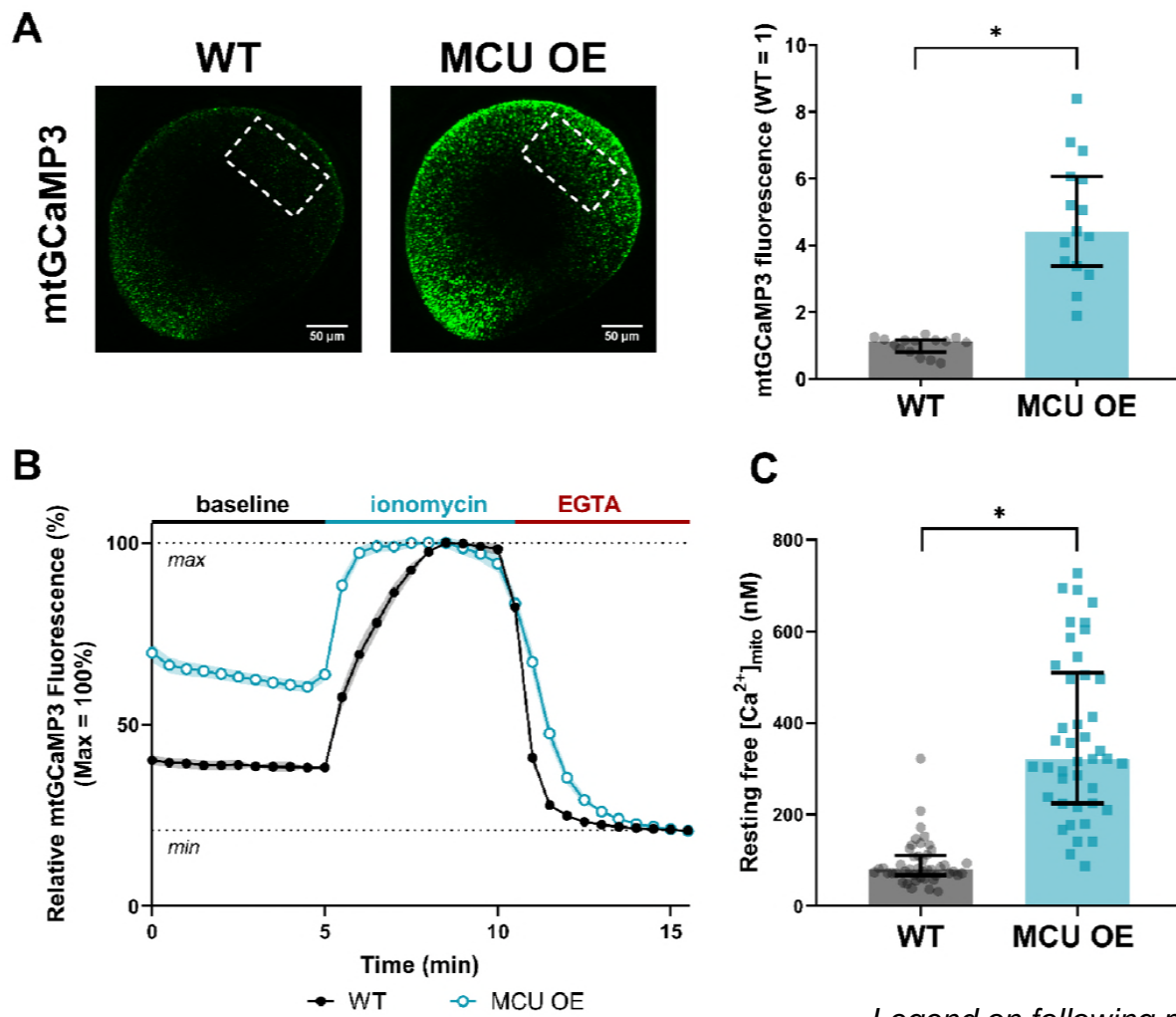
C. Quantification of relative MCU signal as a function of protein concentration and relative to other mitochondrial markers from the gel in B. Both exogenous and endogenous MCU were used for total MCU quantification in the MCU OE retina. *p<0.05 using Welch's t-test.

D. Immunohistochemistry of a larval zebrafish retina expressing the MCU construct in A using MCU and mitochondrial cytochrome oxidase (MTCO1) antibodies. Scale bar = 5 μm.

153

154 To test the effects of MCU protein overexpression on mitochondrial Ca²⁺ content, we
 155 crossed MCU OE fish with the *gnat2*:mito-GCaMP3 transgenic line, which expresses
 156 the Ca²⁺ sensor GCaMP3 in cone mitochondria (Giarmarco et al., 2017). Mito-GCaMP3
 157 fluorescence in live zebrafish larvae is 4.4 fold higher (median, Q1: 3.4, Q3: 6.06 fold) in
 158 MCU OE models compared to WT siblings (**Figure 3A**). We next prepared *ex vivo*

retinal slices (Giarmarco et al., 2018) of MCU OE *gnat2*:mito-GCaMP3 zebrafish and sibling controls. We measured the baseline mito-GCaMP3 fluorescence (F_0), the maximum fluorescence (F_{max}) with ionomycin and 2 mM Ca^{2+} , and the minimum fluorescence (F_{min}) in 5 mM EGTA (**Figure 3B**). Comparing ($F_0 - F_{min}$) to ($F_{max} - F_{min}$) indicated that the baseline GCaMP signal is operating at $20 \pm 1\%$ of maximum fluorescence in WT mitochondria and $48 \pm 2\%$ of maximum in MCU OE mitochondria. Based on these measurements, we estimate that the baseline free $[Ca^{2+}]_{mito}$ is 80.0 nM (median, with Q1: 67.1, Q3: 110.5 nM) in WT mitochondria and 320.6 nM (median, with Q1: 223.9, Q3: 509.0 nM) in MCU OE mitochondria (**Figure 3C, equation in legend**).



Legend on following page.

Figure 3: MCU overexpression in cones increases basal $[Ca^{2+}]_{mito}$.

A. Total cone mitochondrial clusters in a larval zebrafish eye expressing *gnat2:mtGCaMP3*, a mitochondrial Ca^{2+} sensor (green). Dotted outlines demarcate the region of the eye used for fluorescence quantification. Reporting the median with bars = interquartile range, $n=15$ larvae for both WT and MCU OE. * $p<0.05$ using Mann-Whitney test.

B. Relative mito-GCaMP3 fluorescence of cone mitochondrial clusters in adult retinal slices of *gnat2:mtGCaMP3* fish (WT or MCU OE). Baseline fluorescence was first assayed in the presence of KRB buffer containing 2 mM $CaCl_2$, then ionomycin (5 μ M) was added to the slice to allow 2 mM Ca^{2+} entry into the mitochondria to saturate the probe. Next, EGTA (5 mM) was added to the solution (keeping [ionomycin] constant) to chelate Ca^{2+} and establish the minimum GCaMP3 fluorescence signal. $n=45$ mitochondrial clusters (3 fish) for WT and $n=42$ mitochondrial clusters (3 fish) for MCU OE. Fish were between 3-5 months of age and slices were imaged every 30 s. Shaded region = standard error.

C. Approximation of resting free $[Ca^{2+}]$ in mitochondrial clusters assayed in B. Approximations used the equation $[Ca^{2+}] = K_D \times \frac{\theta}{1-\theta}$, where $\theta = \frac{F_0 - F_{min}}{F_{max} - F_{min}}$. We used the previously reported K_D of GCaMP3 (345 nM, from Chen et al., 2013) as an approximation for our calculation. Reporting the median with bars = interquartile range and * $p<0.05$ using Mann-Whitney test.

168

169 **Overexpression of MCU in cones reduces cytosolic Ca^{2+} transients and alters the**
170 **cone photoresponse**

171 Increased mitochondrial Ca^{2+} uptake could alter the clearance kinetics of cytosolic Ca^{2+}
172 transients. To test this, we prepared *ex vivo* retinal slices of control and MCU OE
173 *gnat2:GCaMP3* zebrafish, which express the Ca^{2+} sensor GCaMP3 in the cytosol of
174 cones. We pre-incubated the retinal slices in a 0 mM Ca^{2+} solution before introducing a
175 bolus of 5 mM $CaCl_2$. We then used timelapse imaging to monitor the clearance of
176 cytosolic Ca^{2+} from the cell body (**Figure 4A**). Consistent with increased Ca^{2+} uptake by
177 mitochondria, MCU OE cones clear Ca^{2+} from the cell body cytosol 2.3 ± 0.1 times
178 faster than their WT siblings, as determined by the decay constant of a single
179 exponential fit (**Figure 4B, Supplemental Figure 4A**). We also found that the peak fold
180 change in cone cell body GCaMP3 fluorescence in response to the Ca^{2+} bolus is lower
181 in MCU OE compared to their WT siblings (**Figure 4C**). To determine whether these
182 changes were due to Ca^{2+} uptake via MCU and not another secondary effect, we
183 incubated MCU OE retinal slices in Ru360, a drug that blocks Ca^{2+} uptake through the
184 MCU; these experiments significantly restored the WT phenotype (**Figure 4A-C**).

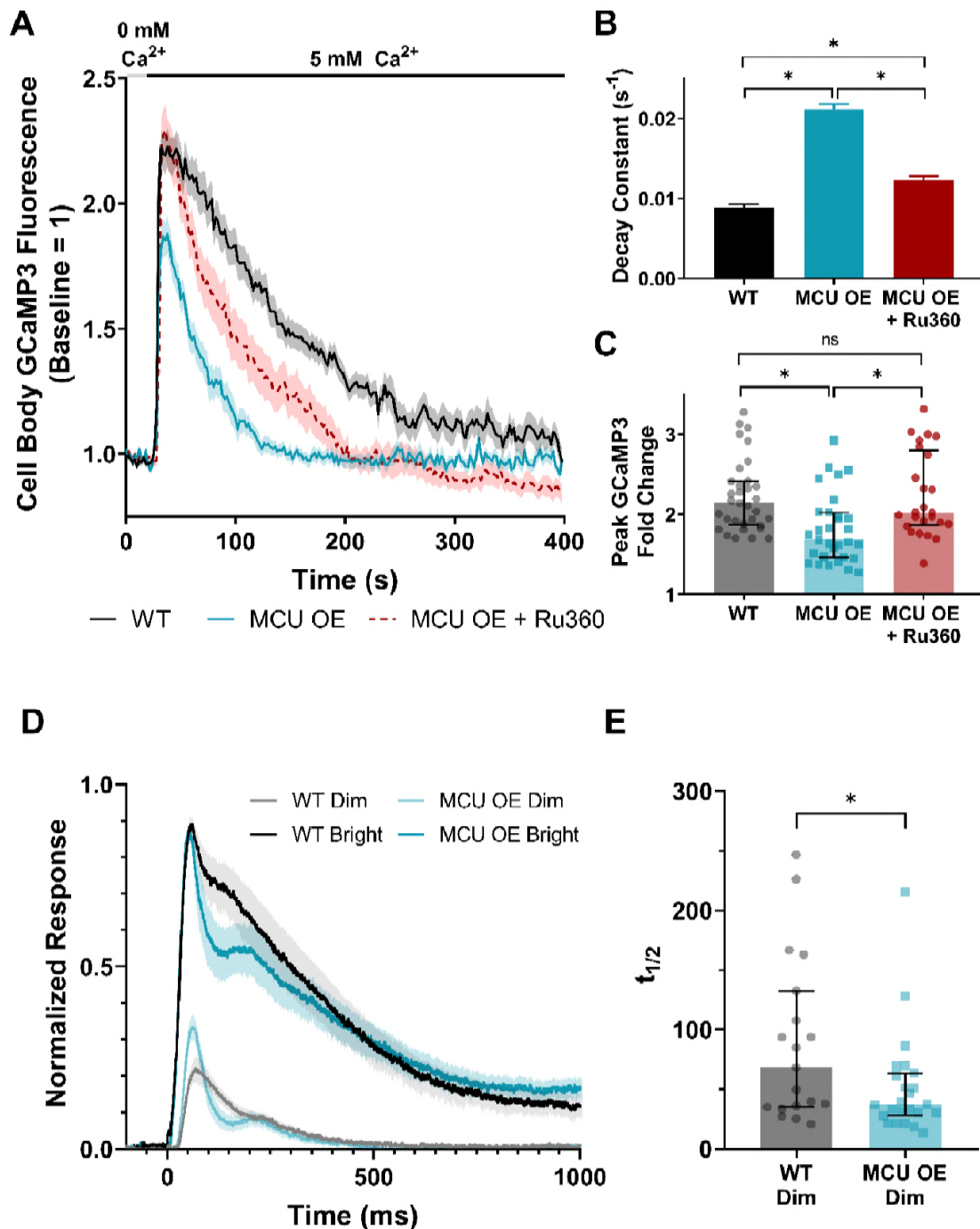


Figure 4: MCU overexpression in cones accelerates cytosolic Ca^{2+} clearance with functional consequences on the photoreceptor response to light.

A. Isolated retinas from *gnat2*:GCaMP3 fish pre-incubated in 0 mM Ca^{2+} for 10 min then subjected to a 5 mM Ca^{2+} bolus (black bar). Fish used were WT, MCU OE, or MCU OE retinas preincubated in Ru360 (100 μM) and maintained throughout the experiment. N=33 cells (7 fish) for WT, n=31 cells (7 fish) for MCU OE, n=26 cells (3 fish) for MCU OE + Ru360. Fish were between 3-5 months of age and slices were imaged every 2s. Shaded region = standard error.

B. Decay constant of Ca^{2+} clearance for experiments shown in A. Bars = standard error. * $p < 0.05$ using ANOVA followed by Tukey post-hoc test.

Figure 4 contd.

C. Peak GCaMP3 fluorescence fold-change from baseline for experiments shown in A. The median is reported and bars = interquartile range. WT: median=2.14, Q1=1.87, Q3=2.42. MCU OE: median=1.68, Q1=1.46, Q3=2.02. MCU OE + Ru360: median=2.02, Q1=1.87, Q3=2.80. * $p < 0.05$ using Kruskal-Wallis followed by Dunn post-hoc test.

D. The normalized *ex vivo* a-wave response isolated using DL-AP4 (40 μ M) and CNQX (40 μ M). Each retina response is normalized to R_{\max} , the maximum response at the brightest light intensity. N=19 retinas (11 fish) for WT siblings, n=24 retinas (14 fish) for MCU OE. Fish were 7 months of age. Shaded region = standard error.

E. Time to half maximum of the individual responses to a dim stimulus flash from data shown in D. The median is reported and bars = interquartile range. WT: median=68.1 s, Q1=34.9, Q3=132.4. MCU OE: median=37.1 s, Q1=28.2, Q3=63.0 * $p < 0.05$ using Mann-Whitney test.

186

187 Cytosolic Ca^{2+} in the photoreceptor outer segments regulates the gain of
188 phototransduction, light response recovery kinetics and light adaptation mainly via
189 GCAPs- and recoverin-mediated pathways both in rods and cones (Makino et al., 2004;
190 Mendez et al., 2001; Sakurai et al., 2011, 2015). Compared to rod photoreceptors, cone
191 phototransduction gain is smaller and cones recover faster to the dark-adapted state
192 after transient light stimulus (for recent review, see Vinberg et al., 2018). These
193 differences are believed to stem, at least partly, from the faster clearance of cytosolic
194 Ca^{2+} in cone as compared to rod outer segments (Sampath et al., 1998, 1999). We
195 asked whether overexpression of MCU would contribute to a faster clearance of Ca^{2+}
196 from the cone outer segments and consequently lead to a faster photoresponse
197 recovery. We used an *ex vivo* ERG technique to measure pharmacologically isolated
198 cone photoreceptor responses from adult WT and MCU OE retinas and found that the
199 initial phase of photoreceptor response recovery following light flashes is accelerated by
200 MCU overexpression (**Figure 4D**). This is most apparent in the dim flash responses,
201 which have a shorter time to half-maximum in MCU OE retinas (**Figure 4E**). At this age
202 (7 months) the maximal response amplitude (R_{\max}) is somewhat decreased
203 (**Supplemental Figure 4B**). However, the dim flash responses normalized to R_{\max}
204 increase, suggesting a higher gain of phototransduction in MCU OE cones (**Figure 4D**,
205 **Supplemental Figure 4C**).

206 **Retinas with MCU overexpressing cones have altered flux through the TCA cycle**

207 It has been reported that pyruvate dehydrogenase (PDH), isocitrate dehydrogenase
208 (IDH), and α -ketoglutarate dehydrogenase (α -KGDH) have higher activity in the

presence of Ca^{2+} (Denton and Randle 1972, McCormack and Denton 1979, McCormack and Denton 1990). Ca^{2+} can boost PDH activity by stimulating PDP1c, which is a subunit of the phosphatase that converts inactive phosphorylated PDH to active unphosphorylated PDH (Denton 2009). How Ca^{2+} stimulates α -KGDH and IDH is not as well understood, but it is thought that Ca^{2+} increases activity by interacting directly with these enzymes to lower the K_M for their substrates (Denton 2009).

We investigated the effect of MCU overexpression on PDP1c phosphatase activity by immunoblotting WT and MCU OE retinas with antibodies against phosphorylated PDH (P-Ser293 of E1 α) and against total E1 α . While we hypothesized MCU OE cones would have a lower P-PDH/total PDH ratio, we observed that it was instead very slightly increased (**Figure 5A, Supplemental Figure 5A**).

To investigate the effects of MCU overexpression on α -KGDH and IDH, we performed a series of metabolic flux experiments. Cones rely on glucose to fuel both aerobic glycolysis and the TCA cycle in order to meet the high energy demands required for phototransduction. We incubated WT and MCU OE retinas in U- ^{13}C -glucose, extracted metabolites, and used gas chromatography-mass spectrometry (GC-MS) to quantify ^{13}C -labeled metabolites in these pathways (**Figure 5B**). Flux through glycolysis and total metabolite levels are largely unaltered in MCU OE cones (**Supplemental Figure 5C,D**). However, the time course of ^{13}C -metabolite accumulation indicates that IDH and α -KGDH activities are enhanced (**Figure 5C**). The steady state levels of m2 citrate and m2 isocitrate are lower in MCU OE retinas compared to WT retinas. This is consistent with Ca^{2+} lowering the K_m of IDH, leading to depletion of upstream metabolites. High IDH activity alone should cause more m2 α -KG accumulation, but instead we observe similar steady state levels of m2 α -KG in MCU OE retinas and an accumulation of metabolites downstream of α -KGDH. This suggests that MCU OE retinas also have increased α -KGDH activity which is preventing the buildup of α -KG. Overall, these results are consistent with Ca^{2+} increasing activity of both IDH and α -KGDH.

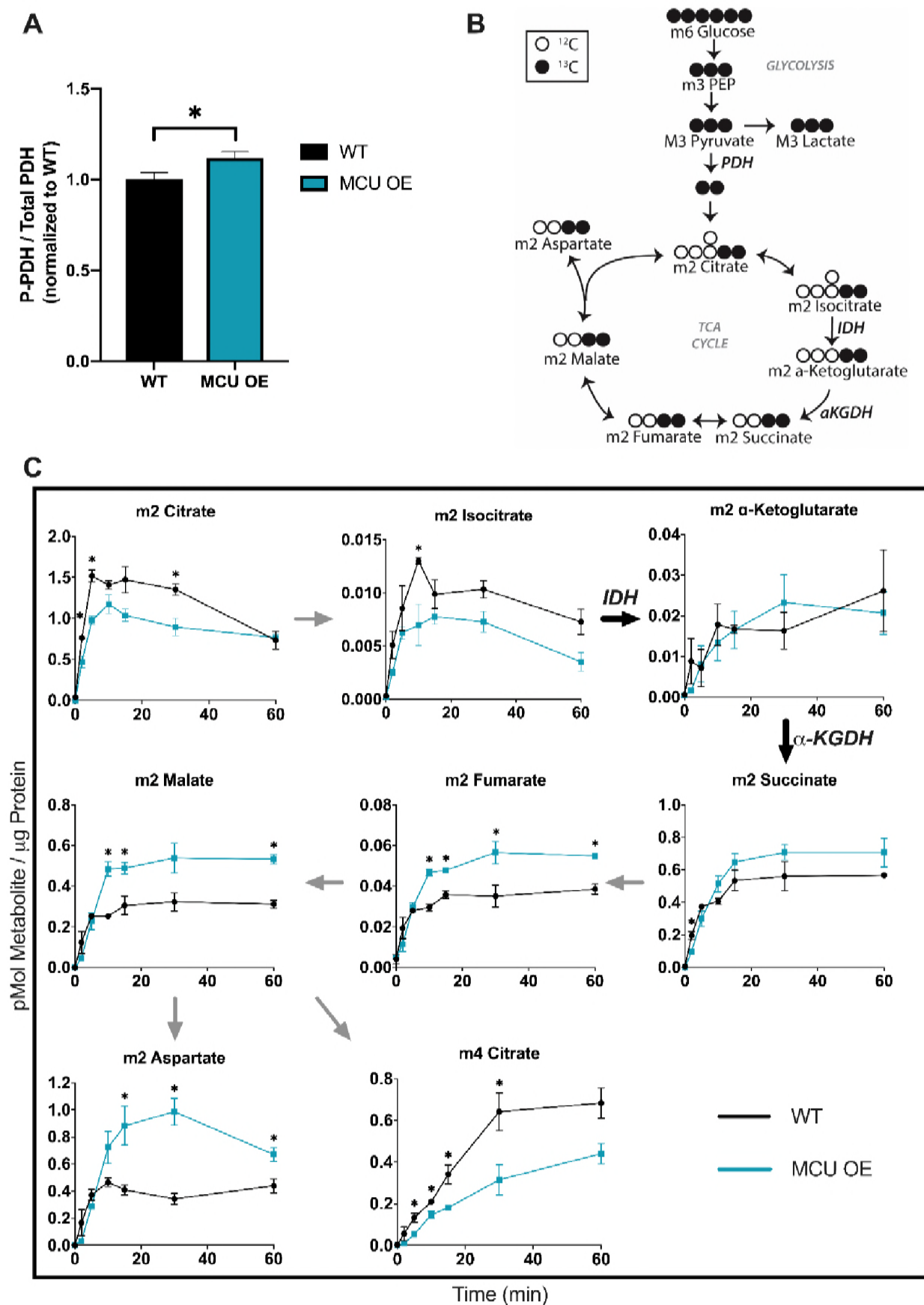


Figure 5: ^{13}C -Glucose reveals increased flux through the TCA cycle in MCU OE retinas.

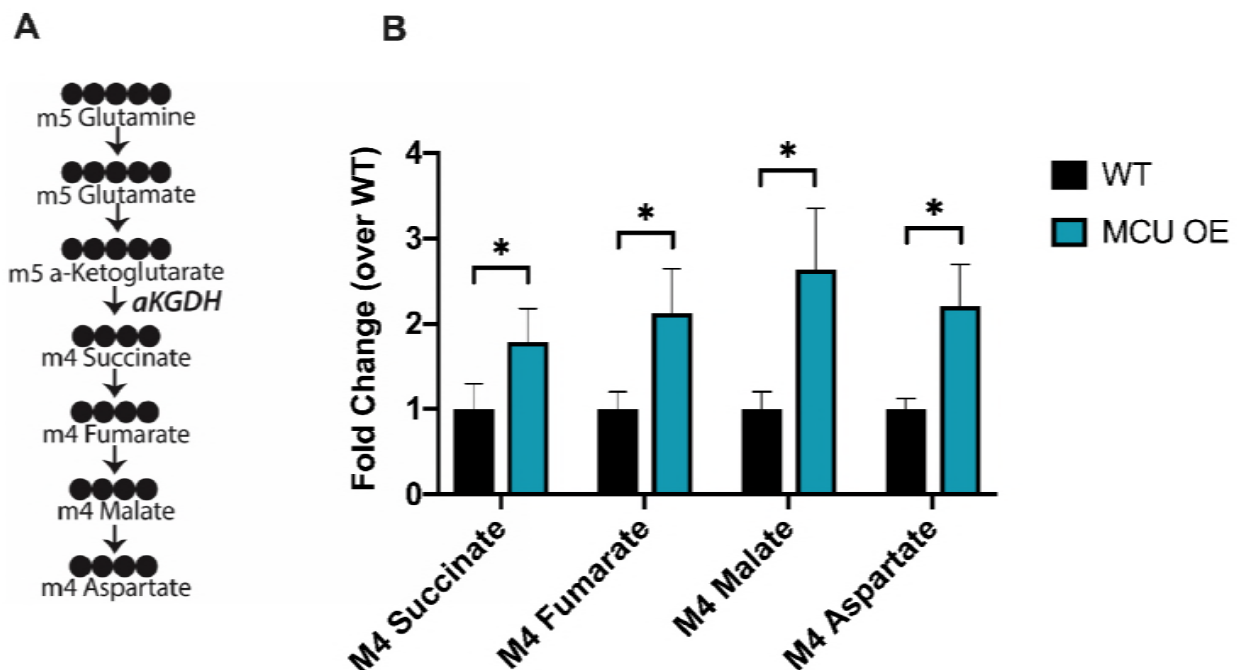
A. P-PDH/total PDH ratio from WT and MCU OE retinas, normalized to WT. MCU OE retinas have a 1.12 ± 0.02 -fold higher P-PDH/total PDH ratio than WT. $n=6$ WT and 6 MCU OE retinas. $*p<0.05$ using Welch's t-test.

B. Diagram showing how labelled carbons from U- ^{13}C -glucose are incorporated through glycolysis and the first round of the TCA cycle. Shaded = labeled carbon, empty = unlabeled carbon.

C. Levels of isotopomers in WT and MCU OE retinas. 'm' signifies the number of ^{13}C -labeled carbons in each metabolite. 'm2' TCA cycle metabolites are made from one round of the TCA cycle. Data points represent averages from $n=3$ retinas from 3 different fish. $*p<0.05$ using Welch's t-test.

237

238 While glucose is a physiologically relevant fuel for photoreceptors, it makes it difficult to
 239 observe IDH and α -KGDH activity in isolation because the two are intrinsically linked in
 240 the TCA cycle. For this reason, we next used U- ^{13}C -glutamine in the absence of glucose
 241 to bypass IDH and directly fuel α -KGDH (**Figure 6A**). Since glutamine is not a typical
 242 fuel for photoreceptors, we tested concentrations of ^{13}C -glutamine ranging from 0.1 mM
 243 to 2 mM (**Supplemental Figure 6A**). We found that at most concentrations of ^{13}C -
 244 Glutamine, MCU OE retinas produced metabolites downstream of α -KGDH at higher
 245 levels compared to WT (**Figure 6B**). Increased production of these metabolites further
 246 confirms that α -KGDH activity is higher in MCU OE cones.



247

248

Legend on following page.

Figure 6: ^{13}C -Glutamine supplementation confirms increased α -KGDH activity in MCU OE retinas.

A. Diagram showing how labelled carbons from U- ^{13}C -glutamine are incorporated into α -ketoglutarate and downstream metabolites. Shaded = labeled carbon, empty = unlabeled carbon.

B. Levels of isotopomers in WT and MCU retinas supplied with 2 mM ^{13}C -glutamine for 15 minutes. Data points represent averages from n=3 retinas from 3 different fish. * p < 0.05 using Welch's t-test.

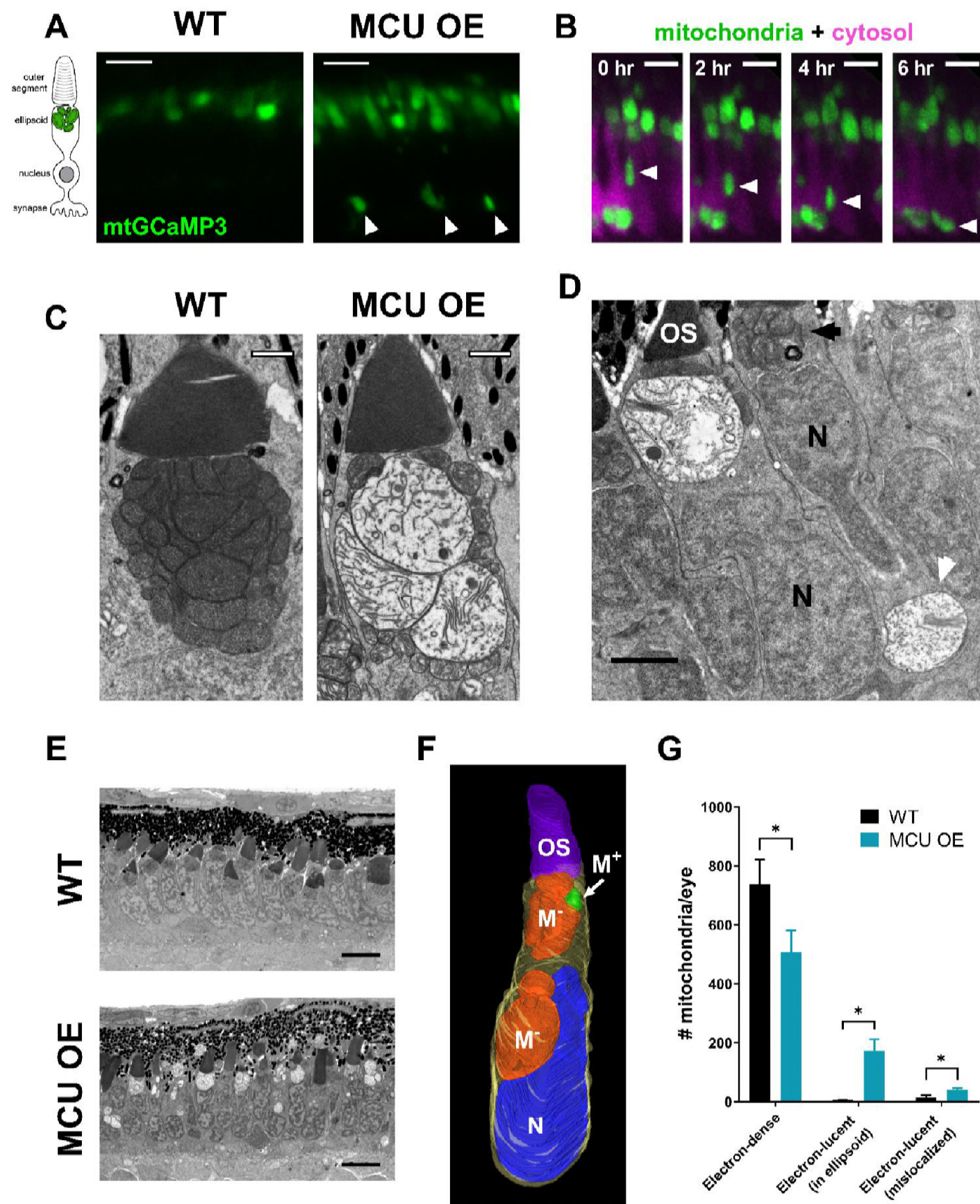
249

250 **MCU-overexpressing mitochondria are mislocalized and have abnormal**
251 **morphology**

252 In zebrafish cones, mitochondria are reported to be confined solely to the ellipsoid
253 region (Tarboush et al., 2012). However, while imaging *gnat2*:mito-GCaMP3 larvae, we
254 observed large mitochondrial clusters outside of this region in the MCU OE fish (**Figure**
255 **7A**). We recorded 8 hour time-lapses of live zebrafish larvae expressing *gnat2*:mito-
256 GCaMP3 and *gnat2*:MCU-T2A-RFP. Cytosolic RFP was included to visualize cones.
257 The timelapse recordings demonstrate directed movement of mitochondrial clusters
258 away from the ellipsoid region toward the synapse (**Figure 7B, supplemental video 1**).

259 EM analysis reveals dramatic changes in mitochondrial structure in both mislocalized
260 mitochondrial clusters and those in the ellipsoid region. Mitochondria in MCU OE cones
261 increase in size to the scale of an entire normal mitochondrial cluster, they lose
262 substantial electron density, and their cristae are disorganized (**Figure 7C**). This
263 phenotype is heterogenous; some abnormal mitochondria have internal membrane
264 stacks, clusters of electron dense material, or few internal membrane structures.
265 Furthermore, many cones contain a mix of electron-dense and -lucent mitochondria;
266 even cones containing mislocalized, electron-lucent mitochondria near the synapse can
267 also contain what appear to be healthy mitochondria at the ellipsoid region (**Figure 7D**).
268 This electron-lucent phenotype emerges soon after expression of MCU is first
269 detectable at 78 hours post-fertilization and is widespread by 120 hours post-fertilization
270 (**Figure 7E**). 3D reconstructions of MCU OE mitochondria suggest that movement of
271 electron-lucent mitochondria away from the ellipsoid region is an active process, as
272 these mitochondria deform the nucleus on their way toward the synapse (**Figure 7F,**
273 **Supplemental Video 2**).

Using electron micrographs of whole larval eyes, we quantified mitochondria that were electron-lucent in the ellipsoid region and those that were mislocalized to the nuclear layer and synapse. With the caveat that the lucent mitochondria in MCU OE models are often much larger than their healthy counterparts, we found that relative to WT cones the MCU OE cones have fewer electron-dense mitochondria and substantially more electron-lucent mitochondria both within the ellipsoid region and outside of it (**Figure 7G**). Notably, electron-dense mitochondria were never observed outside of the ellipsoid region in either WT or MCU OE cones. WT cones rarely contained electron-lucent mitochondria ($2.7 \pm 0.6\%$ of cone mitochondria); these were markedly smaller than lucent mitochondria in their MCU OE siblings (**Supplemental Figure 7A**), and most of these were mislocalized ($2.0 \pm 0.7\%$ of cone mitochondria, **Supplemental Figure 7B**). Cones containing lucent and mislocalized mitochondria were more concentrated on the dorsal side of the retina, with fewer near the periphery of the retina where new photoreceptors form (**Supplemental Figure 7C**). Overall, we found that $37.6 \pm 4.0\%$ of cone ellipsoid clusters contained electron lucent mitochondria in MCU OE larvae (**Supplemental Figure 7D**). The widespread mitochondrial swelling and mislocalization phenotype of MCU OE fish is not specific to larval development and is retained as fish mature (**Supplemental Figure 7E**).



Legend on following page.

Figure 7: Mitochondria in MCU OE cones migrate away from the ellipsoid region and exhibit swelling, loss of electron-density, and disorganized cristae.

A. Cone mitochondrial clusters in live larvae expressing *gnat2:mtGCaMP3*. WT mitochondria were imaged with higher laser settings to show localization. In MCU OE models, mitochondrial clusters were found near the synapse and nuclear layer (white arrows), which was not observed in WT siblings. Scale bar = 5 μ m.

B. Timelapse of a migrating mitochondrial cluster (green, white arrow) in live MCU OE *gnat2:mtGCaMP3* larvae. Cone cell bodies express cytosolic RFP (magenta). MCU OE mitochondrial clusters slowly move from the ellipsoid region down to the synapse. Full video in supplemental data. Scale bar = 5 μ m.

C. EM images of cone mitochondria in WT sibling and MCU OE fish at 1 month of age. Mitochondria in MCU OE cones exhibit swelling, loss of electron density, and disorganized cristae. Scale bar = 1 μ m.

D. A single cone photoreceptor can contain both healthy mitochondria in the ellipsoid region (black arrow) and electron-lucent mitochondria near the synapse (white arrow). Electron micrograph from MCU larvae at 14 days of age. Scale bar = 2 μ m. OS = outer segment, N = nucleus.

E. Electron micrograph of MCU cones at 120 hours of age. Scale bar = 5 μ m.

F. 3D reconstruction of an MCU OE cone using serial block-face EM (synapse not shown). Electron-lucent mitochondria displace the nucleus of the cone to move toward the synapse region. OS = outer segment. M⁻ = electron-lucent mitochondria. M⁺ = healthy mitochondria. N = nucleus. Outline (yellow) = cell body.

G. Quantification of cone mitochondrial phenotypes from EM images of whole zebrafish larval eyes (single slice at optic nerve) at 6 days of age. MCU OE cones have fewer “healthy” electron-dense mitochondria, and an increase in lucent mitochondria both in the ellipsoid and outside of this region. All mislocalized mitochondria observed had an electron-lucent phenotype. n=3 larvae for both WT and MCU OE fish. *p<0.05 using a t-test with the Holm-Sidak correction for multiple tests.

294

295 **Cones overexpressing MCU survive throughout early adulthood, but eventually**
296 **degenerate**

297 Despite the early emergence of mitochondrial abnormalities, we noted that larval cones
298 otherwise remain intact and other retinal cell morphology is unperturbed (**Supplemental**
299 **Figure 8A**). Fluorescent imaging of Tg(*gnat2:GFP*) fish showed that cones are
300 conserved as zebrafish reach maturity at 3 months of age and throughout early
301 adulthood despite their severely altered mitochondrial structure. However, some
302 morphological disturbances (shorter cones and disorganized alignment) are apparent at
303 these earlier ages. Severe cone degeneration eventually occurs later in adulthood; the
304 cone number decreases, and many remaining cones round up and lose their outer
305 segment integrity (**Figure 8A,B**). Rods remain intact and healthy rod outer segments
306 persist even when cone loss is extensive (**Figure 8B, black arrowhead**).

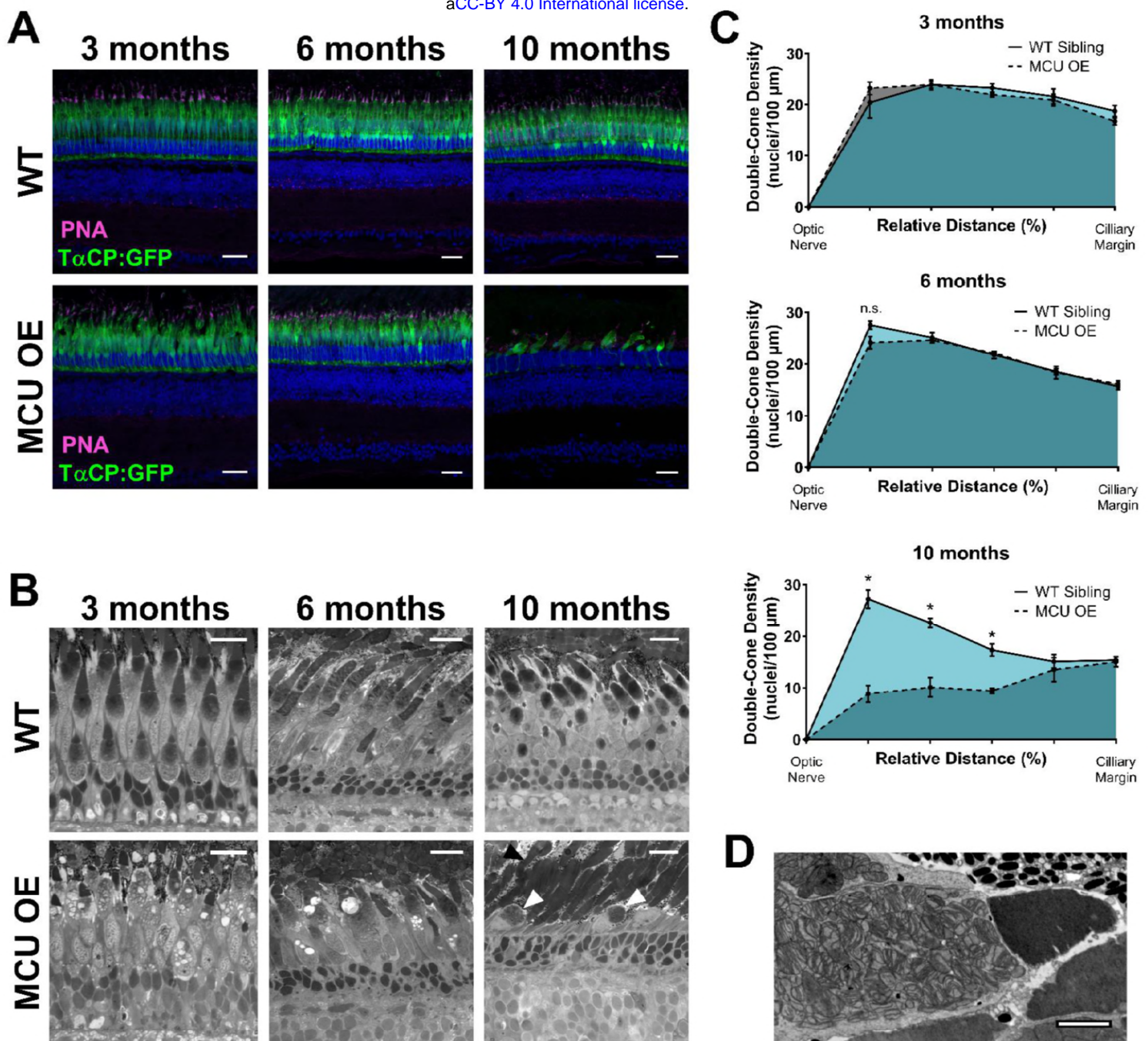


Figure 8: Cones overexpressing MCU survive well into early adulthood, but extensive loss is observed in late adulthood.

A. WT sibling and MCU OE retinas stained with Hoescht (blue) and exhibiting fluorescence from *gnat2*:GFP in all cone types (green) at 3 months, 6 months, and 10 months of age. Cone outer segments are labelled with α -PNA (magenta). Scale bar = 25 μ m.

B. WT sibling and MCU OE retinas stained with Richardson's stain at 3 months, 6 months, and 10 months of age. Swollen mitochondria can still be visualized in 3 month and 6 months cones. By 10 months, the cones are very few and have severe morphological disturbances (white arrow); however, rod mitochondria and outer segments remain intact (black arrow). Scale bar = 25 μ m.

C. Quantification of double-cone nuclei from the optic nerve to the ciliary margin in WT and MCU OE fish. Counts are an average of dorsal and ventral retinal slices in each fish, $n = 3$ WT and 3 MCU OE fish. * $p < 0.05$ using a t-test with Holm-Sidak correction for multiple tests.

D. Electron micrograph of fragmented mitochondria in a cone from 10-month-old MCU OE fish. We observed that many of the remaining cones at 10 months have severe mitochondrial fragmentation rather than the electron-lucent phenotype. Scale bar = 2 μ m.

Quantification of double-cone nuclei, which are most easily distinguished from rod nuclei, revealed that cones in the MCU OE model are preserved at 3 months and 6 months, but severe cone loss occurs by 10 months (**Figure 8C, Supplemental Figure 8B**). Cone loss is consistently most apparent near the optic nerve; cones are only appreciably observed at the ciliary zone of the 10 month MCU OE zebrafish retina, where new cones form. Many of the remaining cones in the MCU OE model have severe mitochondrial fragmentation rather than large electron-lucent mitochondria (**Figure 8D**). Mitochondrial fragmentation is often associated with apoptosis (Frank et al., 2001; Lee et al., 2004; Youle and Karbowski, 2005). Cones in MCU OE models do not re-populate to WT density after 10 months, but rods remain intact and abundant (**Supplemental Figure 8C**). Notably, in 1 year old WT sibling retinas, there are multiple cones with large, electron-lucent mitochondria in the clusters; these were similar in appearance to MCU OE electron-lucent mitochondria (**Supplemental Figure 8D**).

Discussion

Photoreceptors in normal human retinas are remarkable in their ability to survive the entire human life span. Although perturbations to Ca^{2+} homeostasis are implicated in many degenerative diseases, normal photoreceptors can withstand the large intracellular Ca^{2+} fluctuations that occur during normal photoreceptor function. Identification of the MCU protein has allowed us to investigate its role in a biological context; the abundance of direct and indirect regulators of MCU and variability in expression of these regulators across tissues necessitates empirical, cell-type-specific study. Here we investigated the influence of MCU expression on cone photoreceptor function and survival. Our findings demonstrate an important role of mitochondrial Ca^{2+} uptake in regulating functional and structural aspects of cone photoreceptors. This work also reveals a surprising resistance of photoreceptors to the stress caused by elevated mitochondrial matrix Ca^{2+} . Our results indicate that in photoreceptors, homeostatic adaptive responses to high matrix Ca^{2+} are robust.

337 *Effect of MCU OE on Ca²⁺ homeostasis and the functional consequences*

338 Our findings suggest that MCU expression is a limiting factor in basal cone
 339 mitochondrial Ca²⁺ uptake, as overexpression of MCU increases the resting
 340 concentration of free Ca²⁺ in the mitochondrial matrix. EMRE, required for Ca²⁺ uptake
 341 via MCU in vertebrates, does not seem to be limiting in cones; this is consistent with a
 342 recent study demonstrating that EMRE is produced in excess and degraded when MCU
 343 is not present (Sancak et al., 2013, Tsai et al., 2017). Enhancing mitochondrial Ca²⁺
 344 uptake in cones reduces the amplitude and duration of Ca²⁺ transients in the cell body,
 345 where mitochondria reside. However, only partial restoration to WT levels can be
 346 achieved in the MCU OE model by pharmacologically inhibiting MCU. This could be due
 347 to factors other than mitochondrial Ca²⁺ uptake being affected in the MCU OE model
 348 (such as ER Ca²⁺ levels), insufficient permeability of Ru360 into cells, or an abundance
 349 of MICU1/MICU3 which can block Ru360 binding to MCU (Paillard et al., 2018).

350 Extrusion of Ca²⁺ from the outer segment of photoreceptors is thought to be
 351 accomplished primarily by plasma membrane Na⁺/Ca²⁺, K⁺ exchangers NCKX1 in rods,
 352 and NCKX2 and NCKX4 in cones (for recent review, see Vinberg et al., 2018).
 353 However, *Nckx1*^{-/-} rods appear to clear cytosolic Ca²⁺ through a slower, yet unidentified
 354 mechanism (Vinberg et al., 2015a). Moreover, cones that are deficient of both NCKX2
 355 and NCKX4 can respond to light, light-adapt, and degenerate rather slowly, suggesting
 356 that there is an additional NCKX-independent pathway that clears Ca²⁺ from cone outer
 357 segments (Vinberg et al., 2017). The faster clearance of cytosolic Ca²⁺ by mitochondria
 358 in MCU OE cones is accompanied by accelerated photoresponse recovery, consistent
 359 with faster Ca²⁺ clearance. These results suggest that MCU may be the NCKX-
 360 independent mechanism that contributes to the clearance of Ca²⁺ from the cone outer
 361 segment.

362 Increased light sensitivity of MCU OE cones (**Supplemental Figure 5C**) is surprising
 363 considering that the inactivation of cone phototransduction was faster in these cones.
 364 The gain of cone phototransduction activation reactions, normally thought to be Ca²⁺-
 365 independent, is somehow increased by altered Ca²⁺ homeostasis due to MCU

overexpression. We also found that the maximal light response amplitude was decreased in MCU OE cones (**Supplemental Figure 5B**), possibly due to misalignment or loss of cones at the age tested (7 months). Altogether, these functional changes demonstrate that mitochondrial Ca^{2+} uptake in photoreceptors can modulate the kinetics of the photoreceptor response to light, independent of neurotransmitter release and downstream responses. It is likely that this phenomenon is not restricted to zebrafish or cones, as human patients with mtDNA diseases have delayed recovery of the rod photoreceptor response (Cooper et al., 2002).

Effect of MCU OE on mitochondrial metabolism in the retina

Since photoreceptors experience the highest levels of intracellular Ca^{2+} in darkness when O_2 consumption is highest, Ca^{2+} could play an important role in stimulating increased TCA cycle activity (Okawa Fain 2008, Krizaj Copenhagen 2002). We have previously observed that photoreceptors have higher α -KGDH activity in darkness (Du Rountree 2015). Here, we observe that both IDH and α -KGDH are stimulated by increasing Ca^{2+} in cone mitochondria, which supports this hypothesis.

An increase in the P-PDH/total PDH ratio is a common metabolic phenotype in MCU KO tissues, so we initially hypothesized that increasing mitochondrial Ca^{2+} would decrease the P-PDH/total PDH ratio by stimulating PDP1c (for a review of metabolic phenotypes in MCU KO tissues see Mammucari, Raffaello 2018). However, we found that this was not the case. Since the P-PDH/total PDH ratio also does not decrease when MCU is overexpressed in muscle cells, it is possible that changes in mitochondrial bioenergetics resulting from increased mitochondrial Ca^{2+} feed into the complex regulation of PDH (Mammucari, Gherardi 2015). For example, stimulation of α -KGDH and IDH activity may result in higher NADH levels in MCU OE cones, which in turn stimulates PDH kinase to balance increased PDP1c activity.

Effect of MCU OE on mitochondrial homeostasis and subsequent cell death

While some of our results align with predicted consequences of increased mitochondrial Ca^{2+} uptake, our work also revealed some surprising observations. The most

unexpected finding in MCU OE models was the presence and selective movement of electron-lucent mitochondria away from the ellipsoid region of cones toward the synapse. We also occasionally observed electron-lucent structures that appeared to be mislocalized mitochondria in WT fish, especially in older animals (**Supplemental 7A,B; Supplemental 8D**). We hypothesize that this mechanism of mitochondrial sorting and movement occurs in normal cones, but it is more active in MCU OE models due to extensive mitochondrial disruption. This hypothesis is strengthened by recent work with the mito-QC mouse showing photoreceptor mitochondria that were being recycled by lysosomes were specifically present in the outer nuclear layer, away from the ellipsoid region (McWilliams et al., 2016). Additionally, mitochondria in rod-specific Nrf1 KO mice were observed near the outer limiting membrane of rods, away from the ellipsoid region (Kiyama et al., 2018). Many of the models of mitochondrial localization focus on how cytosolic Ca^{2+} changes predicate mitochondrial movement, concentrating mitochondria in high Ca^{2+} regions (Barnhart, 2016; Chen and Sheng, 2013; MacAskill et al., 2009; Wang and Schwarz, 2009). However, mitochondrial matrix Ca^{2+} and interactions between MCU and the transport protein Miro1 may also play a role in mitochondrial movement (Chang et al., 2011; Niescier et al., 2013, 2018). These studies, along with our findings, highlight the need for further investigation of the role of mitochondrial Ca^{2+} content and subsequent stress in selective, directed mitochondrial movement.

We initially suspected that the swollen, electron-lucent mitochondria in MCU OE cones were a manifestation of Ca^{2+} overload that would subsequently trigger apoptosis and rapid loss of cones. Mitochondria undergoing the permeability transition that precedes apoptosis exhibit excessive osmotic swelling and loss of electron density similar to the changes that are observed in MCU OE cones (Elustondo et al., 2016; Hunter et al., 1959; Zoratti and Szabò, 1995). Remarkably, MCU OE cones survive until late adulthood despite their abnormal morphology and electron-lucent mitochondria. This finding suggests that cones are particularly resistant to mitochondrial stress that would trigger apoptosis in other cell types. Furthermore, the occasional presence of large, electron-lucent mitochondria in WT retinas as the zebrafish mature (**Supplemental Figure 8D**) suggests that this phenotype may even be a symptom of cumulative mitochondrial stress in cones as they age. This phenomenon is unlikely to be specific to

zebrafish cones, as large, electron-lucent mitochondria also have been observed in aging cones in human retinas (Nag and Wadhwa, 2016). Increased resistance to mitochondrial stress may be an adaptation necessary for cones, which need to meet excessively high energetic demands throughout a lifetime.

Future Directions, Limitations, and Broader Impact

Despite the network of regulatory proteins that influence Ca^{2+} flux through MCU, solely altering MCU protein levels can influence mitochondrial Ca^{2+} and cell function. Overexpression of MCU in cortical neurons exacerbates excitotoxic cell death (Qiu 2013). However, overexpression of MCU does not always result in negative consequences. Overexpressing MCU in muscle cells increases their size and protects them from denervation-induced atrophy, and increasing MCU expression in diabetic heart models improves cardiac function (Mammucari et al., 2015; Suarez et al., 2018). MCU activity varies significantly across tissues, as does protein expression of MCU and its regulators (Fieni et al., 2012; Plovanich et al., 2013; Raffaello et al., 2013). It is likely that the consequences of MCU overexpression depend on the presence of its regulators. The MICU1:MCU ratio appears to be critical in regulating the mitochondrial response to Ca^{2+} transients; muscles, with the lowest MICU1:MCU ratio of characterized tissues, notably benefit from MCU overexpression (Mammucari et al., 2015; Paillard et al., 2017). Our qPCR results suggest that the retina has high ratios of MICU1:MCU and MICU3:MCU compared to other neural tissues, which would imply that the limited MCU channels present in the retina are primed for highly efficient Ca^{2+} uptake via a MICU1-MICU3 dimer. This could explain why MCU overexpression causes such massive perturbations in cones compared to other tissues. Future studies will characterize the functional roles of MICU1 and MICU3 in retinal cells.

A key finding from our study is that cones are highly tolerant of mitochondrial stress. 100-fold overexpression of MCU is far above the amount of MCU normally present in retina. It is possible that some of the phenotypes of the MCU OE model are secondary effects of excess protein, such as stress on the ubiquitin-proteasomal system. However, the effects of MCU OE on cytosolic Ca^{2+} and the citric acid cycle are consistent with

previous studies on mitochondrial Ca^{2+} , suggesting many of the phenotypes observed were linked to increased mitochondrial Ca^{2+} uptake.

Overall, our work supports a model in which cone photoreceptors maintain low MCU to fine-tune the many changes associated with increased mitochondrial matrix Ca^{2+} and protect from Ca^{2+} -associated mitochondrial disruption. The cone MCU OE model can also be used in future studies to elucidate a mechanistic explanation behind selective sorting of abnormal mitochondria and the adaptations triggered to maintain viability and functionality despite chronic stress. Even more broadly, the distinct localization of mitochondria in zebrafish cones makes the MCU OE model an attractive system to study basic cellular processes underlying mitochondrial movement.

Materials and Methods

Zebrafish Maintenance. Experiments with zebrafish were authorized by the University of Washington and University of Utah Institutional Animal Care and Use Committees. All fish used in this analysis were maintained in the University of Washington South Lake Union aquatics facility or the Centralized Zebrafish Animal Resource (CZAR) at the University of Utah at 27.5C on a 14 h/10 h light/dark cycle, and were maintained in the Roy^{-/-} genetic background. All wild-type fish (WT) used in analysis were age-matched siblings to Tg(gnat2:MCU-T2A-RFP) fish (MCU OE) or age-matched siblings to pde6c^{w59} (pde6c^{-/-}) (Stearns et al., 2007). Fish used for slice preparation, protein quantification, and metabolomics analysis were male and female siblings between 3 and 6 months of age. Fish used in ERG analysis were male and female siblings collected at 7 months of age. For histological analysis, ages of sibling fish are included in the figure and legend.

Zebrafish MCU antibody. The cDNA encoding amino acids 21 – 202 of *Danio rerio* MCU (NM_001077325) was cloned downstream of GST using the pGEX-2T (GE) expression vector. Overexpression was induced in *E.coli* (BL21) by addition of 1mM IPTG at 0.2 OD followed by incubation with vigorous shaking for 5h at 37° C. The tiny fraction of soluble fusion was purified using glutathione sepharose following the manufacturer's instructions (GE Healthcare). Polyclonal antibodies were generated using injections of 0.5 – 1mg protein (R and R Research Co.). Two columns were used to clean the serum. One column contained total *E.coli* proteins covalently coupled to cyanogen bromide beads and the second column contained purified GST protein coupled to cyanogen bromide beads (GE Healthcare). Serum was cleaned by sequential incubations of 3 – 5 hours at room temperature with each column after which it was analyzed on an SDS page gel for lack of cross reactivity with GST and *E.coli* proteins from a total cell extract. Identification of MCU was validated by the absence of a protein of the correct molecular weight in extracts obtained from a CRISPR generated KO strain. The zebrafish MCU antibody was used at a dilution of 1:750 for western blotting and 1:50 for immunohistochemistry.

Zebrafish models. The transgenic zebrafish lines Tg(gnat2:GCaMP3), Tg(gnat2:EGFP), and Tg(mito-GCaMP3) have been described previously (Giarmarco et al., 2017; Kennedy et al., 2007; Ma et al., 2013). Generation of the global MCU KO line was performed using gRNA with the following sequence 5'-CCTCATACCTGGTGCAGCCCCC-3' using methods as previously described (Brockerhoff, 2017). For generation of the Tg(gnat2:MCU-T2A-RFP) line, zebrafish MCU cDNA was isolated from WT zebrafish larvae (5 dpf) using the forward primer 5'-AGAGATGGCTGCGAAAAGTGT-3' and reverse primer 5'-TTCTCATCAGTCCTTGCTGGT-3'. Overhang qPCR methods in conjunction with Fast-Cloning were used to add the T2A ribosomal stalling sequence and the RFP protein coding sequence; this was cloned into a pCR8/GW vector (Invitrogen) (Li et al., 2011). Plasmids were assembled using the Gateway-Tol2 system (Villefranc et al., 2007). Expression of MCU-T2A-RFP was driven by the cone transducin alpha promoter (TaCP, gnat2), and the RFP coding sequence was flanked by a polyA tail sequence to increase transcript stability (Kennedy et al., 2007). A destination vector with a sBFP2 heart marker for aid in transgenic identification was obtained from Cecilia Moens (Kremers et al., 2007). The fully assembled construct was injected into embryos at the 1-cell stage with Tol2 transposase mRNA. Larvae mosaic for the transgene were raised to adulthood to identify founder carriers. A single F₀ founder was used to generate F₁ fish that were screened for a single insertion of the transgene; F₂ fish from two F₁ substrains with a single insertion were used for analysis in this study.

Primers for qRT-PCR. All designed primers were empirically tested to confirm primer efficiency was between 90-110%. Only primers passing this benchmark were used for analysis. Primer sequences for the reference genes *EF1a*, *b2m*, *Rpl13a*, and *TBF* were identical to previous reports testing zebrafish reference gene stability (*EF1a*, *Rpl13a*: (Tang et al., 2007), *b2m*, *TBP*: (McCurley et al., 2008)).

Elongation Factor 1 alpha (EF1a):
Forward: 5'-CTGGAGGCCAGCTCAAACAT-3'
Reverse: 5'-ATCAAGAAGAGTAGTACCGCTAGCATTAC-3'

523 Beta-2-microglobulin (b2m):

524 Forward: 5'-GCCTTCACCCCAGAGAAAGG-3'

525 Reverse: 5'-GCGGTTGGGATTTACATGTTG-3'

526 Ribosomal protein L13a (Rpl13a):

527 Forward: 5'-TCTGGAGGACTGTAAGAGGTATGC-3'

528 Reverse: 5'-AGACGCACAATCTTGAGAGCAG-3'

529 TATA-box-binding protein (TBP):

530 Forward: 5'-CGGTGGATCCTGCGAATTA-3'

531 Reverse: 5'-TGACAGGTTATGAAGCAAAACAACA-3'

532 MICU1:

533 Forward: 5'-ACGTTAAAGCAGAATCGTAGAGG-3'

534 Reverse: 5'-CGCAAGCGGTACATATCAGAC-3'

535 MICU2:

536 Forward: 5'-ACTGAGTACCTGTTTCTCCTCAC-3'

537 Reverse: 5'-GGTCCATTTACTTTCTTCAGCTTCT-3'

538 MICU3a:

539 Forward: 5'-CGTCCCATGAGCATCGTTTC-3'

540 Reverse: 5'-TCCAACCTCCTGTTTGGTGAGG-3'

541 MICU3b:

542 Forward: 5'-GCTTGGTGCAAGAATAGTTCTCTTT-3'

543 Reverse: 5'-TGCAGGTTGTCCATGAATCTGT-3'

544 **qRT-PCR.** An Applied Biosystems 7500 Fast Real-Time PCR System in conjunction
 545 with iTaq™ Universal SYBR® Green Supermix (Bio-Rad, 1725120) was used for qPCR
 546 measurements according to the manufacturer's instructions. The reference genes *EF1a*,
 547 *b2m*, *TBF*, and *rpl13a* were screened across the tissue panel using NormFinder to
 548 identify reference genes with the highest stability (Andersen et al., 2004). NormFinder
 549 identified the combination of *EF1a* and *b2m* as most stable for retina-brain comparisons

and *EF1a* as most stable for retina-heart comparisons. Quantification of relative mRNA quantity used 3 biological replicates of each tissue, each performed in technical triplicate. From each technical triplicate, the average C_t value for the gene of interest and reference gene(s) were used to generate a ΔC_t value for each biological replicate. Comparing each tissue of interest to the retina generated a $\Delta\Delta C_t$ value; these were converted to a normalized expression level using the $2^{-\Delta\Delta C_t}$ method (Livak assumptions). Standard error of the ΔC_t value for each tissue was propagated to the final comparison using standard error propagation rules. Calculations were based off the geNorm method of qPCR normalization (Vandesompele et al., 2002).

Commercial antibodies and stains.

Mitochondrial cytochrome oxidase, MTCO1 (Abcam, ab14705, RRID:AB_2084810).
Used in IHC and immunoblotting at 1:1000 dilution.

Succinate dehydrogenase B, SDHB (Abcam, ab14714, RRID:AB_301432).
Used in IHC and immunoblotting at 1:1000 dilution.

Pyruvate Dehydrogenase E1 subunit, PDH (Abcam, ab110334, RRID:AB_10866116)
Used in immunoblotting at 1:1000 dilution.

Phosphorylated Pyruvate Dehydrogenase E1 subunit Ser293, P-PDH (EMD Millipore, ABS204, RRID:AB_11205754)
Used in immunoblotting at 1:2000 dilution.

Pyruvate Kinase, PK (Abcam, ab137791)
Used in immunoblotting at 1:1000 dilution.

Hoechst 33342, Trihydrochloride, Trihydrate stain (ThermoFischer, H3570).
Used in IHC at 5 μ M concentration.

Lectin PNA Alexa Fluor 647 conjugate (ThermoFischer, L32460).
Used in IHC at 1:200 dilution after suspending at a concentration of 1 mg/mL in H₂O.

Goat Anti-Mouse IgG H&L, Alexa Fluor 488 (Abcam, ab150113, RRID:AB_2576208).
Used in IHC at 1:1000 dilution.

577 Goat Anti-Rabbit IgG H&L, Alexa Fluor 647 (Abcam, ab150083, RRID:AB_2714032).
578 Used in IHC at 1:1000 dilution.

579 IRDye 800CW donkey anti-rabbit IgG (H+L) (LI-COR Biosciences, 925-32213, RRID:
580 AB_2715510).
581 Used at 1:5000 dilution for immunoblotting.

582 IRDye 680RD donkey anti-mouse IgG (H+L) (LI-COR Biosciences, 925-32212, RRID:
583 AB_2716622).
584 Used at 1:5000 dilution for immunoblotting.

585 IRDye 680RD donkey anti-rabbit IgG (H+L) (LI-COR Biosciences, 925-68073,
586 RRID:AB_2716687).
587 Used at 1:5000 dilution for immunoblotting.

588 IRDye 800CW goat anti-mouse IgG (H+L) (LI-COR Biosciences, 925-32210,
589 RRID:AB_2687825).
590 Used at 1:5000 dilution for immunoblotting.

591 **Mitochondrial enrichment and sample preparation for immunoblotting.** Organs
592 were snap-frozen in liquid nitrogen after collection, then homogenized with a dounce
593 homogenizer in 50 mM Tris buffer containing sucrose (200 mM), NaCl (150 mM), and
594 EGTA (1 mM) with a protease inhibitor mini tablet (ThermoFischer, 88666).
595 Homogenized samples were centrifuged at a low speed of 1,000 x g for 10 minutes at
596 4°C, then the supernatant (containing mitochondria) was collected and centrifuged at a
597 high speed of 17,000 x g for 45 minutes. The supernatant was discarded and the pellet
598 (containing mitochondria) was homogenized for 1 minute in RIPA buffer. Homogenized
599 mitochondria were sonicated on ice for three 5 second pulses. A standard BSA assay
600 using Pierce™ BCA Protein Assay Kit (ThermoFischer, 23225) was performed
601 according to the manufacturer's instructions for protein concentration determination.
602 Samples were diluted with RIPA buffer to ensure an equal volume and equal protein
603 concentration of each sample could be loaded into wells for immunoblotting.

Immunoblotting. Samples were loaded into wells on 12-14% acrylamide gels made in-house. Each sample contained 20% 5X SDS buffer containing β -mercaptoethanol. After running the gel at 150V for 1 hr, gels were transferred onto PVDF membranes (Millipore, IPFL00010) and blocked for 1 hr at room temperature in LI-COR Odyssey Blocking Buffer (LI-COR, 927-40000). Primary antibodies were diluted in blocking buffer at specified concentrations and incubated overnight at 4°C. Membranes were washed with PBST and PBS, then incubated with secondary antibody for 1 hr at 25°C and washed again before imaging. Membranes were imaged and bands were quantified using the LI-COR Odyssey CLx Imaging System (RRID:SCR_014579).

Immunohistochemistry (IHC) and degeneration quantification. All adult eyes were isolated from light-adapted zebrafish, and a small incision in the cornea was made to allow 4% paraformaldehyde fixative to enter the eye. Whole larvae were euthanized then incubated in 4% paraformaldehyde. After fixation overnight at 4°C, eyes were rinsed in PBS then subject to a sucrose gradient (20% and 30%), embedding in OCT, and cryosectioned at 12 μ m. For sections stained with MCU antibody, antigen retrieval was performed by steaming sections in 10 mM sodium citrate (0.05% Tween-20, pH 6.0). Sections were washed in PBS, then blocked in PBS containing 5% donkey serum, 2 mg/mL bovine serum albumin, and 0.3% Triton X-100 for 1 hr. Primary antibodies were diluted in this buffer as specified, then applied to cryosection overnight at 4°C. Secondary antibodies were diluted as specified and applied to section for 1 hr in darkness at 25°C. For PNA-labelled samples, sections were incubated in diluted PNA-647 for 30 minutes at 25°C. Tissues were washed, incubated in Hoescht stain for 10 minutes, then mounted in Fluoromount-G® (SouthernBiotech, 0100-01) under glass coverslips. Slides were imaged using a Leica LSP8 confocal microscope with a 63X oil objective. Leica LAS-X software (RRID:SCR_013673) was used to acquire images.

For quantification of cone nuclei in *gnat2*:GFP fish, high-resolution images of whole zebrafish retina slices were stitched together using ImageJ Grid/Collection stitching (Preibisch et al., 2009). Both the dorsal and ventral regions of the retina were straightened along the cone nuclei axis using ImageJ from the optic nerve to the ciliary margin. This axis was divided into 5 equal parts, then double-cone nuclei were counted

in each region, normalizing to the length in μm (height of the region was equal across samples, double cone nuclei are along a single axis). GFP was used to confirm that the double-cone nuclei counted were indeed cone nuclei. All counting was performed blinded (masked) to sample identity.

Live larval imaging of mtGCaMP3. Larvae used for imaging were maintained in embryo media containing 0.003% 1-phenyl 2-thiourea (PTU, Sigma-Aldrich P7629) starting at 20 hours post-fertilization. Live zebrafish larvae were analyzed at 6 days postfertilization (dpf) by transferring to 0.5% low melting point agarose containing embryo media with 0.003% PTU and 0.02% (w/v) Tricaine (Sigma-Aldrich, E10521). Larvae were positioned in agarose in a petri dish containing embryo media and 0.02% (w/v) tricaine to prevent drying out. Imaging of slices was performed using an Olympus FV1000 in conjunction with Olympus FluoView FV10-ASW software (RRID:SCR_014215). A 40X water objective was used for imaging. The excitation/emission wavelengths used for mito-GCaMP3 were 488/510 nm. Timelapse images of live larvae were collected with a z-depth of 2 μm and were collected every 20 minutes. Images of total eye mitochondrial clusters were also collected at a z-depth of 2 μm . For quantification of total mito-GCaMP3 fluorescence, images of whole larval eyes were collected, and a fixed ROI centered on the nasal region of the retina was used for quantification. This region near the ventronasal patch is comprised of the most mature cone photoreceptors (Schmitt and Dowling, 1999).

Retinal slice imaging of GCaMP3 and mito-GCaMP3. Slices were prepared as described previously (Giarmarco et al., 2017, 2018). For GCaMP3 cytosolic clearance experiments, slides were preincubated in KRB containing 0 mM Ca^{2+} and 0.4 mM EGTA for 10 minutes. Images of single optical slices were collected every 2 seconds. A 5 mM CaCl_2 bolus (accounting for EGTA) was injected into the slice imaging chamber 30s after the initial timelapse collection to establish baseline fluorescence. These experiments in the MCU-overexpressing fish were additionally performed in the presence of Ru360 (Millipore, 557440) at 100 μM , in which slices were incubated for 1 hr prior to incubation in 0 mM Ca^{2+} media. Retinas treated with Ru360 were maintained in Ru360 throughout timelapse experiments. Dying cells near the cut edge that were

constitutively loaded with Ca^{2+} and cells that did not respond to Ca^{2+} were not included in analysis.

For mito-GCaMP3 timelapse experiments, z-stacks of 15, 2 μm slices were collected every 30 seconds. Retinal slices in modified KRB containing 2 mM CaCl_2 were first imaged for 5 minutes to establish baseline mito-GCaMP3 fluorescence. Next, the chamber was injected with ionomycin (Sigma, 407950) to a final concentration of 5 μM (prepared in DMSO, at a final concentration of 0.1%) for another 5 minutes of image collection. Finally, an excess of EGTA (5 mM) was injected to chelate the 2 mM Ca^{2+} present in solution and images were collected for another 5 minutes. Dying cells containing fragmented mitochondrial clusters constitutively loaded with Ca^{2+} and clusters that did not respond to ionomycin were not included in analysis. Additionally, any clusters where the maximum fluorescence signal in the presence of ionomycin was completely saturated were excluded from analysis.

The excitation/emission wavelengths used for both GCaMP3 and mito-GCaMP3 were 488/510 nm. Timelapses were analyzed using ImageJ + Fiji software (SCR_002285). Images were corrected for X-Y drift using the MultiStackReg plugin of ImageJ. For both cell body GCaMP3 and mito-GCaMP3 fluorescence ex vivo timelapses, fixed ROIs were used to quantify average fluorescence signal across the cluster/cell at every time point. Fluorescence of cytosolic GCaMP3 for timelapse analysis are reported as F/F_0 , where F_0 is the baseline fluorescence. For mito-GCaMP3 fluorescence, the relative fluorescence at maximum was set to 100% for normalization. We used the equation $[\text{Ca}^{2+}] = K_D \times \frac{\theta}{1-\theta}$, where $\theta = \frac{F_0 - F_{\min}}{F_{\max} - F_{\min}}$ to approximate $[\text{Ca}^{2+}]_{\text{mito}}$, where F_0 is the average “baseline” fluorescence, F_{\max} is maximum fluorescence upon ionomycin addition, and F_{\min} is the baseline fluorescence upon EGTA addition. We approximated the K_D of GCaMP3 at 345 nM (from Chen et al., 2013) for the calculation.

Electroretinograms (ERG). Zebrafish were briefly dark-adapted (~30min), before euthanization by icewater immersion. Eyes were enucleated into Modified Salamander Ringer’s solution(mM): NaCl 110, KCl 2.5, CaCl_2 1.0, MgCl_2 1.6, HEPES 10.0, Glucose 10.0, with pH adjusted to 7.8 with NaOH. The eyes were hemisected and retina isolated

from the eyecup. All procedures after the dark adaptation were performed under dim red light. *Ex vivo* Electroretinogram (ERG) recordings were performed as described previously (Vinberg and Kefalov, 2015b). Isolated retinas were mounted photoreceptor side up onto the specimen holder (Vinberg et al., 2014), and perfused with Modified Salamander Ringer's solution, supplemented with 40 μ M DL-AP4 (Tocris Bioscience) and 40 μ M CNQX (Tocris Bioscience) to isolate the photoreceptor component of the ERG signal (A-wave). The rate of perfusion was ~5 ml/min. and the experiments were conducted at room temperature (~23 °C).

ERG signal was first amplified (100X) and low-pass filtered at 300 Hz by a differential amplifier (DP-311, Warner Instruments), and data was acquired at 10KHz using a Sutter IPA amplifier/digitizer (Sutter Instrument, CA). A High-Power LED light source (Solis-3C, Thorlabs, Newton, NJ), with filter for red light (630 nm, Semrock, Rochester, NY) and LED driver (DC2200, Thorlabs) were used to provide the flashes of light stimuli, durations ranged from 5-100ms. The SutterPatch software (SutterPatch v1.1.2, Sutter Instrument, CA) drove both stimulus generation and data acquisition via the IPA amplifier's analogue output and input, respectively. Light stimuli were calibrated before experiments using a calibrated photodiode (FDS100-CAL, Thorlabs, Newton, NJ) and flash intensities converted to photon/ μ m².

Data analysis, including statistical analysis and figure preparation, was performed with GraphPad v 8.00 (for Windows, GraphPad Software, CA, USA). Normalized responses were calculated for each retina by dividing the response amplitude data by the maximal amplitude measured at the peak/plateau of the response to the brightest flash.

Metabolic flux analysis. Krebs-Ringer bicarbonate (KRB) buffer optimized for flux analysis (Du, Linton, Hurley 2013a) was used in these experiments. Zebrafish retinas were first dissected in KRB buffer containing U-¹²C-glucose or U-¹²C-glutamine at the same concentration they would be incubated in. After dissection, retinas were placed in dishes of pre-warmed KRB containing either U-¹³C glucose (5 mM, Cambridge Isotopes, CLM-1396) or U-¹³C glutamine (0.1 - 2 mM, Cambridge Isotopes, CLM-1822). Retinas were incubated in this solution for the specified time points at 28°C in a NAPCO Series

8000 WT CO₂ incubator (5% CO₂), then washed in ice-cold PBS and flash frozen in liquid nitrogen. Metabolites from each time point were extracted using ice-cold 80% MeOH and lyophilized. Two-step derivatization was performed by the addition of 20 mg/mL Methoxyamine HCl dissolved in pyridine, followed by *tert*-butyldimethylsilyl. Metabolites were analyzed on an Agilent 7890/5975C GC-MS as described extensively in previous work (Du et al., 2013a, 2013b, 2015, 2016). Metabolic flux experiments were repeated a minimum of twice, using three retinas from three different zebrafish for each condition in each experiment. Data shown are results from one representative experiment.

Electron microscopy and Richardson's staining. Adult zebrafish eyes were enucleated and a small incision was made in the cornea to allow fixative (4% glutaraldehyde in 0.1 M sodium cacodylate buffer, pH 7.2) to enter the eye. Tissues were stored at 4°C before postfixation in osmium ferrocyanide (2% osmium tetroxide/3% potassium ferrocyanide in buffer) for 1 hr, followed by incubation in 1% thiocarbohydrazide for 20 min. Samples were then incubated in 2% osmium tetroxide for 30 min at RT, and stained with 1% aqueous uranyl acetate overnight at 4°C. Samples were next stained en bloc with Walton's lead aspartate for 30 min at 60°C, dehydrated in a graded ethanol series, and embedded in Durcupan resin. Sections of tissue were cut at 60 nm thickness and imaged using a JEOL JEM-1230 transmission electron microscope or Zeiss Sigma VP scanning electron microscope. Samples of larval zebrafish eyes were imaged in conjunction with a Gatan 3View2XP ultramicrotome apparatus to generate stacks of EM images, which were aligned using TrakEM2 software (RRID:SCR_008954). Position in the eye for EM imaging was confirmed by cutting slices of tissue and staining with Richardson's stain (Richardson et al., 1960). These slices were imaged for histological analysis using a Nikon Eclipse E1000 with a Nikon Plan Apo 100X/1.40 DIC lens. Nikon ACT-1 software was used for image capture.

Statistics. Numerical results in text are reported as mean \pm standard error of the mean unless otherwise stated. Statistical tests were performed using Graphpad Prism v 8.00 software. For statistical analysis, replicates (n) were always defined as biological replicates. Information on what constitutes n (e.g. larvae, retinas, cells) is listed in the figure legend of each experiment. Samples sizes were estimated based on previous experiments (Sakurai et al., 2015; Giarmarco et al., 2017; Du et al., 2016). For data sets with sufficient n to analyze population distribution, tests for normality were administered (Anderson-Darling, D'Agostino & Pearson, Shapiro-Wilk, Kolmogorov-Smirnov). For data sets that did not pass a majority of normality tests, the median is instead reported along with the interquartile range (Q1 and Q3).

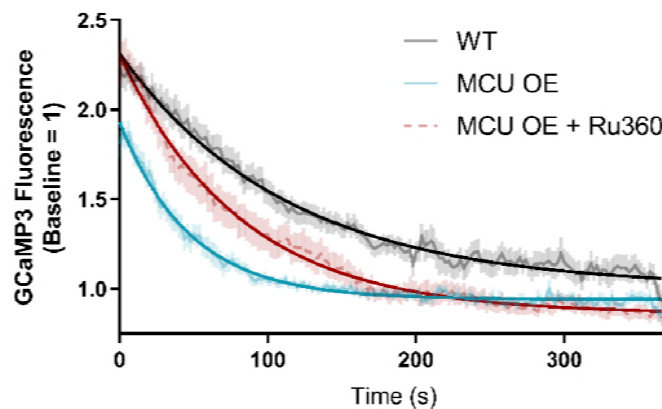
Acknowledgements

We thank Stanley Kim, Jeanot Muster, and Ashlee Evans for assistance in zebrafish husbandry and maintenance at the University of Washington South Lake Union aquatics facility (ISCRM Aquatics Facility). We would also like to acknowledge the Centralized Zebrafish Animal Resource (CZAR) at the University of Utah for providing zebrafish husbandry, laboratory space, and equipment to carry out portions of this research. Expansion of the CZAR is supported in part by NIH grant # 1G20OD018369-01. This work was supported by PHS NRSA T32GM007270 from NIGMS (RAH); NIH grants NEI EY026020 (JBH and SEB), NEI EY028645 (SEB) and P30EY001730 (UW Vision Core). This work was additionally supported by NIH EY014800 (John A. Moran Eye Center), and an Unrestricted Grant from Research to Prevent Blindness, New York, NY, to the Department of Ophthalmology & Visual Sciences, University of Utah.

Competing Interests

The authors declare no competing financial interests.

A Single Exponential Fits of Ca^{2+} Clearance

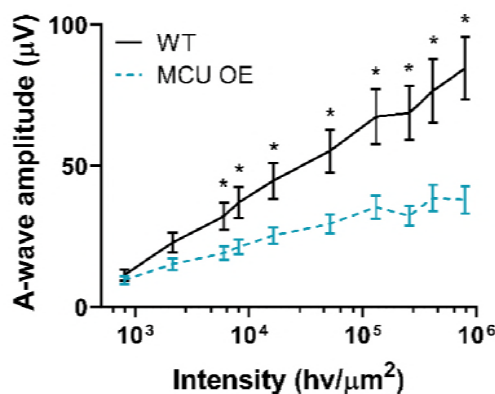


Comparison of Fits			
Null hypothesis	K same for all data sets		
Alternative hypothesis	K different for each data set		
P value	<0.0001		
Conclusion (alpha = 0.05)	Reject null hypothesis		
Preferred model	K different for each data set		
F (DFn, DFd)	99.60 (2, 13176)		

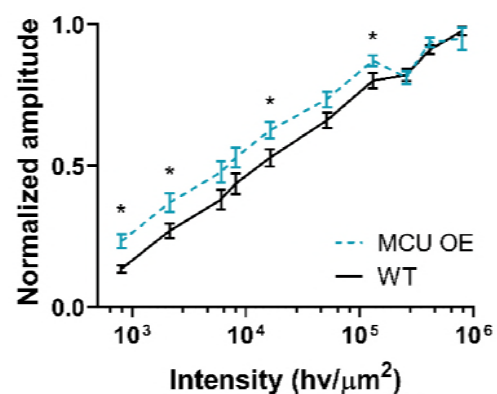
Best-fit Values	WT	MCU OE	MCU OE + Ru360
Y_0	2.314	1.929	2.308
Plateau	1.007	0.9411	0.8592
K	0.008876	0.02114	0.01233
Half Life	78.10	32.79	56.19
Tau	112.7	47.31	81.07
Span	1.306	0.9875	1.449

Std. Error	WT	MCU OE	MCU OE + Ru360
Y_0	0.01950	0.01651	0.02322
Plateau	0.02252	0.005540	0.01133
K	0.0004332	0.0006568	0.0004314
Span	0.02222	0.01592	0.02165

B



C



Supplemental Figure 4: Fitting of Ca^{2+} clearance data and other ERG parameters.

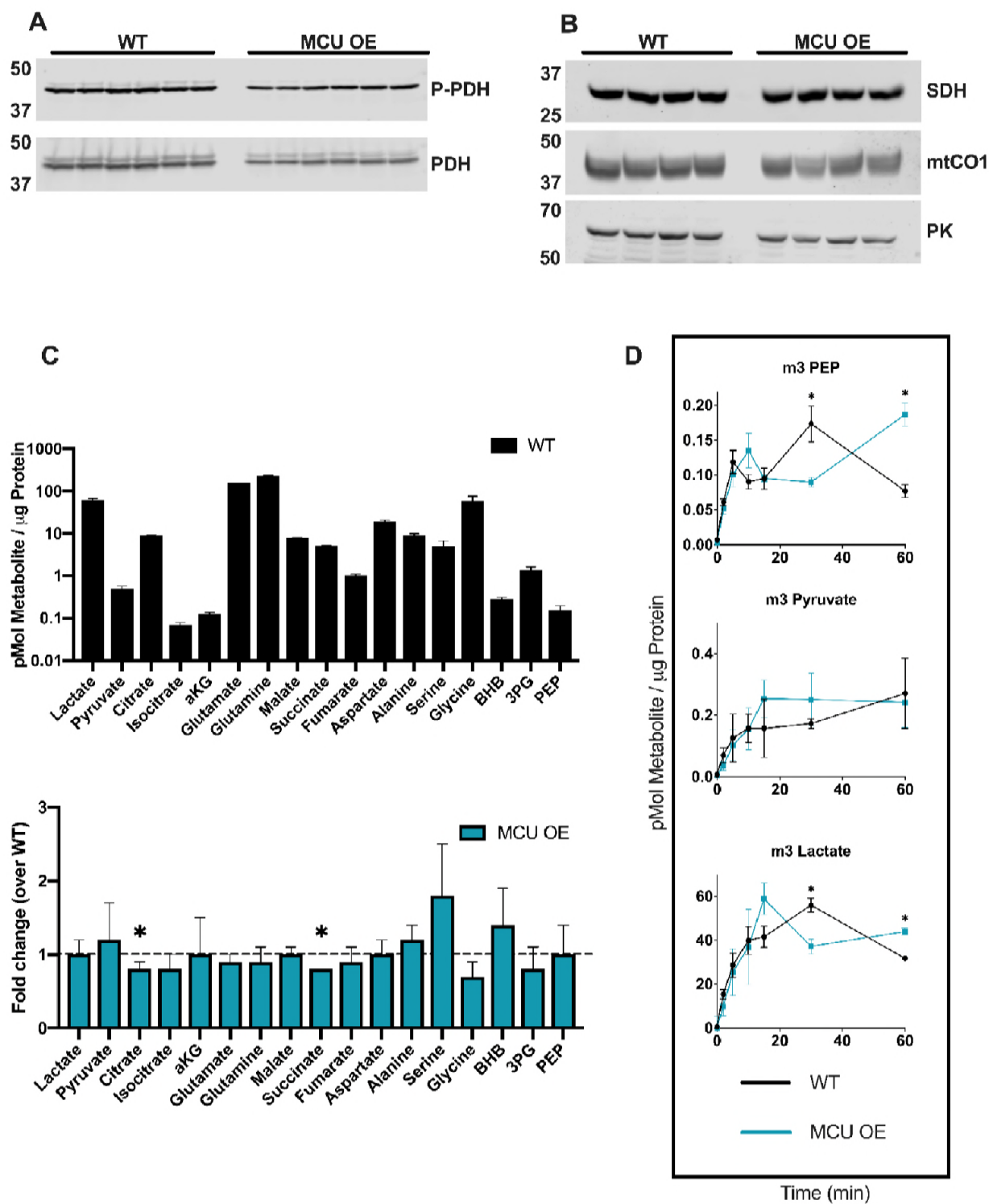
A. Truncated Ca^{2+} clearance data used for fitting with a one-phase exponential decay function (least squares fit) in GraphPad Prism 8.0.1. The fitted exponentials are shown by a solid, dark line. No constraints were included for Y_0 or the plateau, $K > 0$. K is different for each data set, with $p < 0.0001$. Descriptive statistics of the fit included in table.

B. Absolute amplitude of the isolated a-wave response to varying intensity light of WT and MCU OE retinas for experiments shown in Figure 4D. Bars = standard error. * $p < 0.05$ using Welch's t-test.

C. Amplitude of a-wave responses in WT and MCU OE retinas normalized to the maximum response for experiments shown in Figure 4D. Bars = standard error. * $p < 0.05$ using Welch's t-test.

775

Legend on following page.



776

Supplemental Figure 5: Total metabolites and glycolytic flux in MCU OE retinas.

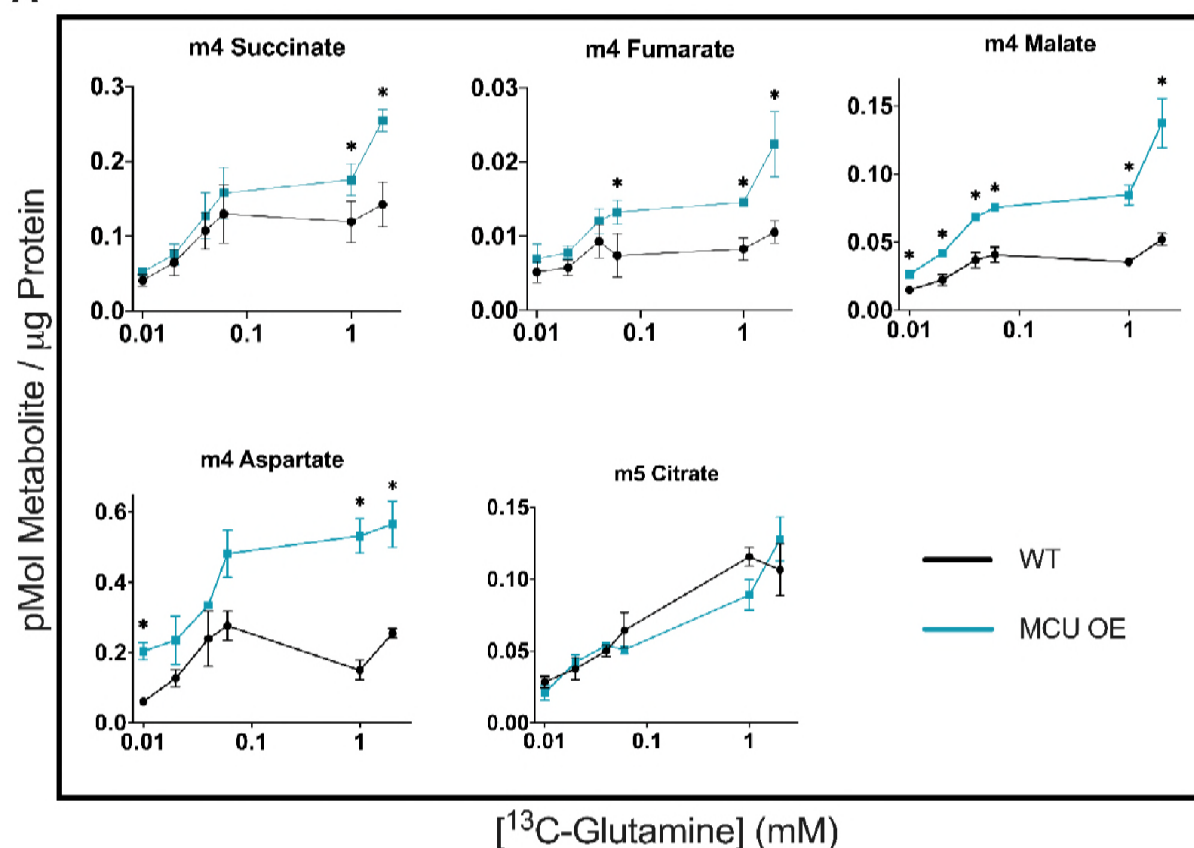
A. Immunoblot showing P-PDH and total PDH expression in WT and MCU OE retinas. n=6 WT and 6 MCU OE retinas from 3 different fish.

B. Immunoblot of mtCO1, SDH, and Pyruvate Kinase (PK) in WT and MCU OE retinas. We observed that expression of every protein we probed for (PDH, SDH, mtCO1 and pyruvate kinase) was slightly lower in MCU OE retinas, even when the same amount of protein lysate was loaded. We hypothesize that this is due to the fact that in MCU OE retinas, MCU and RFP comprise a much larger fraction of the total protein, so other proteins appear less abundant when normalizing to total protein. n=4 WT and 4 MCU OE retinas from 4 different fish.

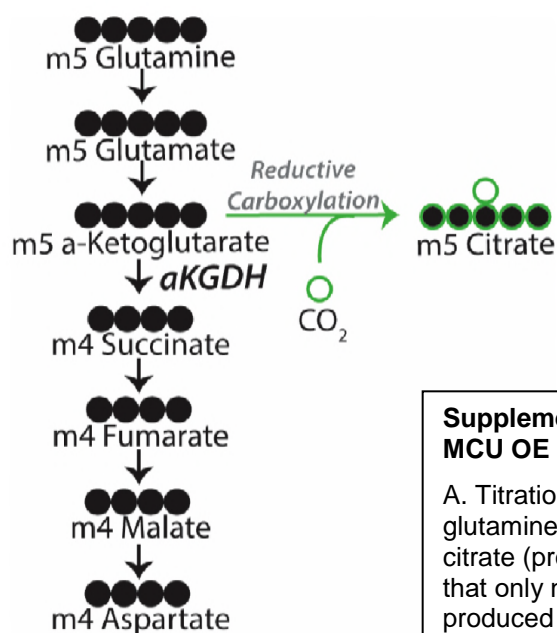
C. Total metabolite levels in freshly dissected WT zebrafish retinas and relative levels of these metabolites in MCU OE retinas. (BHB: β -hydroxybutyrate, 3PG: 3-phosphoglycerate, PEP: phosphoenolpyruvate).

D. Glycolytic intermediates from WT and MCU OE retinas supplied with ^{13}C -glucose. We observed no trends of altered glycolytic flux over time between WT and MCU OE retinas. * $p < 0.05$ using Welch's t-test.

A



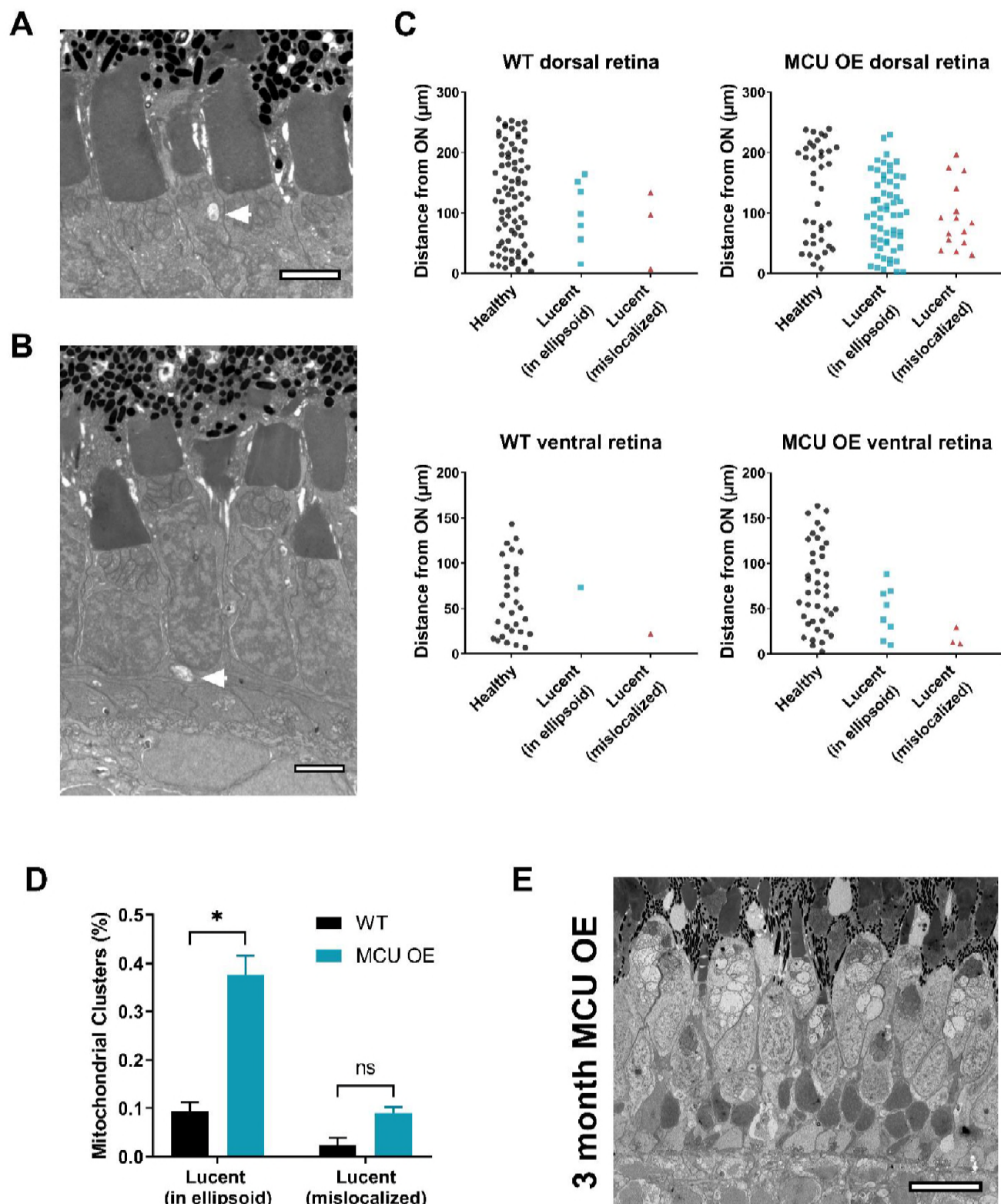
B



Supplemental Figure 6: ^{13}C -Glutamine titration in WT and MCU OE retinas.

A. Titration of WT and MCU OE retinas supplied with ^{13}C -glutamine (0.1, 0.2, 0.4, 0.6, 1, and 2 mM) for 15 minutes. m5 citrate (produced from reductive carboxylation) is included to show that only metabolites directly downstream of α -KGDH are produced at higher levels in MCU OE cones. Data points represent averages from $n=3$ retinas from 3 different fish. * $p<0.05$ using Welch's t-test.

B. Diagram showing how labelled carbons from U- ^{13}C -glutamine are incorporated into α -ketoglutarate and downstream metabolites, including through reductive carboxylation (green outline).



779

780

Legend on following page.

Supplemental Figure 7. Further characterization of electron lucent mitochondria in WT and MCU OE retinas.

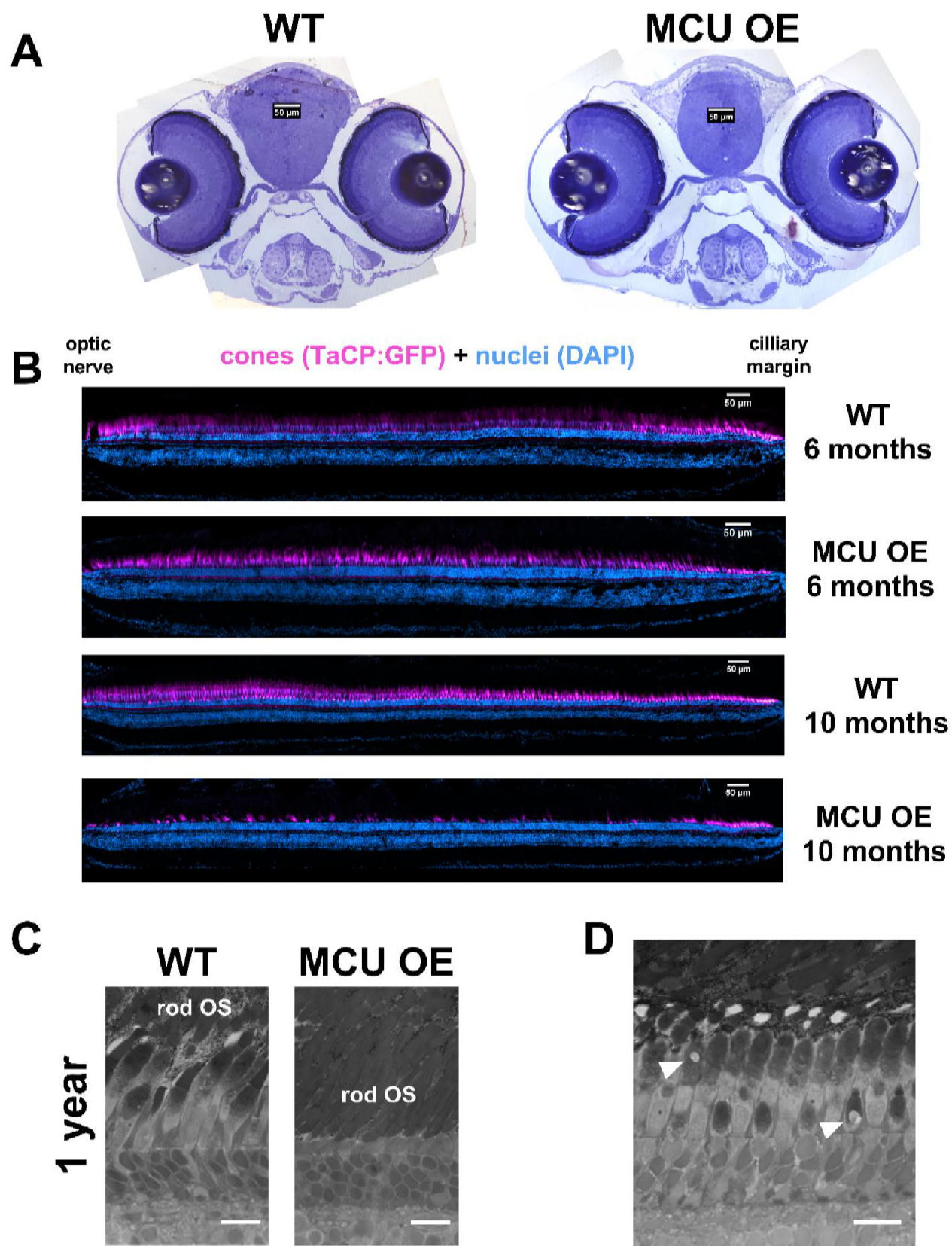
A. Electron micrograph from WT fish at 5 days of age. Structures similar to the electron lucent mitochondria in MCU OE fish can be sparsely observed in the ellipsoid WT cones (white arrowhead). These were markedly smaller than structures seen in MCU OE cones. Scale bar = 2 μ m.

B. Electron micrograph from WT fish at 5 days of age. What appear to be electron lucent, mislocalized mitochondria are sometimes observed in WT fish (white arrowhead). Scale bar = 2 μ m.

C. Quantification of mitochondrial clusters containing all electron dense mitochondria (healthy) and any electron lucent mitochondria either in the ellipsoid or mislocalized. Data compiled from a single slice at the optic nerve of larval zebrafish at 5 days of age. Clusters were counted and plotted relative to the distance (μ m) of the cluster from the optic nerve. Graphs shown are representative plots from dorsal and ventral sides of a single larvae, but this analysis was performed on n=3 larvae for each group for quantification in D.

D. Quantification of clusters containing lucent mitochondria as a percentage of total clusters observed (Healthy + Lucent (ellipsoid) + Lucent (mislocalized)) from data shown in C. N=3 larvae for WT and MCU OE. *p<0.05 and ns = not significant using Welch's t-test.

E. Electron micrograph of MCU OE fish at 3 months of age. The electron lucent mitochondrial phenotype is preserved as fish age and is not specific to early development. Scale bar = 10 μ m.



Legend on following page.

Supplemental Figure 8. Further characterization of retinal health throughout development in both WT and MCU OE models.

- A. Larval zebrafish sections at 6 days of age stained with Richardson's stain. Aside from mitochondrial disturbance in the photoreceptor layer of MCU OE retinas, normal morphology appears to be conserved. Scale bar = 50 μ m.
- B. Representative stitched and straightened images of T α CP:GFP (cones, magenta) retinal sections stained with a nuclear stain (Hoescht, cyan). The double cone nuclei that sit on top of the nuclear layer that contains both UV/blue cones and rods was used for quantification. Scale bar = 50 μ m.
- C. Richardson's stain of representative 1 year old zebrafish retina from WT and MCU OE fish. In MCU OE models, cones are rarely observed and instead rods have proliferated (rod OS = rod outer segments). Scale bar = 25 μ m.
- D. Richardson's stain of 1 year old zebrafish retina from WT fish. Occasionally, cone ellipsoid mitochondria clusters in these older fish are observed to have large, lucent mitochondria like younger MCU OE fish (white arrowheads). Scale bar = 25 μ m.

References

- Andersen, C.L., Jensen, J.L., and Ørntoft, T.F. (2004). Normalization of real-time quantitative reverse transcription-PCR data: a model-based variance estimation approach to identify genes suited for normalization, applied to bladder and colon cancer data sets. *Cancer Res.* 64, 5245–5250.
- Balaban, R.S. (2009). The role of Ca²⁺ signaling in the coordination of mitochondrial ATP production with cardiac work. *Biochim. Biophys. Acta - Bioenerg.* 1787, 1334–1341.
- Baradaran, R., Wang, C., Siliciano, A.F., and Long, S.B. (2018). Cryo-EM structures of fungal and metazoan mitochondrial calcium uniporters. *Nature* 559, 580–584.
- Barnes, S., and Kelly, M.E.M. (2002). Calcium channels at the photoreceptor synapse. *Adv. Exp. Med. Biol.* 514, 465–476.
- Barnhart, E.L. (2016). Mechanics of mitochondrial motility in neurons. *Curr. Opin. Cell Biol.* 38, 90–99.
- Baughman, J.M., Perocchi, F., Girgis, H.S., Plovanich, M., Belcher-Timme, C.A., Sancak, Y., Bao, X.R., Strittmatter, L., Goldberger, O., Bogorad, R.L., et al. (2011). Integrative genomics identifies MCU as an essential component of the mitochondrial calcium uniporter. *Nature* 476, 341–345.
- Baumgartner, H.K., Gerasimenko, J. V, Thorne, C., Ferdek, P., Pozzan, T., Tepikin, A. V, Petersen, O.H., Sutton, R., Watson, A.J.M., and Gerasimenko, O. V (2009). Calcium elevation in mitochondria is the main Ca²⁺ requirement for mitochondrial permeability transition pore (mPTP) opening. *J. Biol. Chem.* 284, 20796–20803.
- Bernardi, P., Scorrano, L., Colonna, R., Petronilli, V., and Lisa, F. Di (1999). Mitochondria and cell death. *Eur. J. Biochem.* 264, 687–701.
- Bowes, C., Li, T., Danciger, M., Baxter, L.C., Applebury, M.L., and Farber, D.B. (1990). Retinal degeneration in the rd mouse is caused by a defect in the β subunit of rod cGMP-phosphodiesterase. *Nature* 347, 677–680.
- Brockerhoff, S.E. (2017). Genome Editing to Study Ca²⁺ Homeostasis in Zebrafish Cone Photoreceptors. In *Advances in Experimental Medicine and Biology*, pp. 91–100.
- Chang, K.T., Niescier, R.F., and Min, K.-T. (2011). Mitochondrial matrix Ca²⁺ as an intrinsic signal regulating mitochondrial motility in axons. *Proc. Natl. Acad. Sci. U. S. A.* 108, 15456–15461.
- Chaudhuri, D., Artiga, D.J., Abiria, S.A., and Clapham, D.E. (2016). Mitochondrial calcium uniporter regulator 1 (MCUR1) regulates the calcium threshold for the mitochondrial permeability transition. *Proc. Natl. Acad. Sci. U. S. A.* 113, E1872–80.
- Chen, Y., and Sheng, Z.-H. (2013). Kinesin-1-syntrophin coupling mediates activity-dependent regulation of axonal mitochondrial transport. *J. Cell Biol.* 202, 351–364.

816 Chen, C.K., Burns, M.E., Spencer, M., Niemi, G.A., Chen, J., Hurley, J.B., Baylor, D.A., and Simon, M.I.
817 (1999a). Abnormal photoresponses and light-induced apoptosis in rods lacking rhodopsin kinase. *Proc.*
818 *Natl. Acad. Sci. U. S. A.* 96, 3718–3722.

819 Chen, J., Simon, M.I., Matthes, M.T., Yasumura, D., and LaVail, M.M. (1999b). Increased susceptibility to
820 light damage in an arrestin knockout mouse model of Oguchi disease (Stationary night blindness).
821 *Investig. Ophthalmol. Vis. Sci.* 40, 2978–2982.

822 Chen, M., Van Hook, M.J., and Thoreson, W.B. (2015). Ca^{2+} Diffusion through Endoplasmic Reticulum
823 Supports Elevated Intraterminal Ca^{2+} Levels Needed to Sustain Synaptic Release from Rods in Darkness.
824 *J. Neurosci.* 35, 11364–11373.

825 Chen, T.-W., Wardill, T.J., Sun, Y., Pulver, S.R., Renninger, S.L., Baohan, A., Schreiter, E.R., Kerr, R.A.,
826 Orger, M.B., Jayaraman, V., et al. (2013). Ultrasensitive fluorescent proteins for imaging neuronal activity.
827 *Nature* 499, 295–300.

828 Contreras, L., Gomez-Puertas, P., Iijima, M., Kobayashi, K., Saheki, T., and Satrústegui, J. (2007). Ca^{2+}
829 Activation kinetics of the two aspartate-glutamate mitochondrial carriers, aralar and citrin: role in the heart
830 malate-aspartate NADH shuttle. *J. Biol. Chem.* 282, 7098–7106.

831 Cooper, L.L., Hansen, R.M., Darras, B.T., Korson, M., Dougherty, F.E., Shoffner, J.M., and Fulton, A.B.
832 (2002). Rod Photoreceptor Function in Children With Mitochondrial Disorders. *Arch. Ophthalmol.* 120,
833 1055.

834 Csordás, G., Golenár, T., Seifert, E.L., Kamer, K.J., Sancak, Y., Perocchi, F., Moffat, C., Weaver, D.,
835 Perez, S. de la F., Bogorad, R., et al. (2013). MICU1 Controls Both the Threshold and Cooperative
836 Activation of the Mitochondrial Ca^{2+} Uniporter. *Cell Metab.* 17, 976–987.

837 Denton, R.M. (2009). Regulation of mitochondrial dehydrogenases by calcium ions. *Biochim. Biophys.*
838 *Acta - Bioenerg.* 1787, 1309–1316.

839 Denton, R.M., Randle, P.J., and Martin, B.R. (1972). Stimulation by calcium ions of pyruvate
840 dehydrogenase phosphate phosphatase. *Biochem. J.* 128, 161–163.

841 Dizhoor, A.M., Boikov, S.G., and Olshevskaya, E. V (1998). Constitutive activation of photoreceptor
842 guanylate cyclase by Y99C mutant of GCAP-1. Possible role in causing human autosomal dominant cone
843 degeneration. *J. Biol. Chem.* 273, 17311–17314.

844 Du, J., Cleghorn, W.M., Contreras, L., Lindsay, K., Rountree, A.M., Chertov, A.O., Turner, S.J.,
845 Sahaboglu, A., Linton, J., Sadilek, M., et al. (2013a). Inhibition of mitochondrial pyruvate transport by
846 zaprinast causes massive accumulation of aspartate at the expense of glutamate in the retina. *J. Biol.*
847 *Chem.* 288, 36129–36140.

848 Du, J., Cleghorn, W., Contreras, L., Linton, J.D., Chan, G.C.-K., Chertov, A.O., Saheki, T., Govindaraju,
849 V., Sadilek, M., Satrústegui, J., et al. (2013b). Cytosolic reducing power preserves glutamate in retina.
850 *Proc. Natl. Acad. Sci. U. S. A.* 110, 18501–18506.

851 Du, J., Linton, J.D., and Hurley, J.B. (2015). Chapter Four – Probing Metabolism in the Intact Retina
852 Using Stable Isotope Tracers. In *Methods in Enzymology*, pp. 149–170.

853 Du, J., Rountree, A., Cleghorn, W.M., Contreras, L., Lindsay, K.J., Sadilek, M., Gu, H., Djukovic, D.,
854 Raftery, D., Satrústegui, J., et al. (2016). Phototransduction Influences Metabolic Flux and Nucleotide
855 Metabolism in Mouse Retina. *J. Biol. Chem.* 291, 4698–4710.

856 Elustondo, P.A., Nichols, M., Negoda, A., Thirumaran, A., Zakharian, E., Robertson, G.S., and Pavlov, E.
857 V (2016). Mitochondrial permeability transition pore induction is linked to formation of the complex of
858 ATPase C-subunit, polyhydroxybutyrate and inorganic polyphosphate. *Cell Death Discov.* 2, 16070.

859 Fain, G.L. (2006). Why photoreceptors die (and why they don't). *BioEssays* 28, 344–354.

860 Fan, C., Fan, M., Orlando, B.J., Fastman, N.M., Zhang, J., Xu, Y., Chambers, M.G., Xu, X., Perry, K.,
861 Liao, M., et al. (2018). X-ray and cryo-EM structures of the mitochondrial calcium uniporter. *Nature* 559,
862 575–579.

863 Fieni, F., Bae Lee, S., Jan, Y.N., Kirichok, Y., Duchen, M.R., Carafoli, E., Carafoli, E., McCormack, J.G.,
864 Halestrap, A.P., Denton, R.M., et al. (2012). Activity of the mitochondrial calcium uniporter varies greatly
865 between tissues. *Nat. Commun.* 3, 1317.

866 Fox, D.A., Poblenz, A.T., and He, L. (1999). Calcium Overload Triggers Rod Photoreceptor Apoptotic Cell
867 Death in Chemical-Induced and Inherited Retinal Degenerations. *Ann. N. Y. Acad. Sci.* 893, 282–285.

868 Frank, S., Gaume, B., Bergmann-Leitner, E.S., Leitner, W.W., Robert, E.G., Catez, F., Smith, C.L., and
869 Youle, R.J. (2001). The Role of Dynamin-Related Protein 1, a Mediator of Mitochondrial Fission, in
870 Apoptosis. *Dev. Cell* 1, 515–525.

871 Giarmarco, M.M., Cleghorn, W.M., Sloat, S.R., Hurley, J.B., and Brockerhoff, S.E. (2017). Mitochondria
872 maintain distinct Ca^{2+} pools in cone photoreceptors. *J. Neurosci.* 37, 2689–16.

873 Giarmarco, M.M., Cleghorn, W.M., Hurley, J.B., and Brockerhoff, S.E. (2018). Preparing Fresh Retinal
874 Slices from Adult Zebrafish for Ex Vivo Imaging Experiments. *J. Vis. Exp.* e56977–e56977.

875 Glancy, B., and Balaban, R.S. (2012). Role of Mitochondrial Ca^{2+} in the Regulation of Cellular
876 Energetics. *Biochemistry* 51, 2959–2973.

877 Griffiths, E.J., and Rutter, G.A. (2009). Mitochondrial calcium as a key regulator of mitochondrial ATP
878 production in mammalian cells. *Biochim. Biophys. Acta - Bioenerg.* 1787, 1324–1333.

879 Hajnóczky, G., Robb-Gaspers, L.D., Seitz, M.B., and Thomas, A.P. (1995). Decoding of cytosolic calcium
880 oscillations in the mitochondria. *Cell* 82, 415–424.

881 He, L., Poblenz, A.T., Medrano, C.J., and Fox, D.A. (2000). Lead and calcium produce rod photoreceptor
882 cell apoptosis by opening the mitochondrial permeability transition pore. *J. Biol. Chem.* 275, 12175–
883 12184.

884 Hoang, Q.V., Linsenmeier, R.A., Chung, C.K., and Curcio, C.A. (2002). Photoreceptor inner segments in
885 monkey and human retina: Mitochondrial density, optics, and regional variation. *Vis. Neurosci.* 19, 395–
886 407.

887 Hoffman, N.E., Chandramoorthy, H.C., Shanmugapriya, S., Zhang, X.Q., Vallem, S., Doonan, P.J.,
888 Malliankaraman, K., Guo, S., Rajan, S., Elrod, J.W., et al. (2014). SLC25A23 augments mitochondrial
889 Ca^{2+} uptake, interacts with MCU, and induces oxidative stress-mediated cell death. *Mol. Biol. Cell* 25,
890 936–947.

891 Hunter, J.J.F.E., Malison, R., Bridgers, W.F., Schutz, B., and Atchisox, A. (1959). Reincorporation of
892 Diphosphopyridine Nucleotide into Mitochondrial Enzyme Systems. *J. Biol. Chem.* 234, 693–700.

893 Jouaville, L.S., Pinton, P., Bastianutto, C., Rutter, G.A., and Rizzuto, R. (1999). Regulation of
894 mitochondrial ATP synthesis by calcium: evidence for a long-term metabolic priming. *Proc. Natl. Acad.*
895 *Sci. U. S. A.* 96, 13807–13812.

896 Kamer, K.J., Mootha, V.K., Deluca, H., Engstrom, G., Vasington, F., Murphy, J., Kirichok, Y., Krapivinsky,
897 G., Clapham, D., Gunter, T., et al. (2014). MICU1 and MICU2 play nonredundant roles in the regulation of
898 the mitochondrial calcium uniporter. *EMBO Rep.* 15, 299–307.

899 Kanow, M.A., Giarmarco, M.M., Jankowski, C.S., Tsantilas, K., Engel, A.L., Du, J., Linton, J.D.,
900 Farnsworth, C.C., Sloat, S.R., Rountree, A., et al. (2017). Biochemical adaptations of the retina and
901 retinal pigment epithelium support a metabolic ecosystem in the vertebrate eye. *Elife* 6.

902 Kennedy, B.N., Alvarez, Y., Brockerhoff, S.E., Stearns, G.W., Sapetto-Rebow, B., Taylor, M.R., and
903 Hurley, J.B. (2007). Identification of a Zebrafish Cone Photoreceptor-Specific Promoter and Genetic
904 Rescue of Achromatopsia in the *nof* Mutant. *Investig. Ophthalmology Vis. Sci.* 48, 522.

905 Kim, J.H., Lee, S.-R., Li, L.-H., Park, H.-J., Park, J.-H., Lee, K.Y., Kim, M.-K., Shin, B.A., and Choi, S.-Y.
906 (2011). High Cleavage Efficiency of a 2A Peptide Derived from Porcine Teschovirus-1 in Human Cell
907 Lines, Zebrafish and Mice. *PLoS One* 6, e18556.

908 Kiyama, T., Chen, C., Wang, S.W., Pan, P., Ju, Z., Wang, J., Takada, S., Klein, W.H., and Mao, C.
909 (2018). Essential roles of mitochondrial biogenesis regulator Nrf1 in retinal development and
910 homeostasis. 1–23.

- 911 Kremers, G.-J., Goedhart, J., van den Heuvel, D.J., Gerritsen, H.C., and Gadella, T.W.J. (2007).
912 Improved Green and Blue Fluorescent Proteins for Expression in Bacteria and Mammalian Cells.
913 *Biochemistry* 46, 3775–3783.
- 914 Krizaj, D., and Copenhagen, D.R. (1998). Compartmentalization of Calcium Extrusion Mechanisms in the
915 Outer and Inner Segments of Photoreceptors. *Neuron* 21, 249–256.
- 916 Križaj, D. (2012). Calcium stores in vertebrate photoreceptors. *Adv. Exp. Med. Biol.* 740, 873–889.
- 917 Kroemer, G., Zamzami, N., and Susin, S.A. (1997). Mitochondrial control of apoptosis. *Immunol. Today*
918 18, 44–51.
- 919 LaVail, M.M., Gorin, G.M., Repaci, M.A., Thomas, L.A., and Ginsberg, H.M. (1987). Genetic regulation of
920 light damage to photoreceptors. *Invest. Ophthalmol. Vis. Sci.* 28, 1043–1048.
- 921 Lee, Y.-J., Jeong, S.-Y., Karbowski, M., Smith, C.L., and Youle, R.J. (2004). Roles of the Mammalian
922 Mitochondrial Fission and Fusion Mediators Fis1, Drp1, and Opa1 in Apoptosis. *Mol. Biol. Cell* 15, 5001–
923 5011.
- 924 Li, C., Wen, A., Shen, B., Lu, J., Huang, Y., and Chang, Y. (2011). FastCloning: a highly simplified,
925 purification-free, sequence- and ligation-independent PCR cloning method. *BMC Biotechnol.* 11, 92.
- 926 Ma, E.Y., Lewis, a, Barabas, P., Stearns, G., Suzuki, S., Krizaj, D., and Brockerhoff, S.E. (2013). Loss of
927 Pde6 reduces cell body Ca²⁺ transients within photoreceptors. *Cell Death Dis.* 4, e797.
- 928 Madesh, M., Mallilankaraman, K., Doonan, P., Cardenas, C., Chandramoorthy, H.C., Muller, M., Miller,
929 R., Hoffman, N., Gandhirajan, R., Birnbaum, M., et al. (2013). MICU1 is an Essential Gatekeeper for
930 MCU-Mediated Mitochondrial Ca²⁺ Uptake that Regulates Cell Survival. *Biophys. J.* 104, 301a.
- 931 Makino, C.L., Dodd, R.L., Chen, J., Burns, M.E., Roca, A., Simon, M.I., and Baylor, D.A. (2004).
932 Recoverin Regulates Light-dependent Phosphodiesterase Activity in Retinal Rods. *J. Gen. Physiol.* 123,
933 729–741.
- 934 Mammucari, C., Gherardi, G., Zamparo, I., Raffaello, A., Boncompagni, S., Sandri, M., Stefani, D. De,
935 Protasi, F., Lanfranchi, G., and Rizzuto, R. (2015). The Mitochondrial Calcium Uniporter Controls Skeletal
936 Muscle Trophism In Vivo Report The Mitochondrial Calcium Uniporter Controls Skeletal Muscle Trophism
937 In Vivo. *CellReports* 10, 1269–1279.
- 938 Mammucari, C., Raffaello, A., Vecellio Reane, D., Gherardi, G., De Mario, A., and Rizzuto, R. (2018).
939 Mitochondrial calcium uptake in organ physiology: from molecular mechanism to animal models. *Pflügers*
940 *Arch. - Eur. J. Physiol.* 1165–1179.
- 941 McCormack, J.G., and Denton, R.M. (1979). The effects of calcium ions and adenine nucleotides on the
942 activity of pig heart 2-oxoglutarate dehydrogenase complex. *Biochem. J.* 180.
- 943 McCormack, J.G., Halestrap, A.P., and Denton, R.M. (1990). Role of calcium ions in regulation of
944 mammalian intramitochondrial metabolism. *Physiol. Rev.* 70, 391–425.
- 945 McCurley, A.T., Callard, G. V, Eisen, J., Huggett, J., Dheda, K., Bustin, S., Zumla, A., Bustin, S., Bustin,
946 S., Dheda, K., et al. (2008). Characterization of housekeeping genes in zebrafish: male-female
947 differences and effects of tissue type, developmental stage and chemical treatment. *BMC Mol. Biol.* 9,
948 102.
- 949 McWilliams, T.G., Prescott, A.R., Allen, G.F.G., Tamjar, J., Munson, M.J., Thomson, C., Muqit, M.M.K.,
950 and Ganley, I.G. (2016). mito-QC illuminates mitophagy and mitochondrial architecture in vivo. *J. Cell*
951 *Biol.* 214, 333–345.
- 952 Mendez, A., Burns, M.E., Sokal, I., Dizhoor, A.M., Baehr, W., Palczewski, K., Baylor, D.A., and Chen, J.
953 (2001). Role of guanylate cyclase-activating proteins (GCAPs) in setting the flash sensitivity of rod
954 photoreceptors. *Proc. Natl. Acad. Sci.* 98, 9948–9953.
- 955 Nag, T.C., and Wadhwa, S. (2016). Immunolocalisation pattern of complex IV in ageing human retina:
956 Correlation with mitochondrial ultrastructure. *Mitochondrion* 31, 20–32.
- 957 Nakatani, K., and Yau, K.W. (1988). Calcium and light adaptation in retinal rods and cones. *Nature* 334,
958 69–71.

959 Nguyen, N.X., Armache, J.-P., Lee, C., Yang, Y., Zeng, W., Mootha, V.K., Cheng, Y., Bai, X., and Jiang,
960 Y. (2018). Cryo-EM structure of a fungal mitochondrial calcium uniporter. *Nature* 559, 570–574.

961 Nieminen, A.-L., Schwartz, J., Hung, H.-I., Blocker, E.R., Gooz, M., and Lemasters, J.J. (2014). Mitoferrin-
962 2 (MFRN2) Regulates the Electrogenic Mitochondrial Calcium Uniporter and Interacts Physically with
963 MCU. *Biophys. J.* 106, 581a–582a.

964 Niescier, R.F., Chang, K.T., and Min, K.-T. (2013). Miro, MCU, and calcium: bridging our understanding of
965 mitochondrial movement in axons. *Front. Cell. Neurosci.* 7, 148.

966 Niescier, R.F., Hong, K., Park, D., and Min, K.-T. (2018). MCU Interacts with Miro1 to Modulate
967 Mitochondrial Functions in Neurons. *J. Neurosci.* 38, 4666–4677.

968 Okawa, H., Sampath, A.P., Laughlin, S.B., and Fain, G.L. (2008). ATP Consumption by Mammalian Rod
969 Photoreceptors in Darkness and in Light. *Curr. Biol.* 18, 1917–1921.

970 Oxenoid, K., Dong, Y., Cao, C., Cui, T., Sancak, Y., Markhard, A.L., Grabarek, Z., Kong, L., Liu, Z.,
971 Ouyang, B., et al. (2016). Architecture of the mitochondrial calcium uniporter. *Nature* 533, 1–17.

972 Paillard, M., Csordás, G., Szanda, G., Golenár, T., Debattisti, V., Bartok, A., Wang, N., Moffat, C., Seifert,
973 E.L., Spät, A., et al. (2017). Tissue-Specific Mitochondrial Decoding of Cytoplasmic Ca^{2+} Signals Is
974 Controlled by the Stoichiometry of MICU1/2 and MCU. *Cell Rep.* 18, 2291–2300.

975 Paillard, M., Csordás, G., Huang, K.-T., Várnai, P., Joseph, S.K., and Hajnóczky, G. (2018). MICU1
976 Interacts with the D-Ring of the MCU Pore to Control Its Ca^{2+} Flux and Sensitivity to Ru360. *Mol. Cell.* 72,
977 1–8.

978 Patron, M., Checchetto, V., Raffaello, A., Teardo, E., Vecellio Reane, D., Mantoan, M., Granatiero, V.,
979 Szabò, I., De Stefani, D., and Rizzuto, R. (2014). MICU1 and MICU2 Finely Tune the Mitochondrial Ca^{2+}
980 Uniporter by Exerting Opposite Effects on MCU Activity. *Mol. Cell* 53, 726–737.

981 Patron, M., Granatiero, V., Espino, J., Rizzuto, R., and De Stefani, D. (2018). MICU3 is a tissue-specific
982 enhancer of mitochondrial calcium uptake. *Cell Death Differ.* 1.

983 Paupe, V., Prudent, J., Dassa, E.P., Rendon, O.Z., and Shoubridge, E.A. (2015). CCDC90A (MCUR1) Is
984 a Cytochrome c Oxidase Assembly Factor and Not a Regulator of the Mitochondrial Calcium Uniporter.
985 *Cell Metabolism* 21, 109–116.

986 Payne, A.M., Downes, S.M., Bessant, D.A., Taylor, R., Holder, G.E., Warren, M.J., Bird, A.C., and
987 Bhattacharya, S.S. (1998). A mutation in guanylate cyclase activator 1A (GUCA1A) in an autosomal
988 dominant cone dystrophy pedigree mapping to a new locus on chromosome 6p21.1. *Hum. Mol. Genet.* 7,
989 273–277.

990 Plovanich, M., Bogorad, R.L., Sancak, Y., Kamer, K.J., Strittmatter, L., Li, A.A., Girgis, H.S., Kuchimanchi,
991 S., De Groot, J., Speciner, L., et al. (2013). MICU2, a Paralog of MICU1, Resides within the Mitochondrial
992 Uniporter Complex to Regulate Calcium Handling. *PLoS One* 8, e55785.

993 Preibisch, S., Saalfeld, S., and Tomancak, P. (2009). Globally optimal stitching of tiled 3D microscopic
994 image acquisitions. *Bioinformatics* 25, 1463–1465.

995 Raffaello, A., De Stefani, D., Sabbadin, D., Teardo, E., Merli, G., Picard, A., Checchetto, V., Moro, S.,
996 Szabò, I., and Rizzuto, R. (2013). The mitochondrial calcium uniporter is a multimer that can include a
997 dominant-negative pore-forming subunit. *EMBO J.* 32, 2362–2376.

998 Richardson, K.C., Jarett, L., and Finke, E.H. (1960). Embedding in Epoxy Resins for Ultrathin Sectioning
999 in Electron Microscopy. *Stain Technol.* 35, 313–323.

1000 Rizzuto, R., De Stefani, D., Raffaello, A., and Mammucari, C. (2012). Mitochondria as sensors and
1001 regulators of calcium signalling. *Nat. Rev. Mol. Cell Biol.* 13, 566–578.

1002 Sakurai, K., Chen, J., and Kefalov, V.J. (2011). Role of guanylyl cyclase modulation in mouse cone
1003 phototransduction. *J. Neurosci.* 31, 7991–8000.

1004 Sakurai, K., Chen, J., Khani, S.C., and Kefalov, V.J. (2015). Regulation of Mammalian Cone
1005 Phototransduction by Recoverin and Rhodopsin Kinase. *J. Biol. Chem.* 290, 9239–9250.

1006 Sampath, A.P., Matthews, H.R., Cornwall, M.C., and Fain, G.L. (1998). Bleached pigment produces a
1007 maintained decrease in outer segment Ca^{2+} in salamander rods. *J. Gen. Physiol.* **111**, 53–64.

1008 Sampath, A.P., Matthews, H.R., Cornwall, M.C., Bandarchi, J., and Fain, G.L. (1999). Light-dependent
1009 Changes in Outer Segment Free- Ca^{2+} Concentration in Salamander Cone Photoreceptors. *J. Gen.*
1010 *Physiol.* **113**, 267–277.

1011 Sancak, Y., Markhard, A.L., Kitami, T., Kovács-Bogdán, E., Kamer, K.J., Udeshi, N.D., Carr, S.A.,
1012 Chaudhuri, D., Clapham, D.E., Li, A.A., et al. (2013). EMRE is an essential component of the
1013 mitochondrial calcium uniporter complex. *Science* **342**, 1379–1382.

1014 Satrustegui, J., Pardo, B., and del Arco, A. (2007). Mitochondrial Transporters as Novel Targets for
1015 Intracellular Calcium Signaling. *Physiol. Rev.* **87**, 29–67.

1016 Schmitt, E.A., and Dowling, J.E. (1999). Early retinal development in the zebrafish, *Danio rerio*: Light and
1017 electron microscopic analyses. *J. Comp. Neurol.* **404**, 515–536.

1018 Smaili, S.S., Hsu, Y.-T., Youle, R.J., and Russell, J.T. (2000). Mitochondria in Ca^{2+} Signaling and
1019 Apoptosis. *J. Bioenerg. Biomembr.* **32**, 35–46.

1020 Sokal, I., Li, N., Surgucheva, I., Warren, M.J., Payne, A.M., Bhattacharya, S.S., Baehr, W., and
1021 Palczewski, K. (1998). GCAP1(Y99C) Mutant Is Constitutively Active in Autosomal Dominant Cone
1022 Dystrophy. *Mol. Cell* **2**, 129–133.

1023 Stearns, G., Evangelista, M., Fadool, J.M., and Brockerhoff, S.E. (2007). A Mutation in the Cone-Specific
1024 *pde6* Gene Causes Rapid Cone Photoreceptor Degeneration in Zebrafish. *J. Neurosci.* **27**, 13866–13874.

1025 De Stefani, D., Raffaello, A., Teardo, E., Szabò, I., and Rizzuto, R. (2011). A forty-kilodalton protein of the
1026 inner membrane is the mitochondrial calcium uniporter. *Nature* **476**, 336–340.

1027 De Stefani, D., Patron, M., and Rizzuto, R. (2015). Structure and function of the mitochondrial calcium
1028 uniporter complex. *Biochim. Biophys. Acta - Mol. Cell Res.* **1853**, 2006–2011.

1029 Strzelecki, T., Strzelecka, D., Koch, C.D., and LaNoue, K.F. (1988). Sites of action of glucagon and other
1030 Ca^{2+} mobilizing hormones on the malate aspartate cycle. *Arch. Biochem. Biophys.* **264**, 310–320.

1031 Suarez, J., Cividini, F., Scott, B.T., Lehmann, K., Diaz-Juarez, J., Diemer, T., Dai, A., Suarez, J.A., Jain,
1032 M., and Dillmann, W.H. (2018). Restoring mitochondrial calcium uniporter expression in diabetic mouse
1033 heart improves mitochondrial calcium handling and cardiac function. *J. Biol. Chem.* **293**, 8182–8195.

1034 Szikra, T., and Krizaj, D. (2007). Intracellular organelles and calcium homeostasis in rods and cones. *Vis.*
1035 *Neurosci.* **24**, 733–743.

1036 Tang, R., Dodd, A., Lai, D., McNabb, W.C., and Love, D.R. (2007). Validation of zebrafish (*Danio rerio*)
1037 reference genes for quantitative real-time RT-PCR normalization. *Acta Biochim. Biophys. Sin. (Shanghai).*
1038 **39**, 384–390.

1039 Tarboush, R., Chapman, G.B., and Connaughton, V.P. (2012). Ultrastructure of the distal retina of the
1040 adult zebrafish, *Danio rerio*. *Tissue Cell* **44**, 264–279.

1041 Tomar, D., Dong, Z., Shanmughapriya, S., Koch, D.A., Thomas, T., Hoffman, N.E., Timbalia, S.A.,
1042 Goldman, S.J., Breves, S.L., Corbally, D.P., et al. (2016). MCUR1 Is a Scaffold Factor for the MCU
1043 Complex Function and Promotes Mitochondrial Bioenergetics. *Cell Rep.* **0**, 833–844.

1044 Tsai, C.-W., Wu, Y., Pao, P.-C., Phillips, C.B., Williams, C., Miller, C., Ranaghan, M., and Tsai, M.-F.
1045 (2017). Proteolytic control of the mitochondrial calcium uniporter complex. *Proc. Natl. Acad. Sci. U. S. A.*
1046 **114**, 4388–4393.

1047 Tucker, C.L., Woodcock, S.C., Kelsell, R.E., Ramamurthy, V., Hunt, D.M., and Hurley, J.B. (1999).
1048 Biochemical analysis of a dimerization domain mutation in RetGC-1 associated with dominant cone-rod
1049 dystrophy. *Proc. Natl. Acad. Sci. U. S. A.* **96**, 9039–9044.

1050 Vandesompele, J., De Preter, K., Pattyn, F., Poppe, B., Van Roy, N., De Paepe, A., and Speleman, F.
1051 (2002). Accurate normalization of real-time quantitative RT-PCR data by geometric averaging of multiple
1052 internal control genes. *Genome Biol.* **3**.

1053 Villefranc, J.A., Amigo, J., and Lawson, N.D. (2007). Gateway compatible vectors for analysis of gene
1054 function in the zebrafish. *Dev. Dyn.* 236, 3077–3087.

1055 Vinberg, F., Kolesnikov, A. V., and Kefalov, V.J. (2014). Ex vivo ERG analysis of photoreceptors using an
1056 in vivo ERG system. *Vision Res.* 101, 108–117.

1057 Vinberg, F., Wang, T., Molday, R.S., Chen, J., and Kefalov, V.J. (2015a). A new mouse model for
1058 stationary night blindness with mutant Slc24a1 explains the pathophysiology of the associated human
1059 disease. *Hum. Mol. Genet.* 24, 5915–5929.

1060 Vinberg, F., and Kefalov, V. (2015b). Simultaneous ex vivo Functional Testing of Two Retinas by in vivo
1061 Electroretinogram System. *J. Vis. Exp.*

1062 Vinberg, F., Wang, T., De Maria, A., Zhao, H., Bassnett, S., Chen, J., and Kefalov, V.J. (2017). The
1063 Na⁺/Ca²⁺, K⁺ exchanger NCKX4 is required for efficient cone-mediated vision. *Elife* 6.

1064 Vinberg, F., Chen, J., and Kefalov, V.J. (2018). Regulation of calcium homeostasis in the outer segments
1065 of rod and cone photoreceptors. *Prog. Retin. Eye Res.* 67, 87–101.

1066 Wan, B., LaNoue, K.F., Cheung, J.Y., and Scaduto, R.C. (1989). Regulation of citric acid cycle by
1067 calcium. *J. Biol. Chem.* 264, 13430–13439.

1068 Wang, X., and Schwarz, T.L. (2009). The Mechanism of Ca²⁺-Dependent Regulation of Kinesin-Mediated
1069 Mitochondrial Motility. *Cell* 136, 163–174.

1070 Wilkie, S.E., Newbold, R.J., Deery, E., Walker, C.E., Stinton, I., Ramamurthy, V., Hurley, J.B.,
1071 Bhattacharya, S.S., Warren, M.J., and Hunt, D.M. (2000). Functional characterization of missense
1072 mutations at codon 838 in retinal guanylate cyclase correlates with disease severity in patients with
1073 autosomal dominant cone-rod dystrophy. *Hum. Mol. Genet.* 9, 3065–3073.

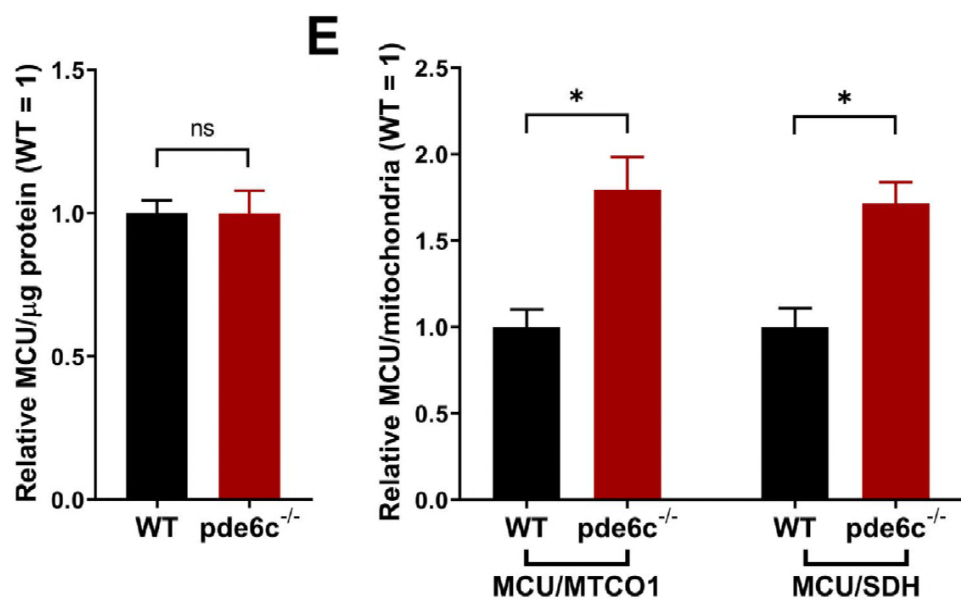
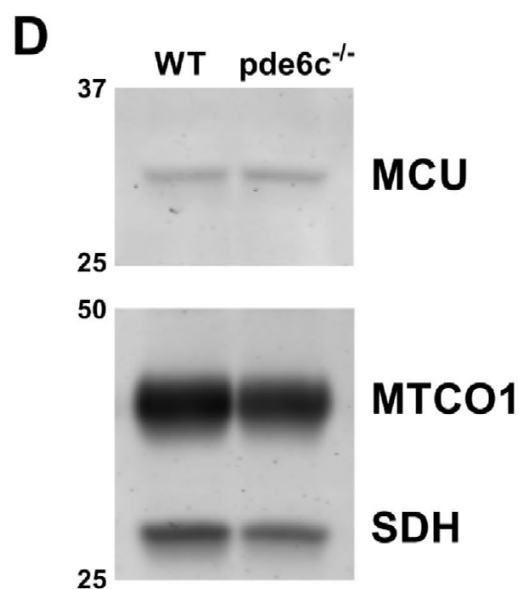
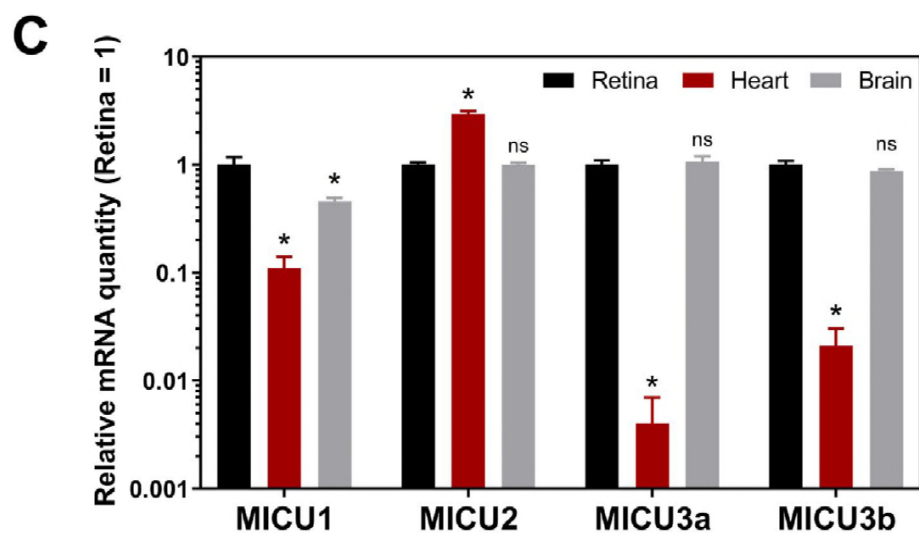
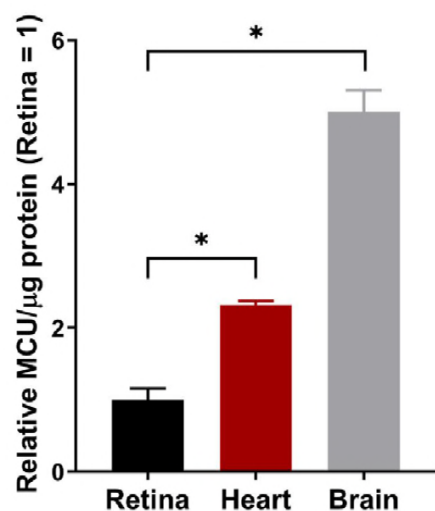
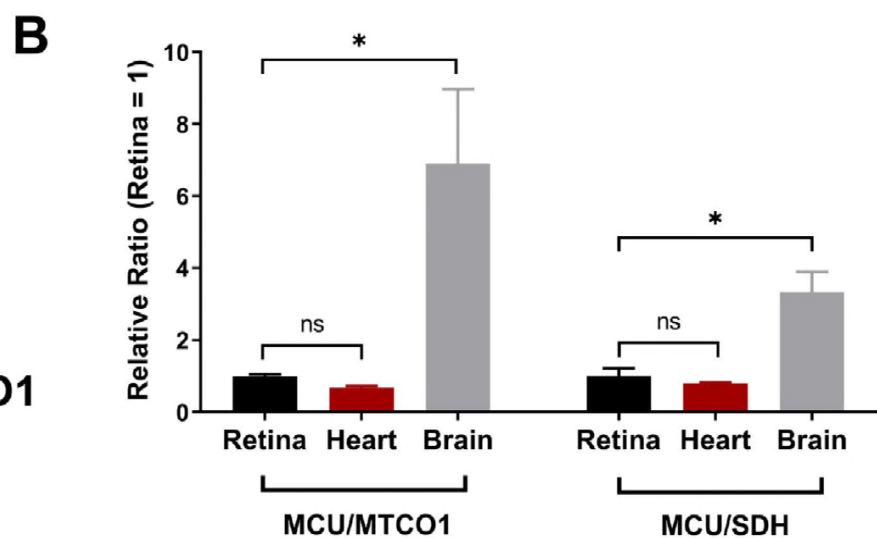
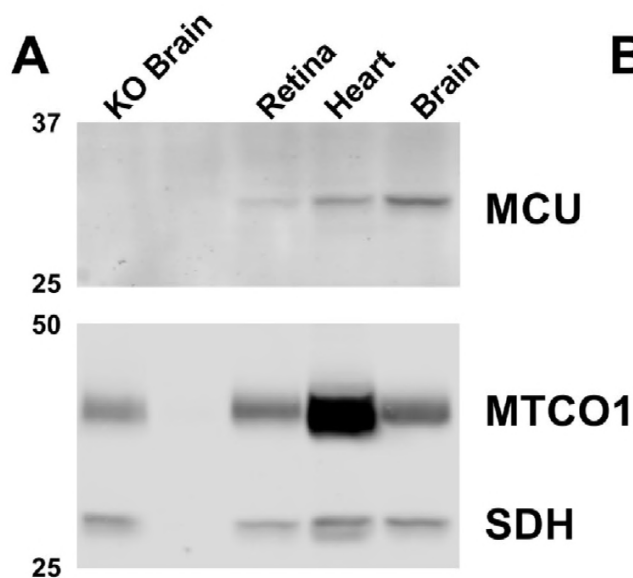
1074 Yoo, J., Wu, M., Yin, Y., Herzik, M.A., Lander, G.C., and Lee, S.-Y. (2018). Cryo-EM structure of a
1075 mitochondrial calcium uniporter. *Science* 361, 506–511.

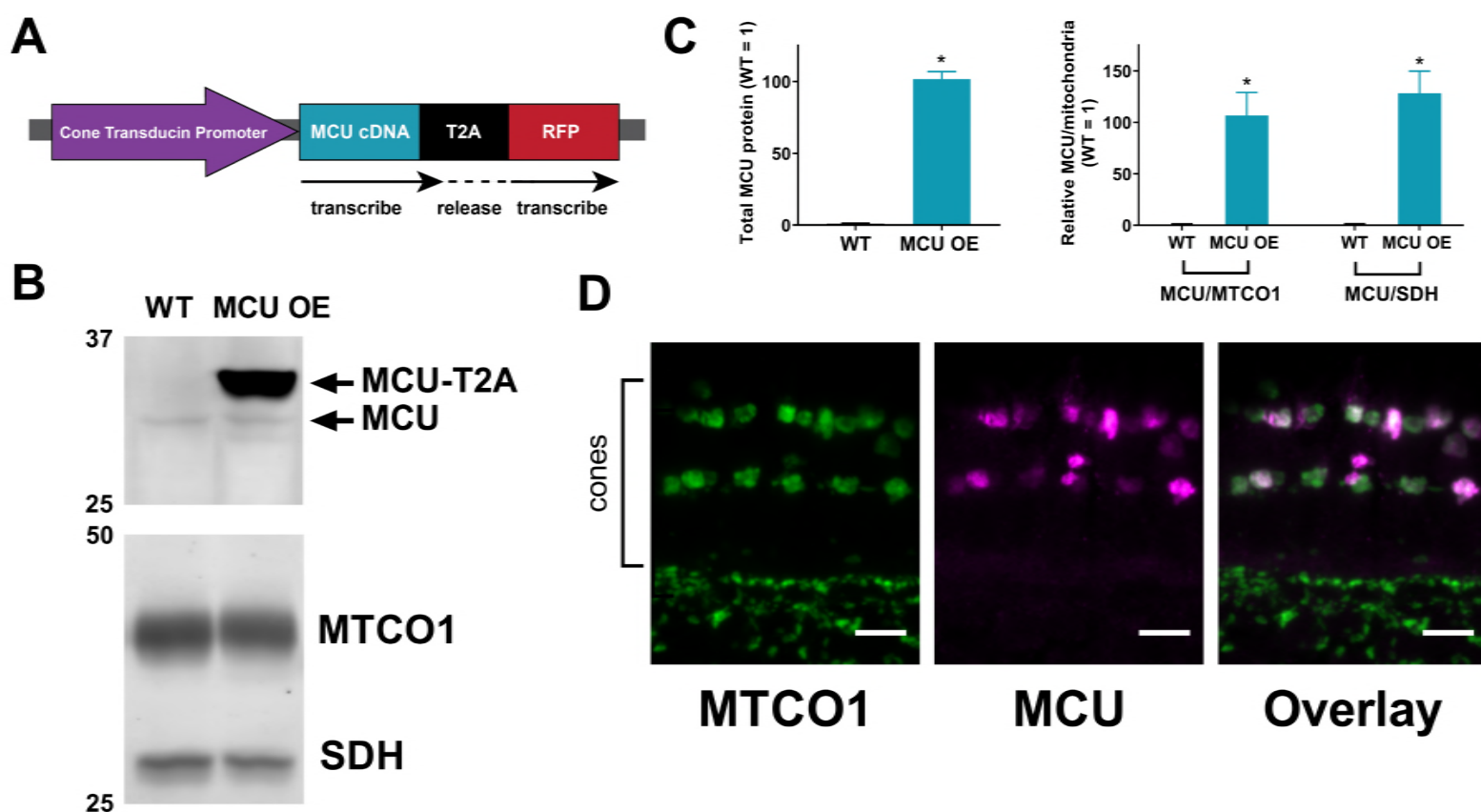
1076 Youle, R.J., and Karbowski, M. (2005). Mitochondrial fission in apoptosis. *Nat. Rev. Mol. Cell Biol.* 6, 657–
1077 663.

1078 Zeng, F., Chen, X., Cui, W., Wen, W., Lu, F., Sun, X., Ma, D., Yuan, Y., Li, Z., Hou, N., et al. (2018b).
1079 RIPK1 Binds MCU to Mediate Induction of Mitochondrial Ca²⁺ Uptake and Promotes Colorectal
1080 Oncogenesis. *Cancer Res.* 78, 2876–2885.

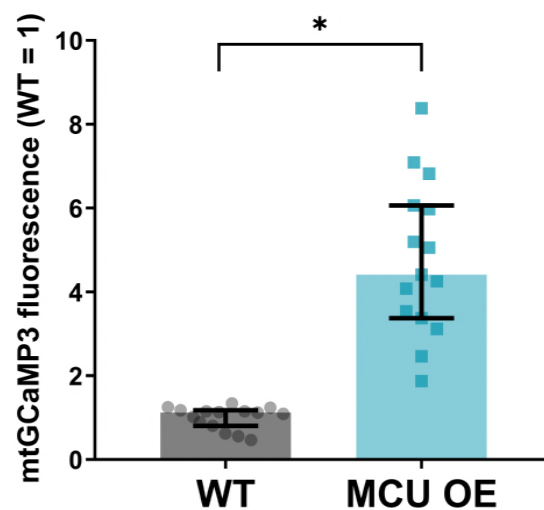
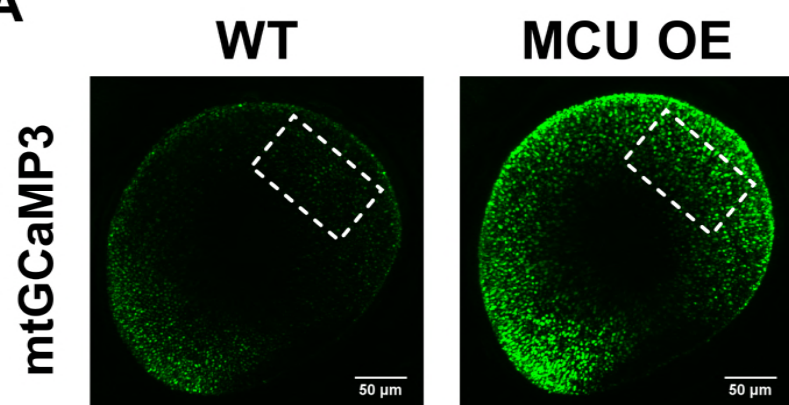
1081 Zoratti, M., and Szabò, I. (1995). The mitochondrial permeability transition. *Biochim. Biophys. Acta - Rev.*
1082 *Biomembr.* 1241, 139–176.

1083

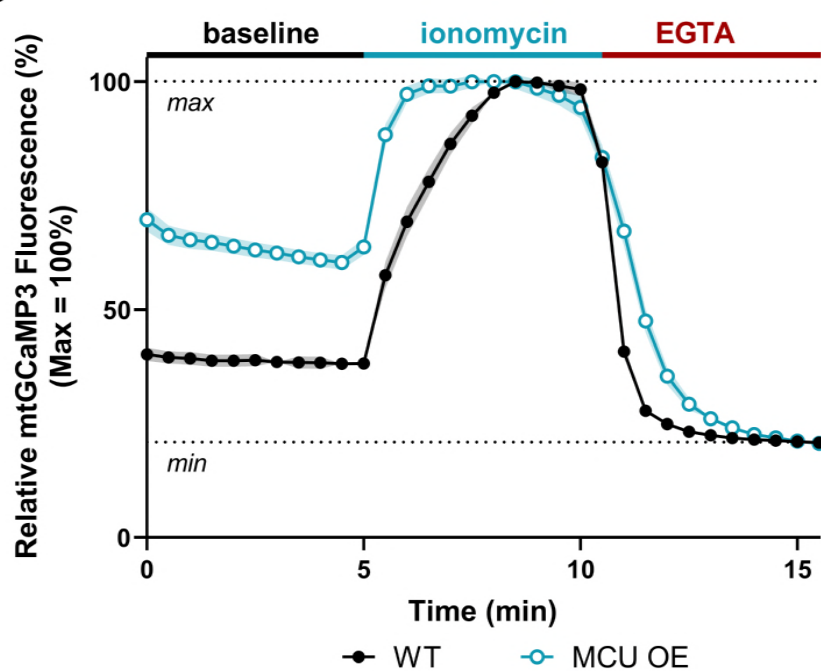




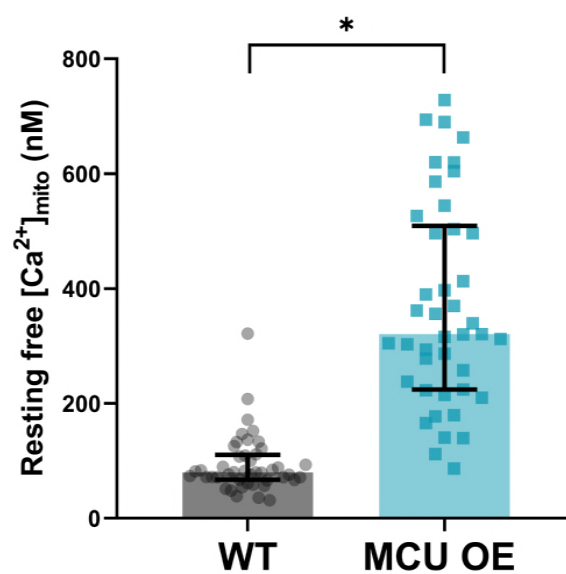
A

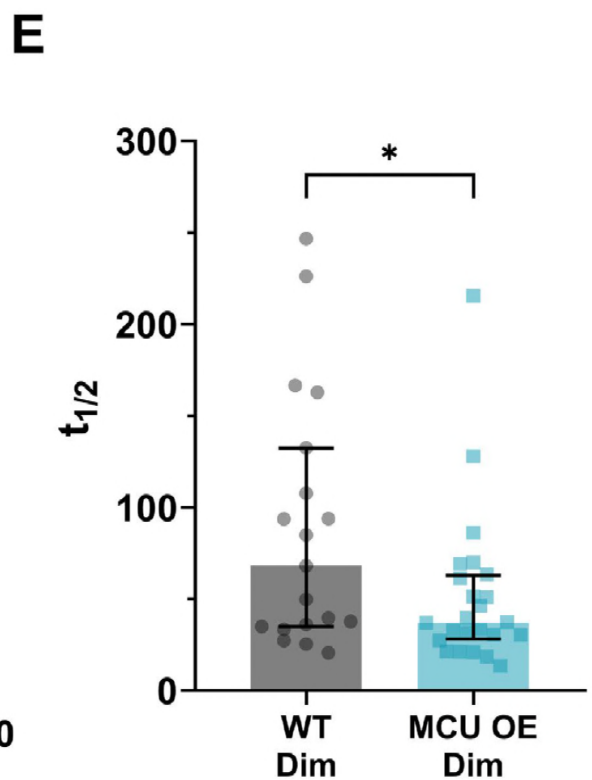
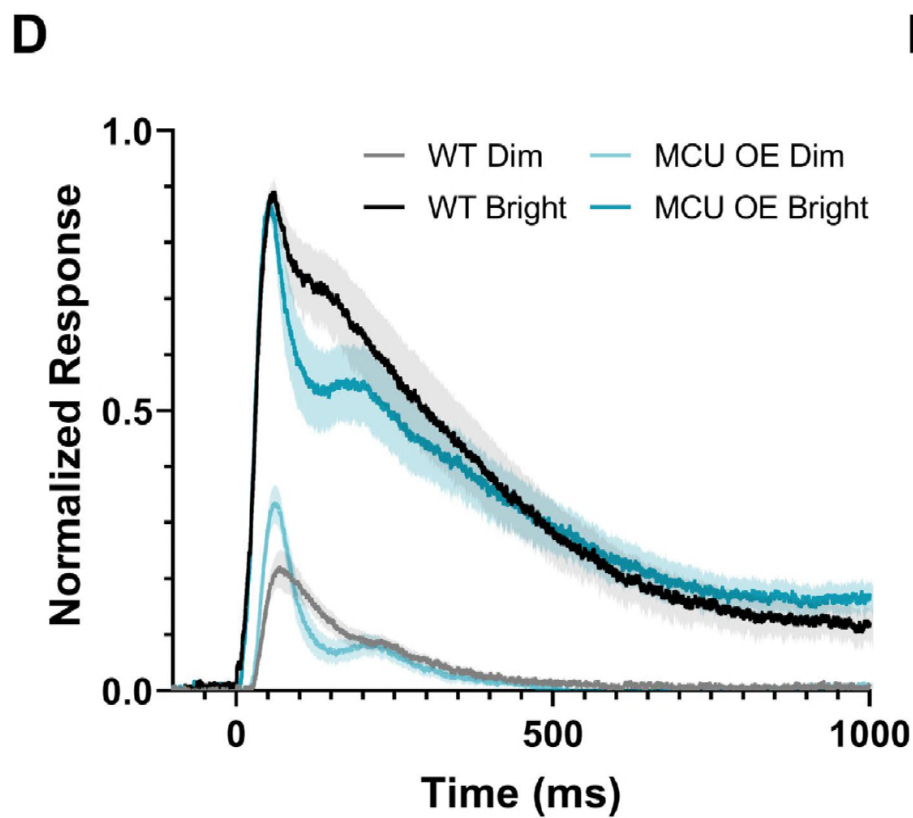
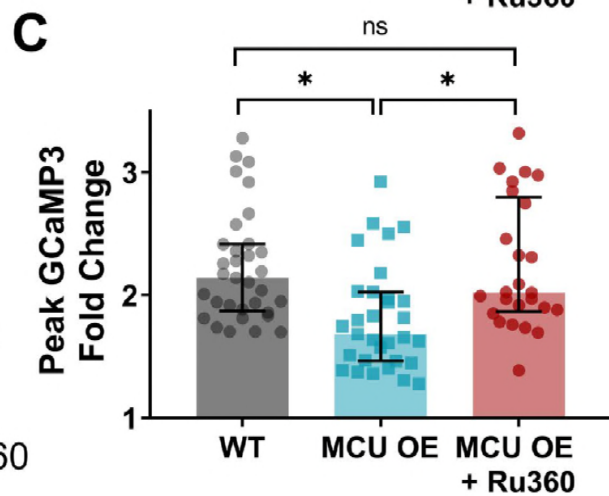
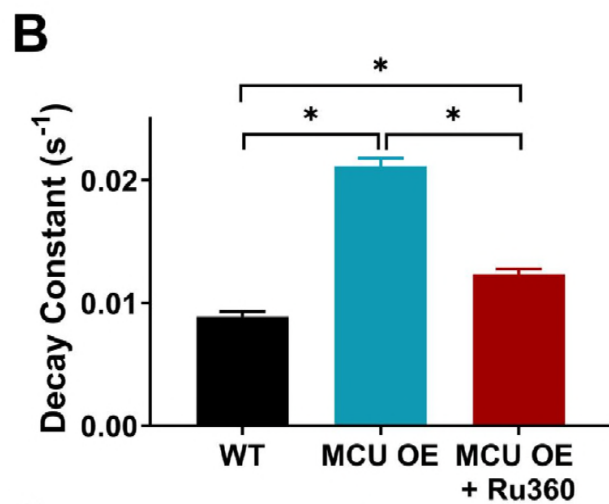
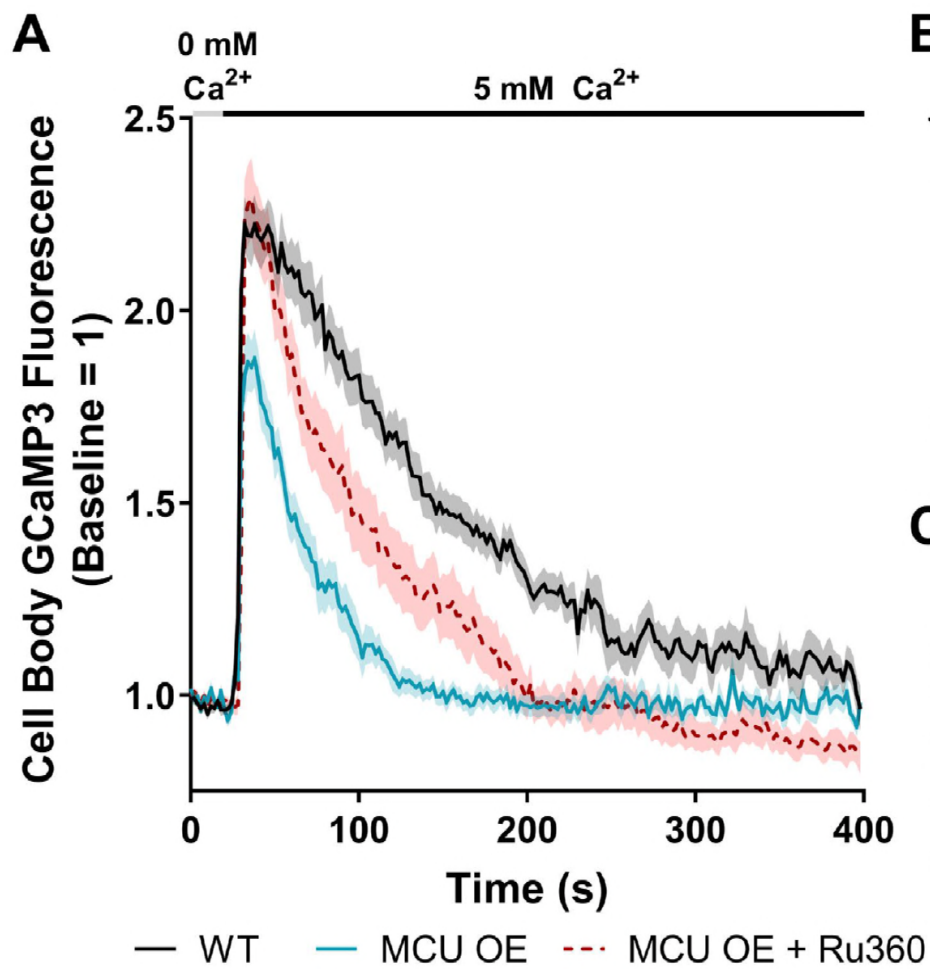


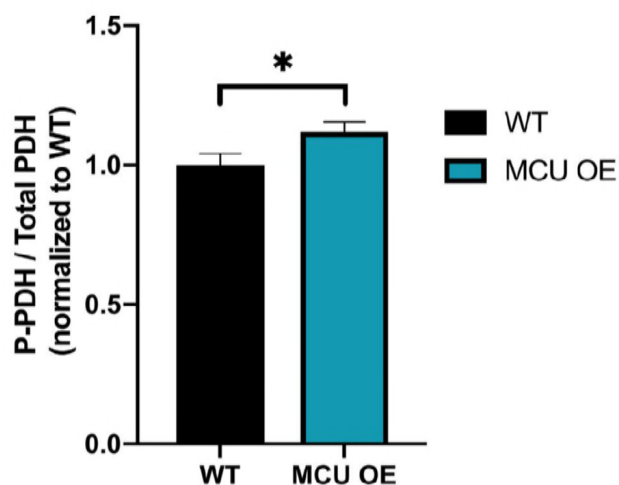
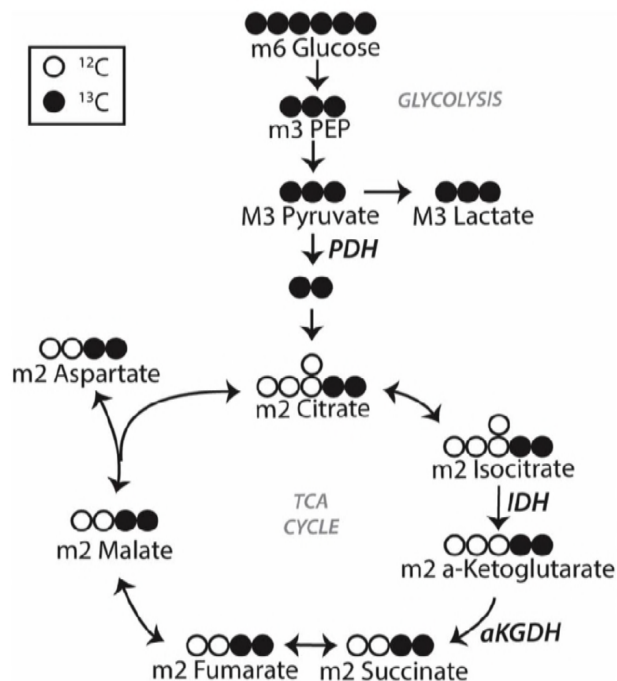
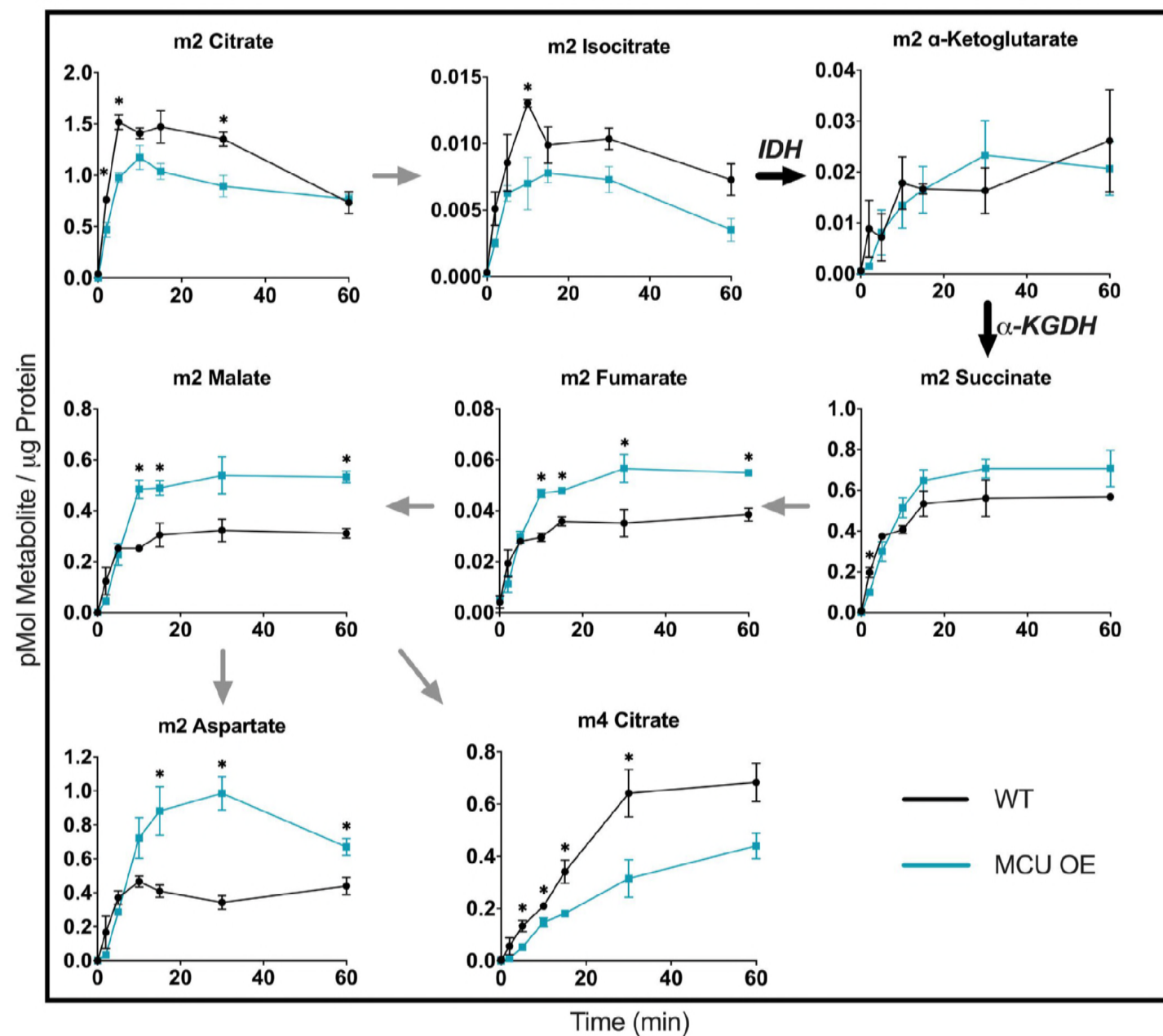
B



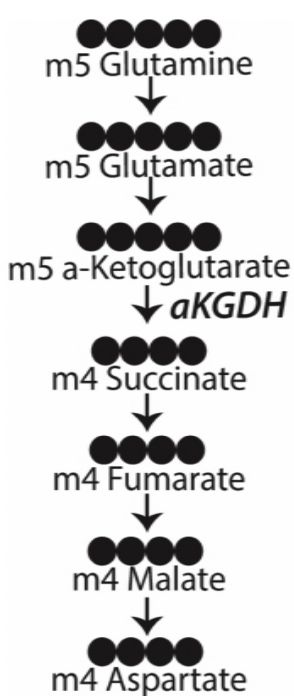
C



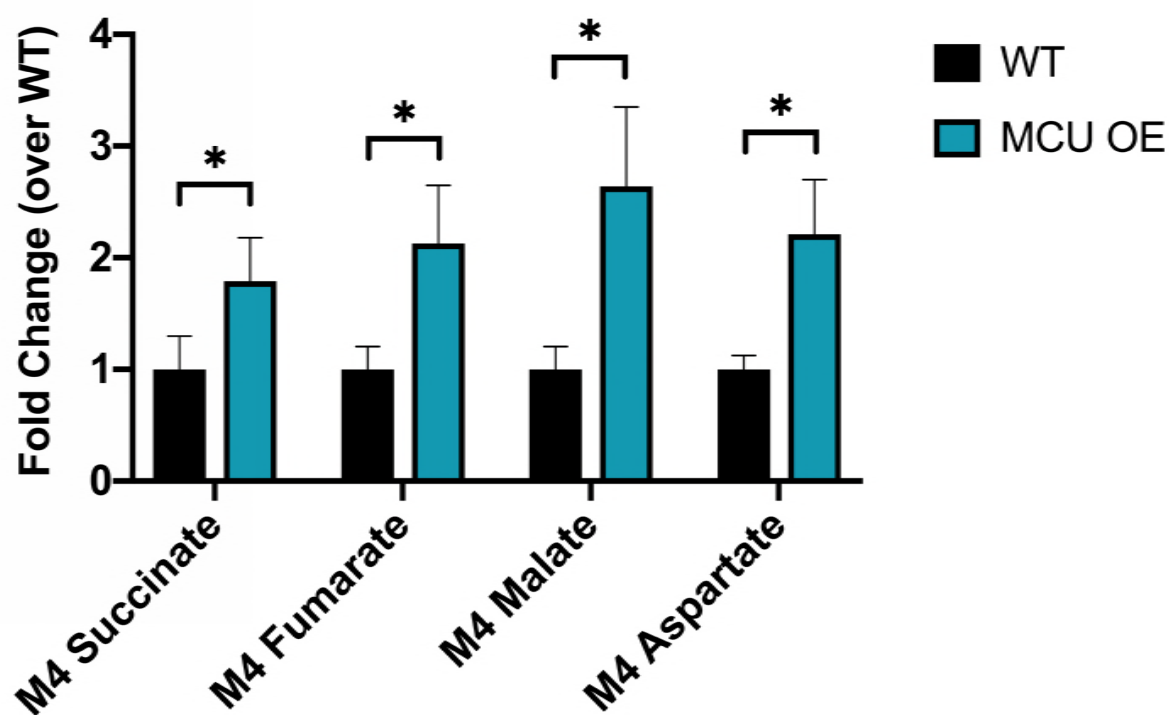


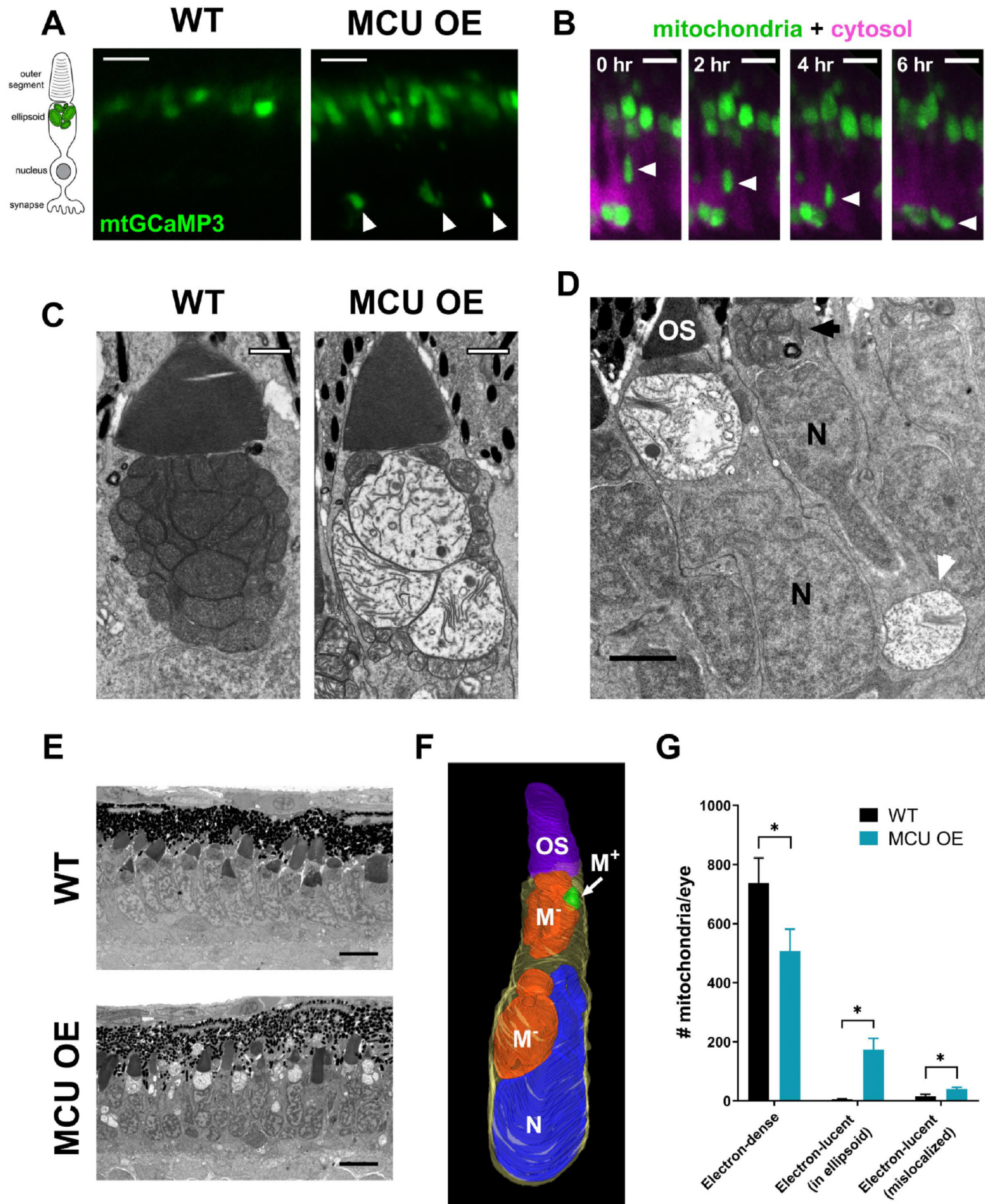
A**B****C**

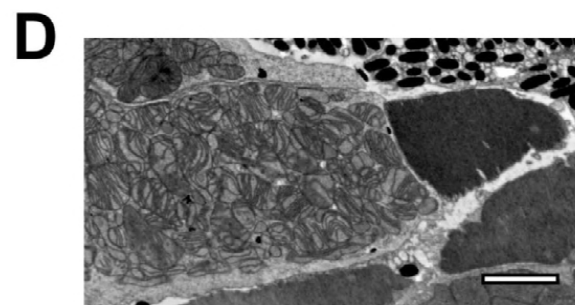
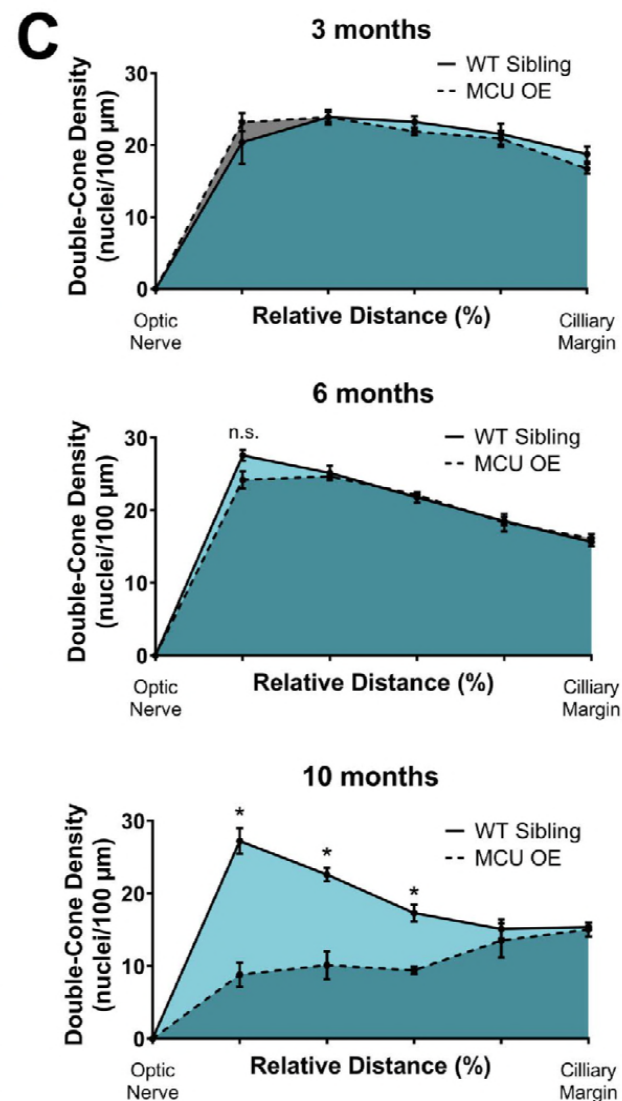
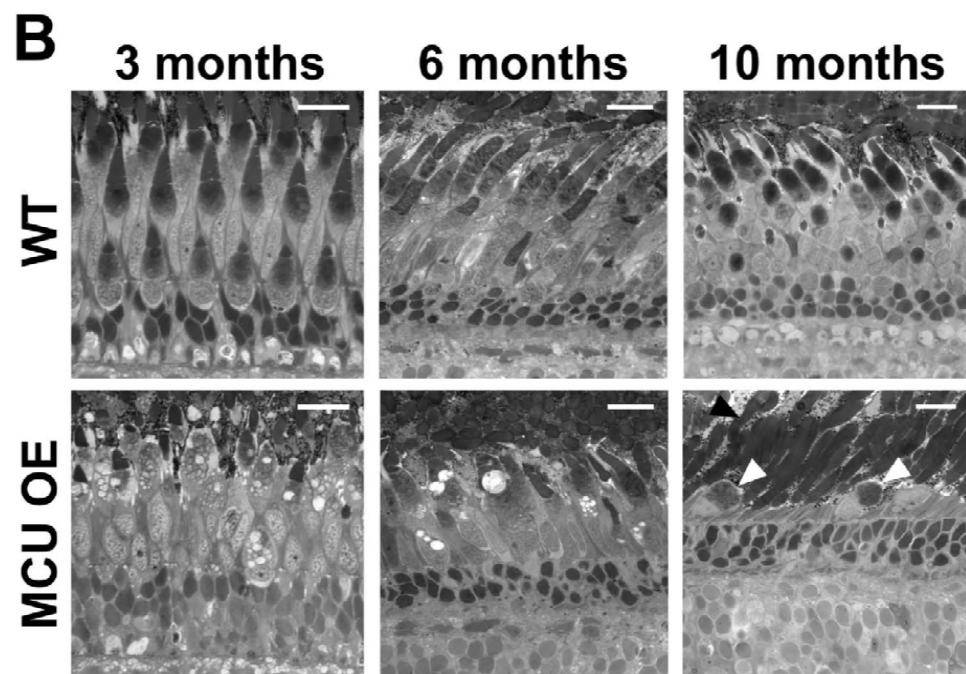
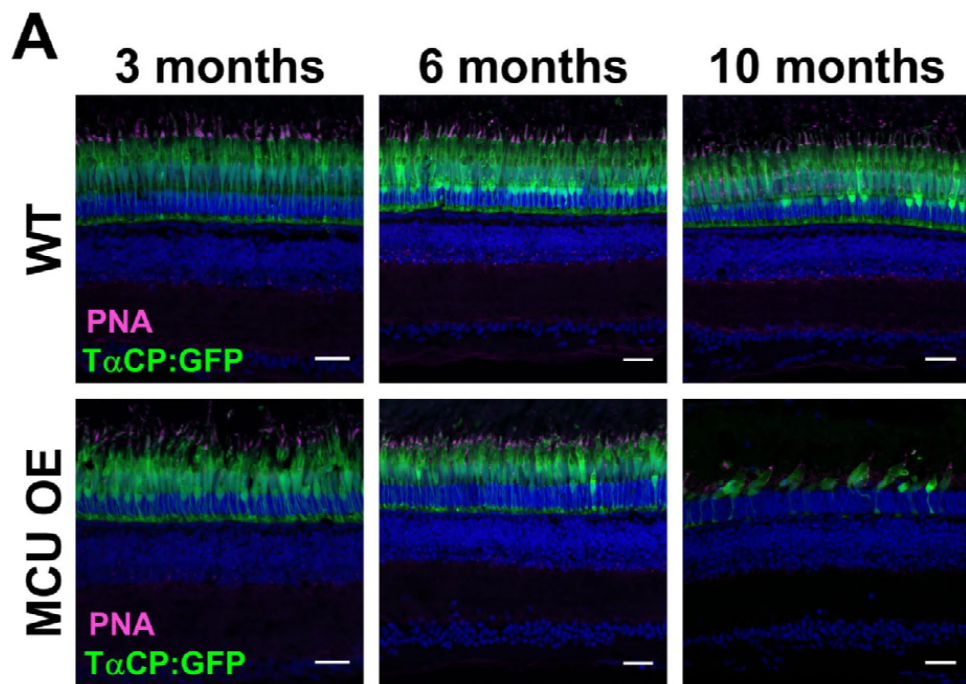
A



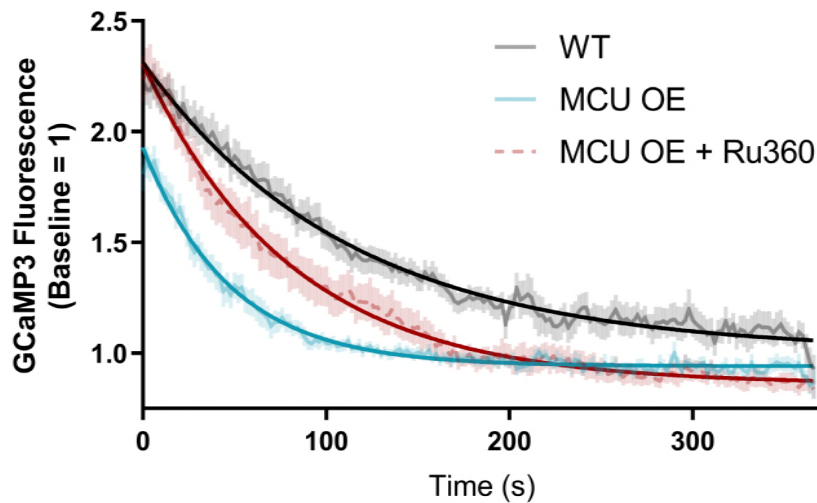
B







A Single Exponential Fits of Ca^{2+} Clearance

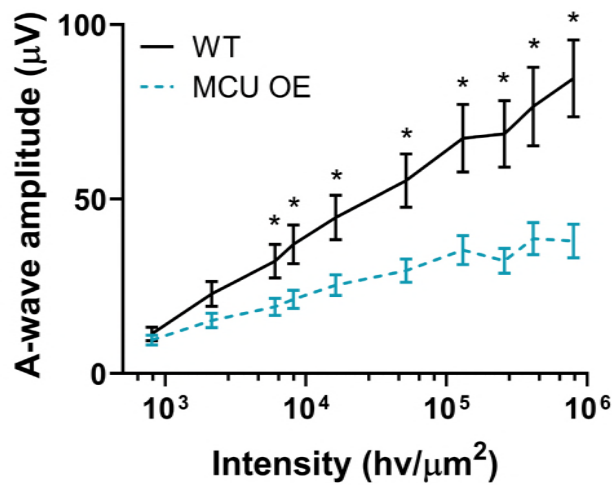


Comparison of Fits

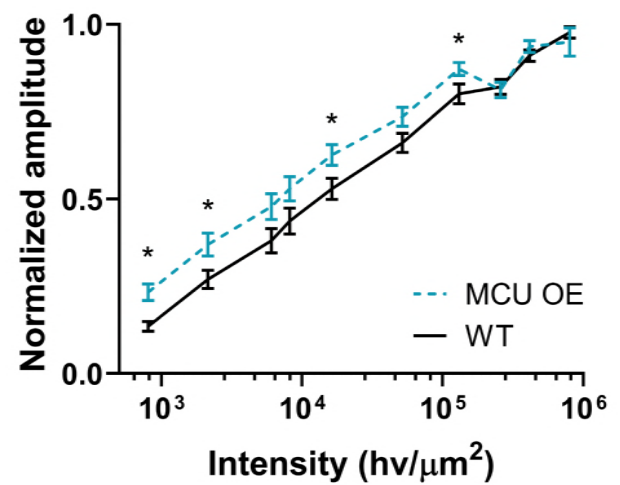
Null hypothesis	K same for all data sets
Alternative hypothesis	K different for each data set
P value	<0.0001
Conclusion (alpha = 0.05)	Reject null hypothesis
Preferred model	K different for each data set
F (DFn, DFd)	99.60 (2, 13176)

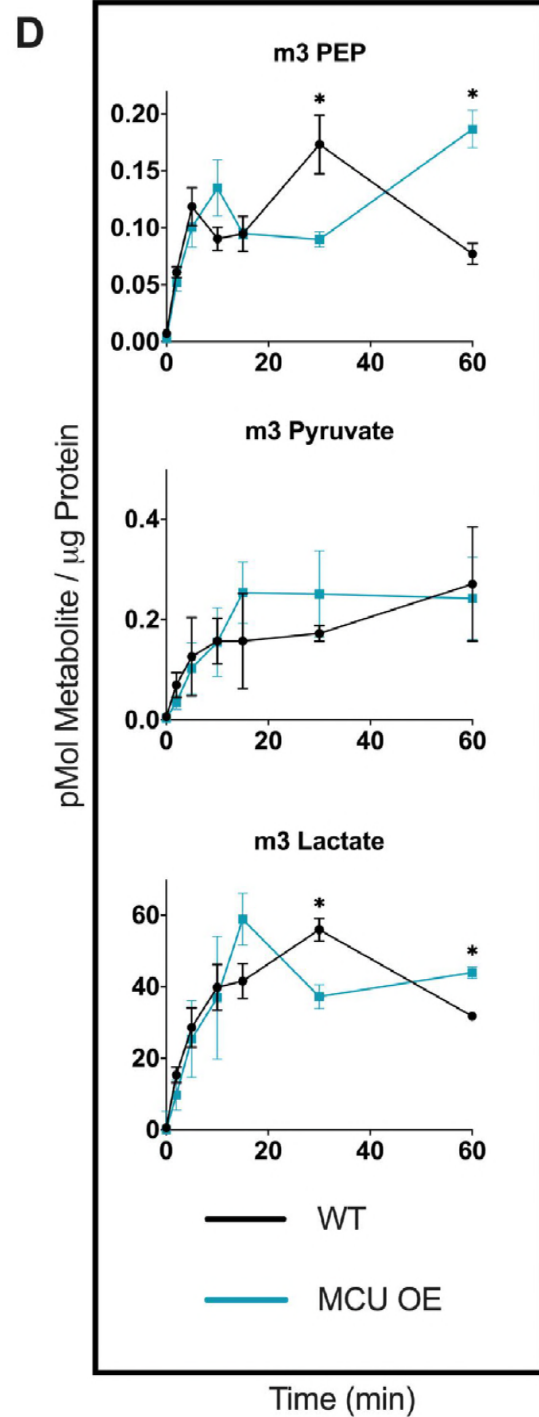
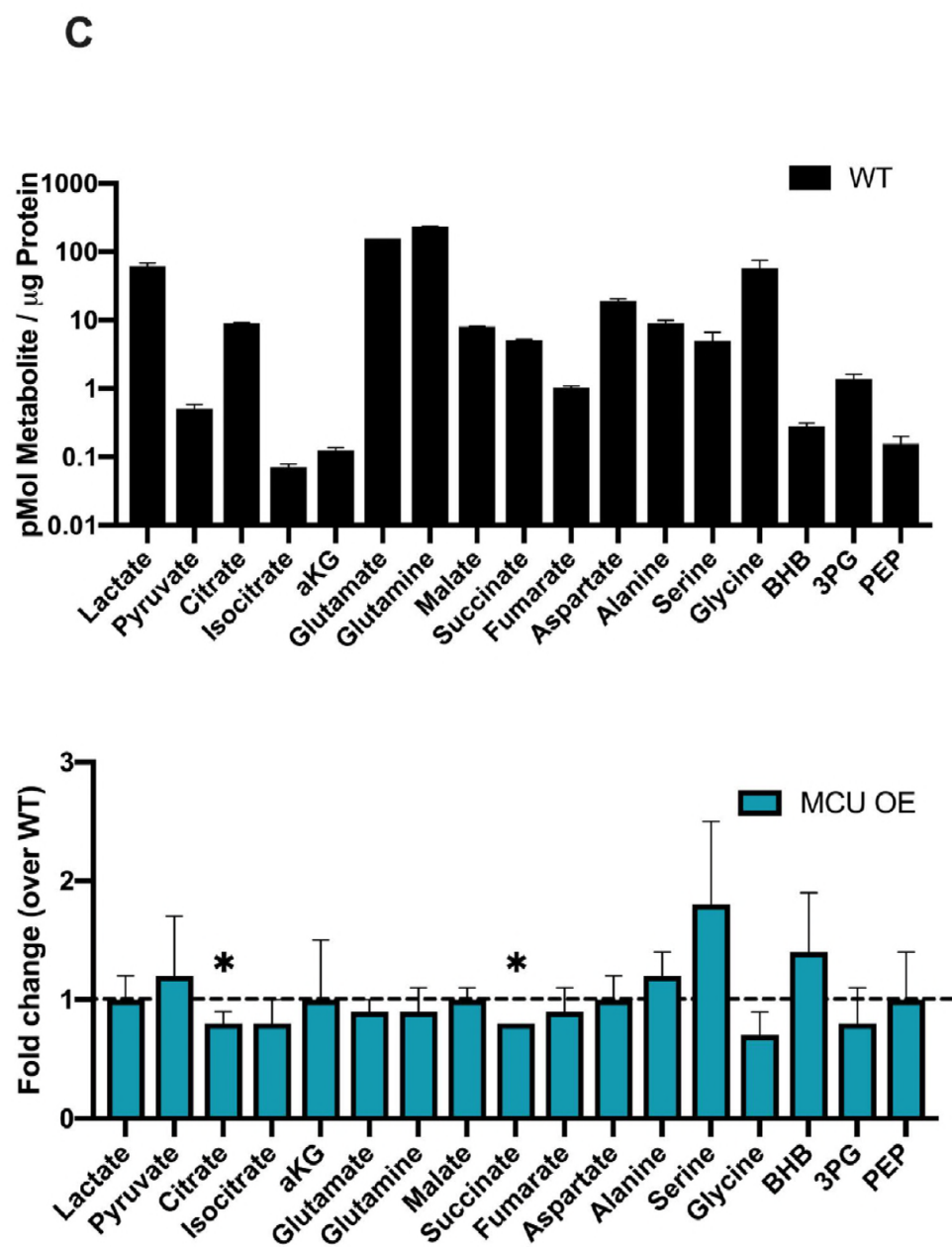
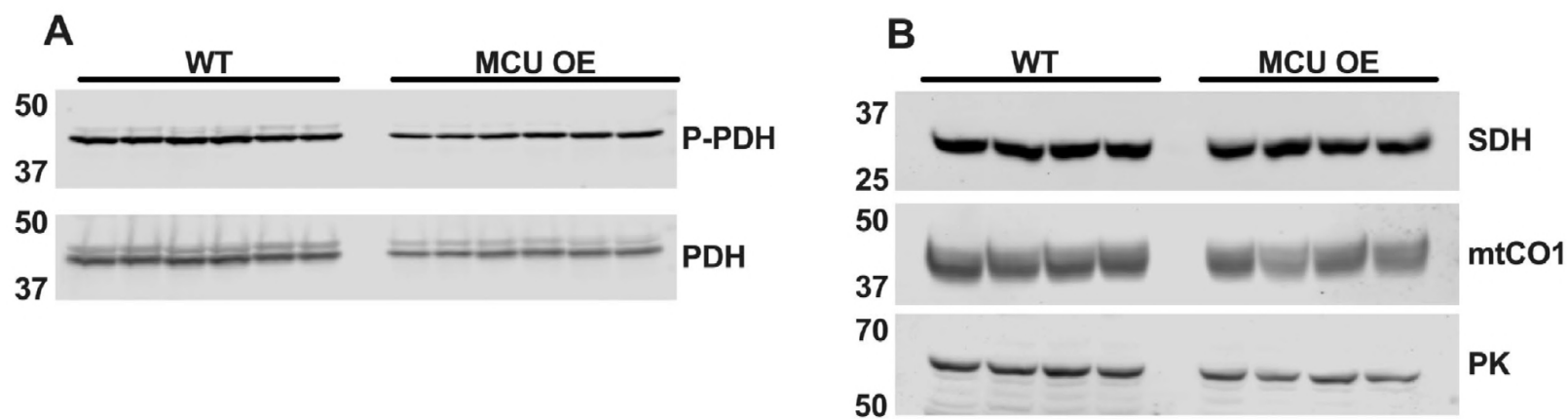
Best-fit Values	WT	MCU OE	MCU OE + Ru360
Y_0	2.314	1.929	2.308
Plateau	1.007	0.9411	0.8592
K	0.008876	0.02114	0.01233
Half Life	78.10	32.79	56.19
Tau	112.7	47.31	81.07
Span	1.306	0.9875	1.449
Std. Error	WT	MCU OE	MCU OE + Ru360
Y_0	0.01950	0.01651	0.02322
Plateau	0.02252	0.005540	0.01133
K	0.0004332	0.0006568	0.0004314
Span	0.02222	0.01592	0.02165

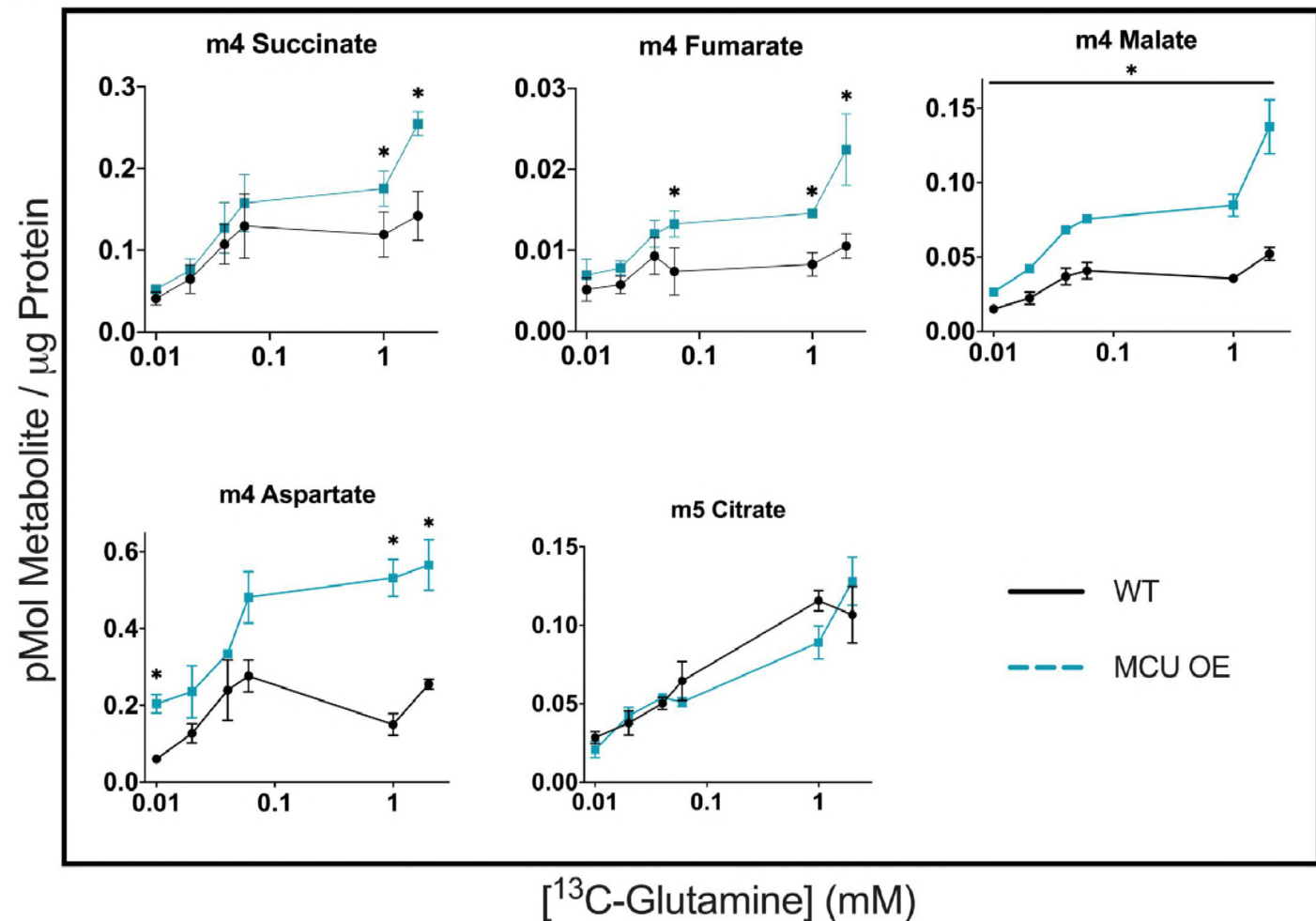
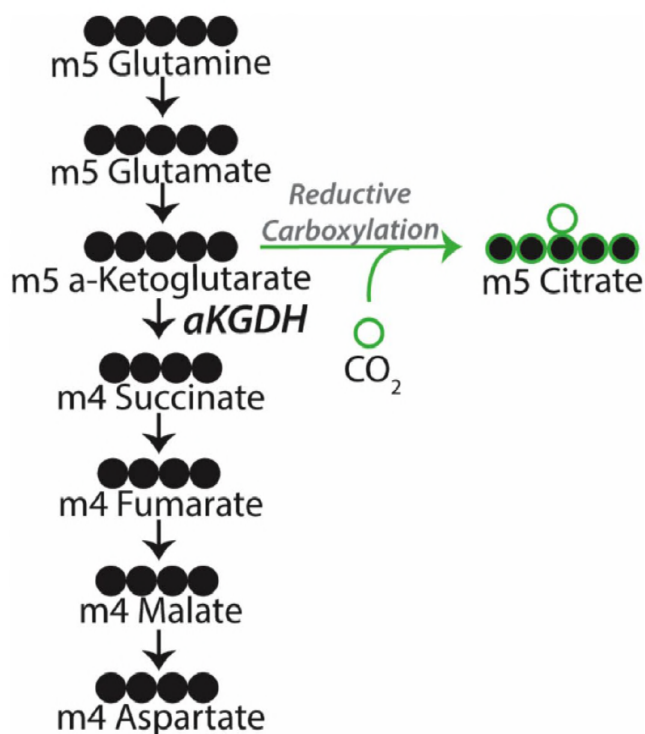
B

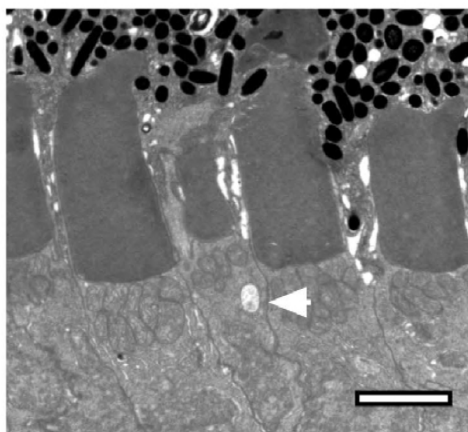
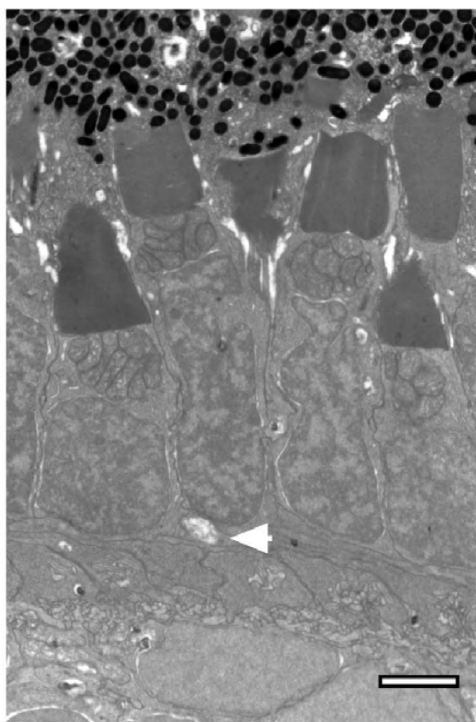
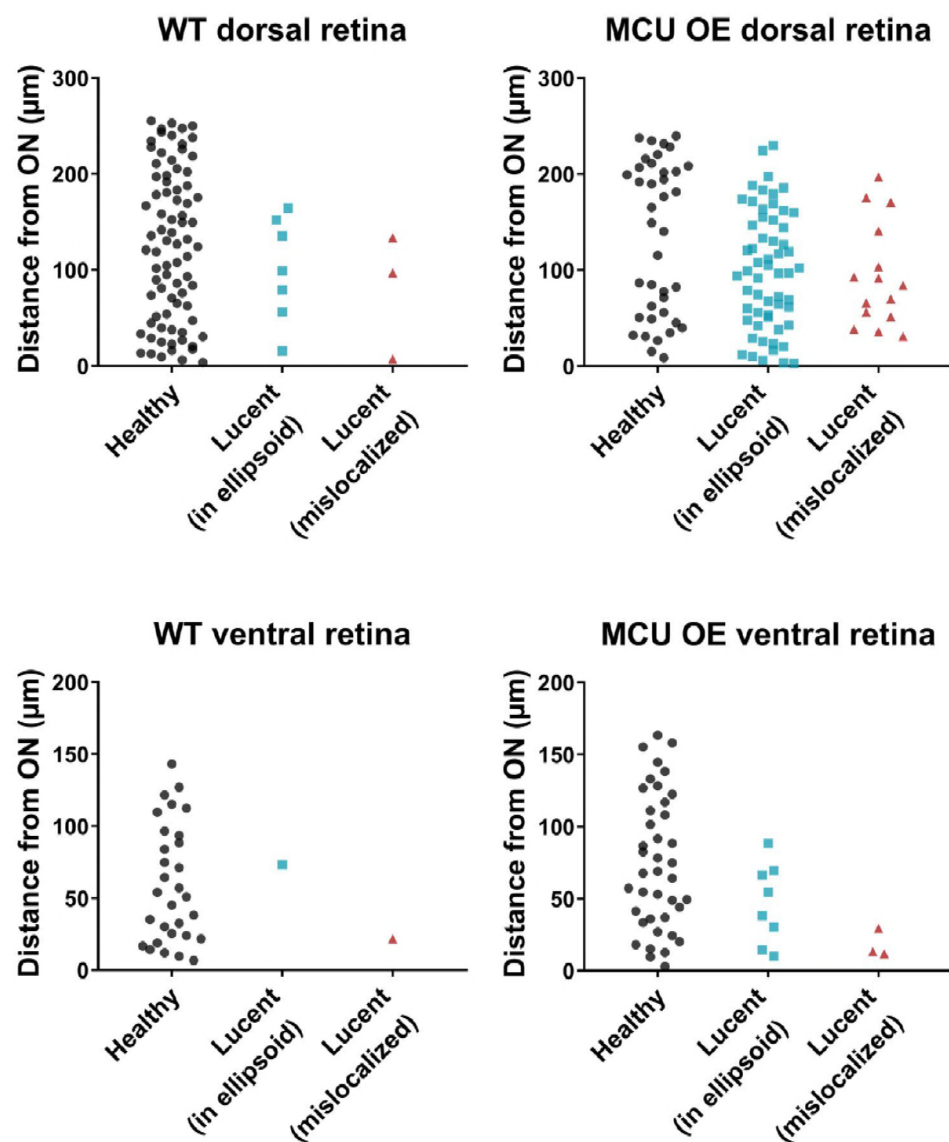
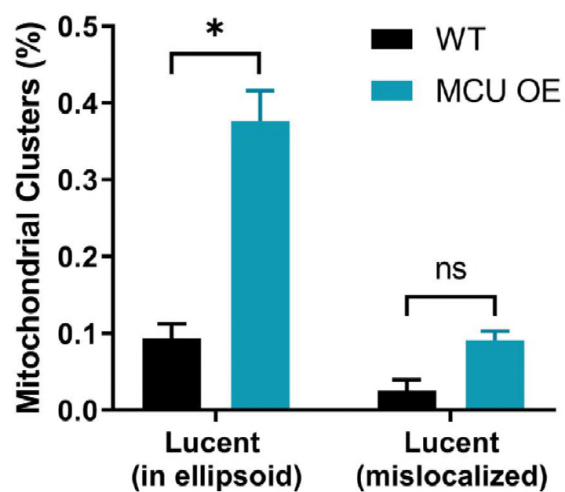


C

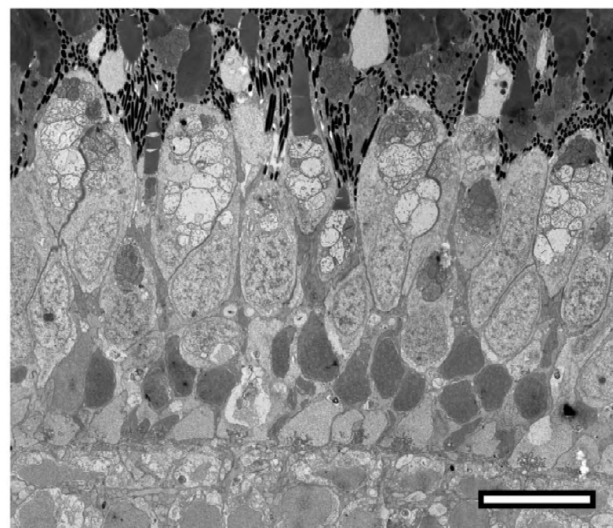




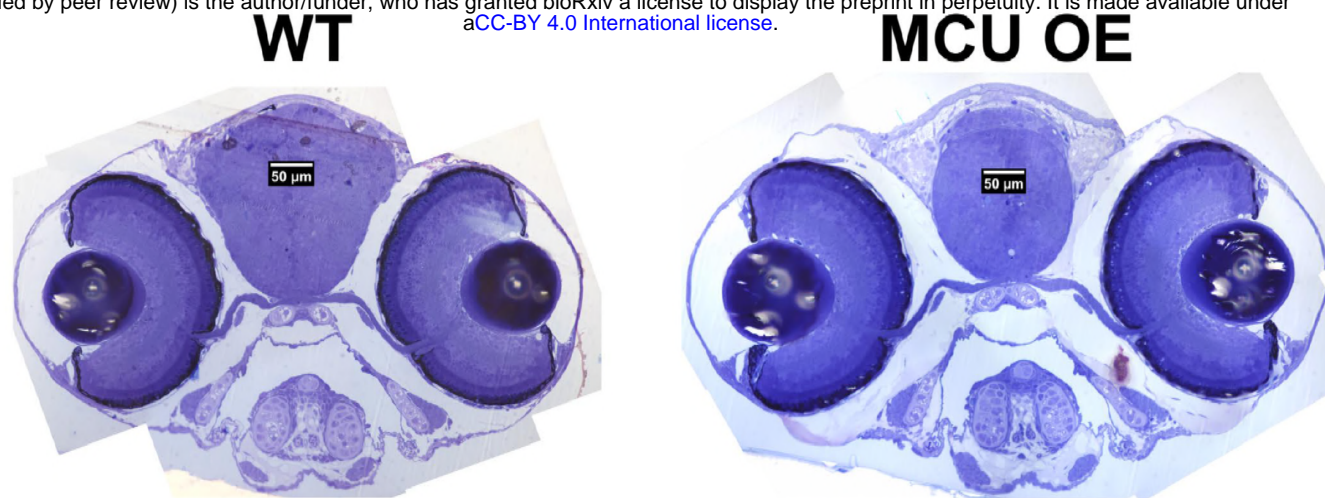
A**B**

A**B****C****D****E**

3 month MCU OE



A

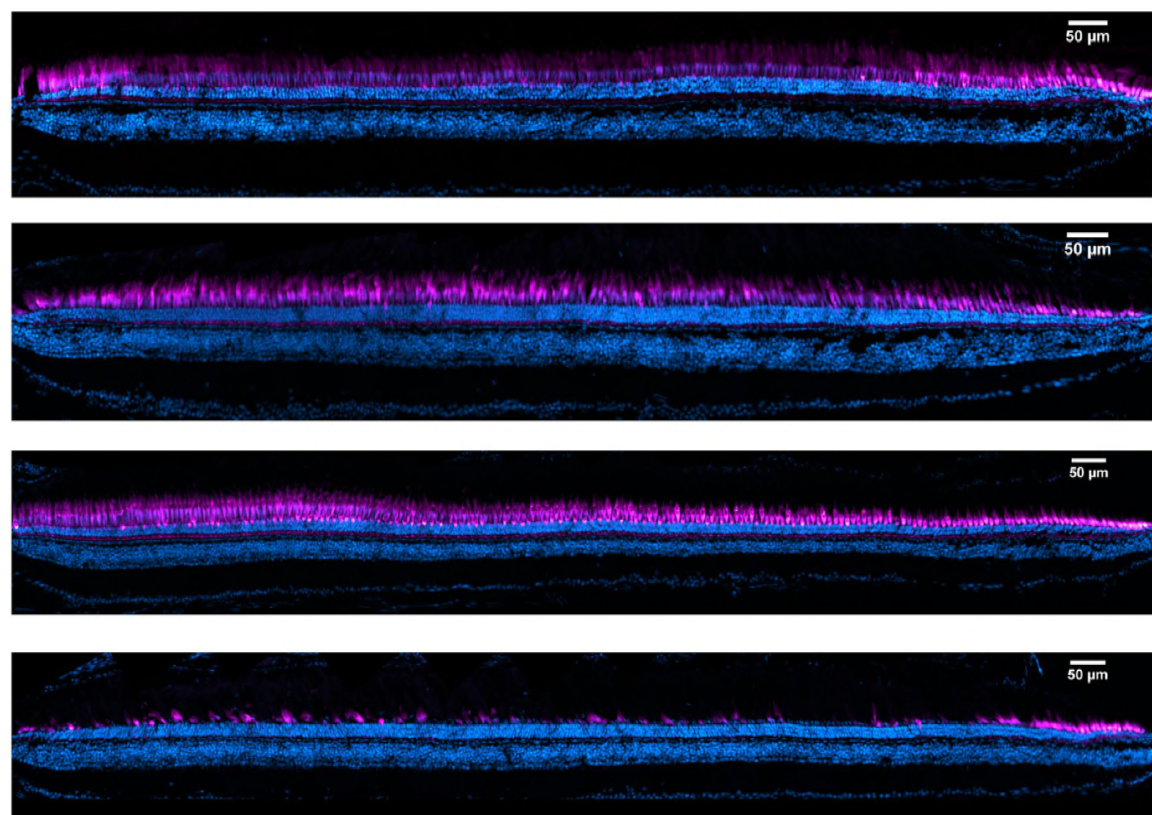


B

optic
nerve

cones (TaCP:GFP) + nuclei (DAPI)

ciliary
margin



WT
6 months

MCU OE
6 months

WT
10 months

MCU OE
10 months

C

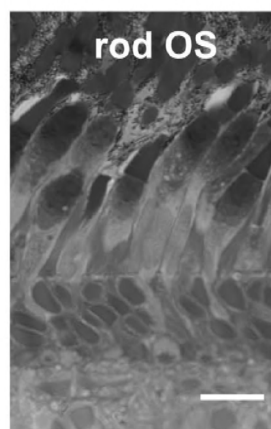
WT

MCU OE

rod OS

rod OS

1 year



D

